ABSTRACT

Title of Document: PROCESSING-STRUCTURE-MICROSTRUCTURE- PROPERTY RELATIONSHIPS IN POLYMER NANOCOMPOSITES

Arun Kumar Kota, Doctor of Philosophy, 2007

Directed By: Professor Hugh A. Bruck,
Department of Mechanical Engineering

The optimal development of polymer nanocomposites using carbon nanotube (CNTs) and carbon nanofiber (CNFs) fillers requires a complete understanding of processing-structure-property relationships. The purpose of this understanding is to determine the optimal approach for processing polymer nanocomposites with engineered microstructures and enhanced material properties. In this research, two processing techniques were investigated: *solvent processing* and *twin screw extrusion*. The former is a batch process which employs mixing a polymer solution with a filler suspension using long mixing times and low levels of shear mixing. The latter is a continuous process that mixes polymer melts with solid nanoscale ingredients using high levels of shear mixing for a short mixing time. Previous studies conducted on polymer-CNT/CNF using these processes have focused mainly on processing-microstructure and structure-property relationships using one technique or the other.

This research focuses on understanding the processing-property relationships by comparing the structure-property relationships resulting from the two processes. Furthermore, the effect of ingredients and processing parameters within each process on microstructure and structure-property relationships was investigated. The microstructural features, namely, distribution of agglomerates, dispersion, alignment, and aspect ratio of the filler were studied using optical, scanning electron, confocal and transmission electron microscopy, respectively. The composition of the filler was determined using thermogravimetric analysis. The electrical, rheological, thermo-oxidative and mechanical properties of the composites were also investigated. Many significant insights related to processing-structure-property relationships were obtained including: (a) deagglomeration is a critical combination of the magnitude of shear rate and the residence time, (b) the structure-property relationships can be modeled using a new methodology based on the degree of percolation by representing the material as an interpenetrating phase composite, (c) annealing can re-establish interconnectivity and improve electrical properties, (d) the degree of dispersion can be resolved using thermogravimetric analysis, and (e) increasing extrusion speed inhibits thermal decomposition and begins to asymptotically increase strength and stiffness through reduction in aspect ratio and size of agglomerates. Finally, a new combinatorial approach was developed for rapidly determining processing-structure relationships of polymer nanocomposites. This dissertation has broad implications in the processing of high performance and multifunctional polymer nanocomposites, combinatorial materials science, and histopathology.

PROCESSING-STRUCTURE-MICROSTRUCTURE- PROPERTY RELATIONSHIPS IN POLYMER NANOCOMPOSITES

By

Arun Kumar Kota

Dissertation submitted to the Faculty of the Graduate School of the
University of Maryland, College Park, in partial fulfillment
of the requirements for the degree of
Doctor of Philosophy
2007

Advisory Committee:
Dr. H. A. Bruck, Associate Professor of Mechanical Engineering, Chair
Dr. D. I. Bigio, Associate Professor of Mechanical Engineering
Dr. S. R. Raghavan, Associate Professor of Chemical and Biomolecular Engineering
Dr. A. Dasgupta, Professor of Mechanical Engineering
Dr. S. D. Solares, Assistant Professor of Mechanical Engineering

Dedication

To the all pervasive Divinity that guided my

search for Truth in Science

Acknowledgements

I would like to express my deepest appreciation and gratitude to Dr. Bruck without whose guidance, support and encouragement this thesis would not have been possible. I admire Dr. Bruck's constructive criticism of technical writing and his helpful remarks. I thank him for imparting me advice both on personal and professional fronts. I am indebted to him for guiding me in preparing for a career in academia.

My sincere thanks and regards to all the professors at University of Maryland who have provided valuable suggestions and resources for my research. Special thanks to Dr. Bigio for helping me understand the mixing concepts associated with twin screw extrusion and to Dr. Raghavan for providing me with rheological concepts and a lot of guidance on the personal front.

My warm regards to the program manager turned mentor turned friend, Dan Powell, for his help on both personal and professional fronts.

I extend a warm thanks to my colleagues, Dan, Alan, Arvind and Bani, who have helped with their valuable suggestions and kept me company all along. I also extend a warm thanks to all the NASA interns, undergraduate students and friends for contributing innumerable hours of work towards the research. A special thanks to my house mates Isaac and Vikram for being very accommodating.

I sincerely appreciate the help provided by all the staff at University of Maryland, especially by Howie in the machine shop and Penny in the main office.

I love my parents and sister beyond expression for their support and encouragement at all times.

Table of Contents

List of Tables

List of Figures

1. Introduction

With the availability of new and improved processing and characterization techniques, researchers have become increasingly interested over the past decade in altering homogeneous materials by adding nanoscale fillers to create what are now being called *nanocomposites*. The unique high surface-to-volume ratios of the nanoscale fillers, combined with quantum mechanical and other nanoscale physical effects, have rendered the nanocomposites with properties that are significantly different from composites that are microstructured, and have unique structural characteristics that can also be possibly controlled by a given process in a different manner. Their significantly different properties have allowed and retain the potential for the development of novel materials, processes, phenomena by engineering composites at the nanoscale [1]. This may lead to new avenues in science and technology that require understanding in more detail the relationship between the processing of these nanocomposites, and their resulting structure and associated properties.

1.1 Background

1.1.1 Carbon Nanotubes and Carbon Nanofibers

Two specific nanoscale fillers, Carbon Nanotubes (CNTs) and Carbon Nanofibers (CNFs), have been identified by materials scientists as having the greatest potential to revolutionize the technological landscape of the century ahead. CNTs can be categorized further as single-walled carbon nanotubes (SWCNTs) and multi-walled carbon nanotubes (MWCNTs). SWCNTs are graphene sheets (hexagonal arrangement of sp^2 hybridized

carbon atoms) rolled into a cylinder and the ends closed by a hemi-fullerene with an appropriate diameter to form a nanotube as shown in figure 1.1 [2].

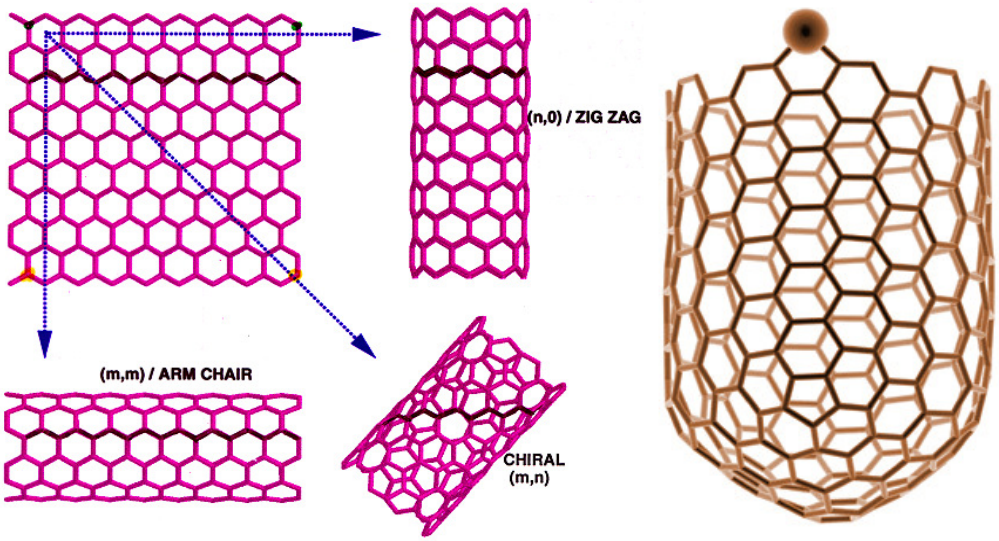

Figure 1.1 Structure of SWCNTs [2]

The nanoscale characteristics of these fillers are defined by their diameters, which range from less than a nanometer to few nanometers. MWCNTs are formed from concentric SWCNTs with diameter increase in range from a few nanometers to a few tens of nanometers as shown in figure 1.2 [2].

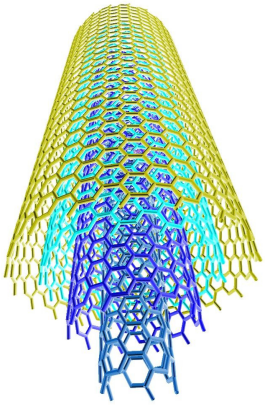

Figure 1.2 Structure of MWCNTs [2]

CNFs are similar in structure to MWCNTs, but have much larger diameters – on the order of hundreds of nanometers – and are formed from graphene layers arranged as stacked cones, cups or plates instead of perfect cylinders. CNTs and CNFs are unique due to their electronic structure and versatile properties like high adsorption, high mechanical strength, high electrical and thermal conductivity and low reactivity. These characteristics of CNTs and CNFs can further be translated to secondary structures with applications [1] in near-field microscope probes, field-emission based devices, chemical sensors, catalyst supports, gas storage, super-capacitors, nano-electronics and multifunctional or high-performance composite materials.

1.1.2 Polymer-CNT/CNF Composites and their Applications

Polymer nanocomposites based on CNTs and CNFs are gaining importance in the global market due to their diverse applications. For example, compelling needs such as reduction of system mass, system-failure risks, and system complexity, while simultaneously imparting spacecraft and mission reconfigurability are demanding the development of high-performance and multifunctional polymer nanocomposites. Ever since the first polymer-CNT composites have been reported by Ajayan et al [3] in 1994, their fabrication has been increasingly reported with enhancements in mechanical, electrical, thermal and rheological properties. Isotropically-enhanced nanostructured bulk composites and directionally-enhanced composite films have the potential for utilization as space mission-enabling materials and in the civilian space arena. In specific, they can be used as light-weight aerospace structural panels, thin-walled space structures, EMI shielding and radiation shielding materials. Furthermore, they can also be used in

sporting goods, automotive parts, electrostatic paints and heat sinks for electrical and electronic components [2].

While CNTs have been the primary focus of laboratory-scale research into the potential for property improvement in polymer composites, the considerably less expensive CNFs ($50/g for CNTs, $500/Kg for CNFs) have been more desirable for commercial production of polymer composites. However, the properties that have been characterized for polymer-CNF composites have not been as good as the polymer-CNT composites (e.g., approximately an order of magnitude difference in filler loadings for electrical percolation threshold and tensile modulus). As a consequence, there has been an additional need to compare the processing-structure-property relationships between polymer nanocomposites containing CNTs and CNFs for different processes in order to realize the potential seen in laboratory-scale research.

1.2 Motivation for Research

In order to enhance the desired material properties for truly and comprehensively realizing the application potential, it is important to understand how the processing and formulation (i.e., choice of composition and ingredients) of the polymer-CNT/CNF composites affects the structure and associated properties of these nanocomposites. Since CNTs are very expensive, we will use them only for small quantities of material produced via solvent processing, while larger quantities of considerably less expensive CNFs will be studied in both solvent and twin screw extrusion (TSE) processing. It is essential to understand the effect of various processing parameters on the structure of the polymer nanocomposites that in turn govern their properties. Establishing such

processing-structure-property relationships also provides avenues to engineer the properties of the material to suit the demands of the application.

With the above factors in view, the focus of this research is to fabricate polymer-CNT/CNF material system using two different processes, an established laboratory-scale *solvent processing* technique and a more scalable, commercial *twin screw extrusion* (TSE) technique, and to characterize the processing-structure-property relationships (see figure 1.3).

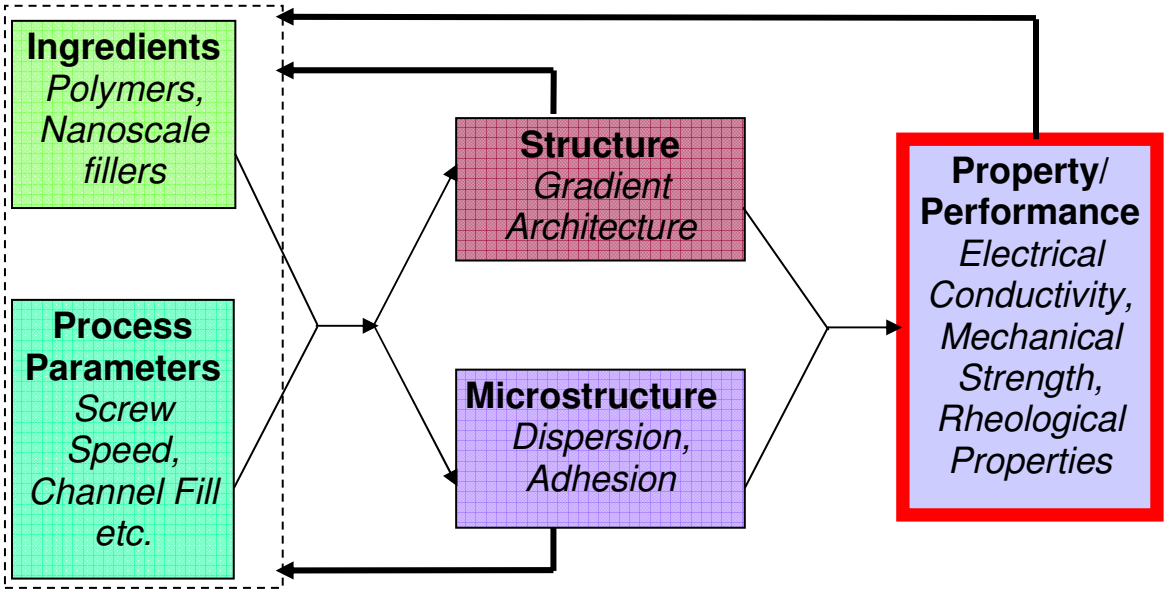

Figure 1.3 The inter-relationship of processing-structure/microstructure-property

Since a majority of the processing-related research that has been conducted on polymer nanocomposites has focused on just small quantities of material produced via solvent processing to determine structure-property relationships, it will be important to see how the differences in the batch nature of the solvent processing and the continuous nature of the TSE technique affect the structure-property aspect of the relationships. It is also possible to use the continuous nature of the TSE technique to produce nanocomposites that are compositionally graded for rapid characterization of structure-

property relationships in a combinatorial material science approach. Using the structure and property characterization, it will be possible to develop models to explain the fundamental physics governing of the structure-property relationships.

1.3 Research Objectives

The following list provides a detailed set of objectives for this research with polystyrene (PS) as the model polymer matrix:

- Establish procedures to fabricate PS-MWCNT/CNF composites using the solvent processing (batch process) and twin screw extrusion (continuous process) techniques for further comparison by characterization.
- Study the processing-microstructure relationships for the solvent processed PS-MWCNT composites, solvent processed PS-CNF composites, and extruded PS-CNF composites and compare when applicable.
- Establish the following structure-property and processing-property relationships for the PS-MWCNT/CNF composites produced by extrusion, compare them with the solvent processed, and explain them with the processing-microstructure relationships:
    i. Characterize electrical percolation and model electrical conductivity as a function of composition.
    ii. Characterize rheological percolation and relate it to electrical percolation by modeling the storage and loss moduli of interpenetrating phase composites using degree of percolation.
    iii. Characterize the thermo-oxidative behavior as a function of composition and the processing technique.

iv. Characterize the mechanical properties as a function of composition and extrusion processing parameters.

v. Establish the relation between the evolution of electrical, rheological, thermo-oxidative and mechanical properties of the composites and their microstructure.

- Develop a convolution process model based on previously developed mixing models and an in-situ measurement technique in order to predict the compositional gradient produced by transient addition of nanoscale fillers into a twin screw extruder, and compare the compositional gradients with a posteriori characterization. Thus, develop a new approach to establishing processing-structure-property relationships in polymer nanocomposites via combinatorial materials science.

1.4 Dissertation Outline

In the following chapters of this dissertation, the methods used to address the above objectives and the results obtained will be presented. Chapter 2 contains a review of the processes used for producing polymer nanocomposites. While providing a detailed review of the research conducted to establish and understand the processing-microstructure and structure-property relationships, it also delineates the deficiencies in the processing-property and processing-structure relationships in various polymer nanocomposites systems. Chapter 3 describes the ingredients used in this work, their properties, and experimental methods used to process and characterize the structure, microstructure and properties of the polymer nanocomposites. Chapter 4 presents and discusses in detail the results obtained by characterizing, the structure, microstructure and

material properties of the PS-MWCNT and PS-CNF composites in context of the various relationships presented in chapter 2. Finally, chapter 5 summarizes the scientific and technical contributions of this work and presents the research issues that have potential for future investigation.

2. Literature Review

2.1 Polymer Nanocomposites : Processing

Several processing methods are available for producing polymer nanocomposites, with both thermoplastic or thermoset polymer matrices and nanoscale fillers. Although the techniques are inherently different, all of them try to address issues such as deagglomeration of filler bundles and ropes, dispersion and alignment of the individual filler particles, and interfacial adhesion between the polymer matrix and the filler that directly affect the composite properties [4,5]. Similar to other nanoscale fillers, the effective utilization of CNTs and CNFs in composite applications depends strongly on the ability to disperse the CNTs individually and uniformly throughout the matrix without destroying their integrity or reducing their aspect ratio [6]. Furthermore, good interfacial bonding is required to achieve load transfer across the polymer-CNT/CNF interface [7]. Finally, the 3D architecture will determine the properties – for example, skeleton-like for percolation, or well-aligned for high strength [8]. The three most common techniques – solvent processing, melt mixing, and in situ polymerization are discussed in detail. However, new techniques, pre and post-processing techniques and combination of techniques have also been utilized.

2.1.1 Solvent processing

Solvent processing (also called solution blending) provides an advantage through low viscosities, which facilitate mixing and dispersion of the CNTs/CNFs. Solvent processing involves three major steps: (1) dispersing the CNTs/CNFs in a suitable

solvent, (2) mixing with the polymer (at room temperature or elevated temperature), and (3) recovering the composite. There have been several variations of these three major steps to obtain the composite in the desired manner. For example, Du et al. [10] developed a versatile coagulation method that involves sonication of SWCNTs followed by mixing and stirring with poly-(methyl methacrylate) (PMMA) solution, and pouring the PMMA-SWCNT suspension into an excess of non-solvent to recover the composite. The precipitating polymer chains entrap the SWCNTs, thereby preventing the SWCNTs from bundling. A variant of recovering the composite is precipitation by cooling. This method has also been adapted to polyethylene (PE), where the PE-SWCNT suspension is heated to promote polymer solubility and then cooled to accomplish the precipitation [10]. When using solvent processing, CNTs/CNFs tend to agglomerate during slow solvent evaporation, leading to inhomogeneous distribution of the CNTs in the polymer matrix. The evaporation time was reduced by placing the polymer-CNT suspension on a rotating substrate (spin-casting) [11] or dropping the polymer-CNT suspension on a hot substrate (drop-casting) [12]. Many studies have used solvent processing with both thermoset and thermoplastic polymers. Biercuk et al. [13] dissolved epoxy in a well-dispersed, ultrasonicated SWCNT suspension. The solvent was evaporated, and the epoxy was subsequently cured to form a nanocomposite. Safadi et al. [14] and Watts et al. [15] added MWCNTs to a solution of PS dissolved in toluene, and made composites both by film-casting and spin-casting. Aqueous solutions may also be used, depending on the polymer. An aqueous poly(vinyl alcohol) (PVA) solution was mixed with an electrostatically stabilized dispersion of CNTs in water, and was subsequently casted to form a composite film [16]. Qian et al. [17] made use of a simple solvent evaporation

method assisted by high energy sonication to prepare polystyrene PS-MWCNT composite films. Solvent processing of polymer-CNF composites is not uncommon. For example, Yang et al [18] and zhang et al [19] prepared PS-CNF composites using toluene by sonication and magnetic stirring. In summary, solvent processing is a simple, yet versatile lab scale, batch process for preparing the polymer-CNT/CNF composites.

2.1.2 Melt mixing

Melt mixing of CNTs/CNFs with thermoplastic polymers using conventional processing techniques, such as extrusion, internal mixing, injection molding and blow molding, is particularly desirable, because of the speed and availability of these processes in the plastics industry. Nevertheless, there is still much to be learnt about the ability of CNTs/CNFs to withstand high magnitude of shear rates in the elongational flows and simultaneously about the optimal processing parameters that can provide isotropic dispersion of CNTs/CNFs. The widely used extrusion compounding is still the most convenient melt mixing technique and practical way to prepare filled polymer composites when nanoscale fillers are considered to replace microscale fillers for high-performance materials. However, mixing the nanoscale fillers with the polymer melt is more difficult than that of microscale fillers due to their strong tendency to agglomerate.

Ferguson et al. [9] used a Buss Kneader for initial compounding, followed by injection molding to prepare composites of CNTs with various thermoplastics. Sandler et al. [4] dispersed MWCNTs in an epoxy by high speed stirring (2000 rpm) using a dissolver disk for 1 hour. They also investigated the effect of increased shear force by decreased the temperature of processing, thereby increasing the resin viscosity. Sennet et

al. [20] and Potschke et al. [21] in two different work compounded polycarbonate (PC) with MWCNTs in a DACA co-rotating, intermeshing, conical twin screw microcompounder at 50-80 rpm with 250-265^{o}C to investigate the affect of draw rate on the microstructure and properties of the composites. Mahfuz et al. [22] dry mixed Nylon6 and MWCNTs and extruded in a single screw extruder and heat stabilized to form continuously drawn composite filaments. Kashiwagi et al. [23] prepared of MWCNTs with polypropylene (PP) composites in a Haake Polylab shear mixer at a temperature of 190^{o}C and screw speed of 20 rpm by mixing for 30 min to investigate the thermal stability and flame retardancy. Melt mixing of polymer-CNF composites to study the properties and microstructure was also extensively reported in literature. For example, small quantities of premixed PP and CNFs were fed to Haake Rheocord 90 twin screw extruder and extruded at a screw speed of 20 rpm followed by pelletization and fiber spinning [24] to study the morphology and mechanical properties of the composites. Andrews et al. [6] conducted an extensive study to investigate the microstructure, electrical, rheological and mechanical properties of composites of PS, PP, acrylonitrile-butadiene-styrene (ABS) with MWCNTs and CNFs by processing them using a Haake Polylab shear mixer. In summary, unlike solvent processing, melt mixing is beneficial because it is free of solvents, which could possibly act as contaminants at the polymer-filler interfaces.

2.1.3 In situ polymerization

In situ polymerization aims at bottom up synthesis of the entire composite structure by mixing the monomer and the nanoscale filler followed by polymerization. It

is a method used for improving dispersion by better integration between the phases [18]. The main advantage is that reinforcement is obtained on a molecular scale. Tang and Xu [25] synthesized poly(phenylacetylene)-wrapped carbon nanotubes (PPA-CNTs), which were soluble in organic solvents, such as tetrahydrofuran, toluene, chloroform and 1,4-dioxane. Fan et al. [26] synthesized conducting polypyrrole-coated carbon nanotubes (PPY-CNTs), and found that the magnetization of the composites is the sum of the two components, PPY and CNTs. Usually, most in situ polymerization works to prepare polymer composites are conducted in conjunction with pre and post-processing techniques.

2.1.4 Other methods

A combination of the above methods have also been used, along with pre and post-processing techniques, like purification, chemical treatment using surfactants, compatibilizers etc. Xie et al. [27] prepared PP-CNT composites compatibilized with maleic anhydride grafted styrene–(ethylene-co-butylene)–styrene copolymer by using a combination of ball milling and melt mixing. Jin et al. [28] coated MWCNTs by poly(vinylidene fluoride) (PVDF) and then melt-blended with PMMA. PVDF was found to be a compatibilizer that assists dispersion of MWCNTs in PMMA and served as an adhesive to increase their interfacial bond strength, hence greatly improving the mechanical properties of PMMA-MWCNT composites. Additionally, surfactants can be used as dispersing agents to improve the dispersion of CNTs in processing polymer-CNT composites. Gong et al. [29] used a non-ionic surfactant, polyoxyethylene-8-lauryl, as a processing aid for epoxy-CNT composites due to the strong interactions between carbon

of CNTs and the hydrophobic segment of the surfactant via van der Waals forces, as well as epoxy and the hydrophilic segment of the surfactant via hydrogen bonding. The homogeneous dispersion of CNTs in epoxy improved the thermomechanical properties of the composites. Haggenmueller et al. [30] used a combination of solvent casting and melt mixing to disperse up to 8 wt.% SWCNTs in PMMA. Solvent cast composite film was broken into pieces and hot pressed into new films, which were again broken into smaller fragments and pressed again. This procedure was repeated as many as 25 times. The dispersion was found to improve as the number of steps was increased, with some of the films showing increased electrical conductivity. In summary, although the property enhancement observed with the combination of various methods, or with pre and post-processing techniques is higher, the difficulty and time involved in processing makes them unsuitable for large-scale, continuous production.

2.2 Processing – Microstructure Relationships

The influence of processing on the evolution of various aspects of microstructure, such as distribution, dispersion, alignment, agglomeration etc., was studied in great detail over the past decade with the availability of new and improved nanoscale characterization techniques.

Du et al. [10] characterized the PMMA-SWCNT composites using optical microscopy and Raman imaging. They concluded that a macroscopic good dispersion is obtained when wet SWCNTs are used and macroscopic phase separation can be seen when dry SWCNTs are used. Furthermore, using scanning electron microscopy (SEM), at a 2 wt.% loading of SWCNTs in PMMA, they reported a filler network that impeded the

motion of SWCNTs past one another. Sandler et al. [31] prepared well dispersed CNFs (see figure 2.1) in a thermoplastic poly(ether ether ketone) (PEEK) matrix via TSE at a loading of 15 wt.%.

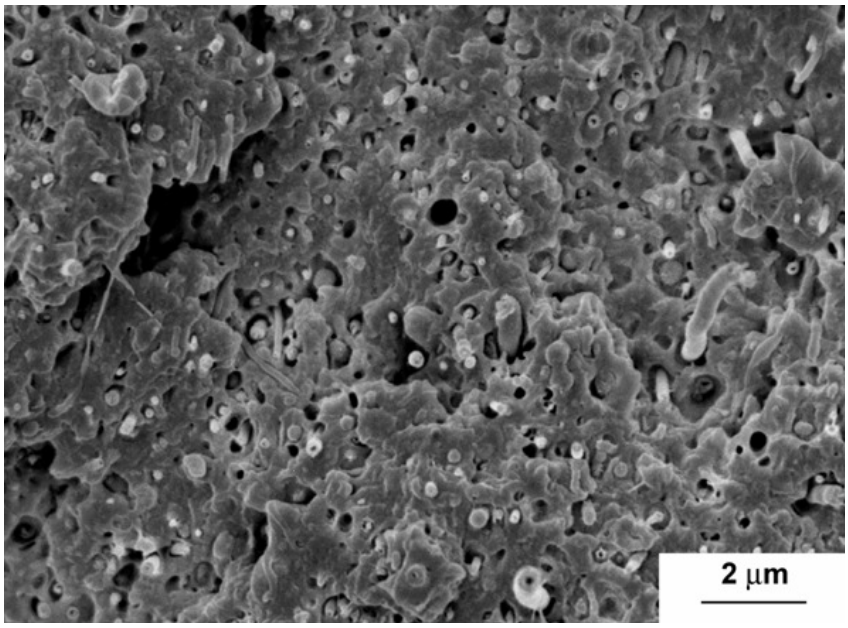

Figure 2.1 An SEM image showing an isotropic dispersion of CNFs in PEEK matrix at 15 wt.% loading [31].

They reported that high intrinsic viscosity of thermoplastic matrices in general, has the dual advantage of increasing the shear applied to the aggregates (even breaking the individual CNTs/CNFs) and minimizing the opportunity for reaggregation. However, even extensive TSE does not lead to a complete break-up of the entanglements in commercially available catalytically-grown MWCNTs [32-34]; nanotube clusters were observed even at low filler loadings. Prolonged mixing times lead to an improved distribution of nanotube aggregates [33]. In contrast, nanotube weight fractions of up to 30 wt.% of arc-grown as well as of CVD-grown MWCNTs were shown to disperse in PMMA [35] and PS [36] matrices, and the use of aligned, rather than entangled nanotubes, also appears to be advantageous [37]. Although filler dispersion can be aided

by ball milling of the raw filler material prior to processing [38], this approach degrades the aspect ratio of individual particles significantly more than shear-intensive melt processing [39].

Processing of compounds under conditions involving both shear and elongational flows, such as injection-molding, can be used to induce alignment of the nanofiller [40]. Similarly, Kuriger et al. showed that flow-induced nanofiber alignment occurred during extrusion [39]; the degree of nanofiber alignment was improved by optimization of the extruder die geometry. Keeping the extruded strand under tension minimized die swell effects and the orientation of the filler was maintained. However, a decreasing degree of alignment with increasing nanofiber content was observed, most likely as a result of nanofiber-nanofiber interactions altering the flow field [39]. Similarly, drawing of composite extrudate was shown to induce significant nanotube alignment [36,20,41] (see figure 2.2) as did mechanical stretching of solid nanocomposites above the glass transition temperature [42,43], spin-casting of nanotube-polymer solutions [14], and the application of magnetic fields during in-situ polymerization [44].

In summary, although processing-microstructure relationships have been extensively studied in polymer nanocomposites, and there will continue to be a need for constantly studying them since they form the fundamental link between optimizing the processing parameters and realizing enhanced material properties through engineered microstructures. In specific, it would be very beneficial to compare the microstructure resulting from different processes for the same ingredients because it would assist in determining the appropriate process for preparing the material with the desired performance.

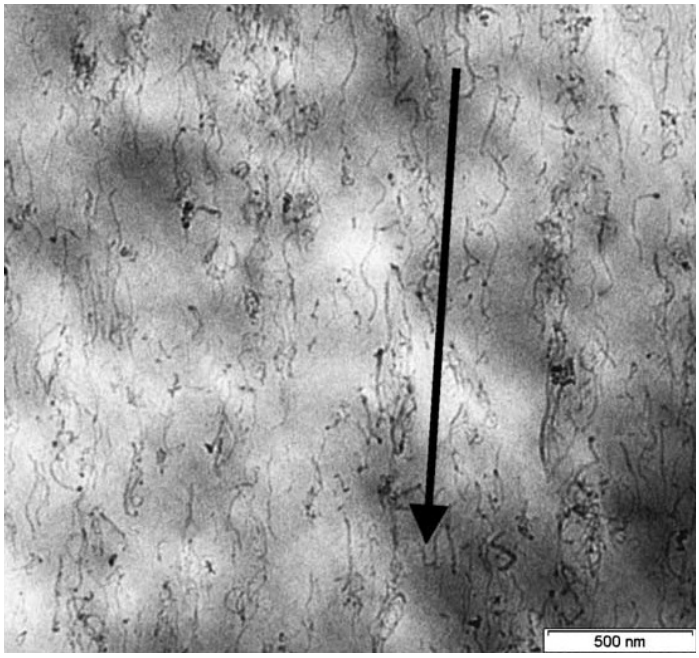

Figure 2.2 A TEM image showing alignment of MWCNTs in PC matrix at high draw down ratios [41].

2.3 Structure – Property Relationships

2.3.1 Electrical Properties

The electrical properties of the polymer composites are significantly higher than those of the neat polymer due to the excellent electrical properties and high aspect ratios of CNTs/CNFs. Composites containing conducting fillers in insulating polymers become electrically conductive when the filler content exceeds a critical value, known as a percolation threshold. The percolation threshold is characterized by a sharp jump in the conductivity by many orders of magnitude which is attributed to the formation of a three-dimensional conductive network of the fillers within the matrix. The percolation threshold is typically determined by plotting the electrical conductivity as a function of the weight or volume fraction of nanotubes and fitting with a power law function (see

figure 2.3). The high aspect ratios of the CNTs/CNFs allow them to form a conductive filler network at low loading, thereby resulting in a low percolation threshold. A wide range of values have been reported for percolation threshold and plateau conductivity of polymer-CNT/CNF composites, depending on the processing method, polymer matrix and nanotube type. A significant uncertainty in the results stems from the reports of percolation threshold in terms of volume fraction because the determination of the true volume fraction of the filler in the composites is not straightforward.

Bai et al [45] found more than an 8-fold decrease in the threshold loading in epoxy-MWCNT composites when the MWCNT length was increased from 1 to 50 μm. Well-dispersed nanotubes generally have higher aspect ratios than nanotube aggregates, so the percolation threshold decreases with better dispersion. Counter examples include work by Bryning et al. [46] where slight aggregation produces a lower percolation threshold by increasing the local interactions between nanotubes. When the nanotubes are highly aligned in the composites, there are fewer contacts between the tubes, which results in a reduction in electrical conductivity and a higher percolation threshold as compared to those in a composite with randomly oriented nanotubes. This topic has been extensively studied by Du et al. [47] using a series of PMMA-SWCNT composites where the degree of nanotube alignment was controlled by the melt fiber spinning conditions and quantified with the full width at half-maximum (FWHM) of the SWNT form factor scattering, where higher FWHM correspond to less SWNT alignment. Similar observations were made by other researchers [36,20,41] too.

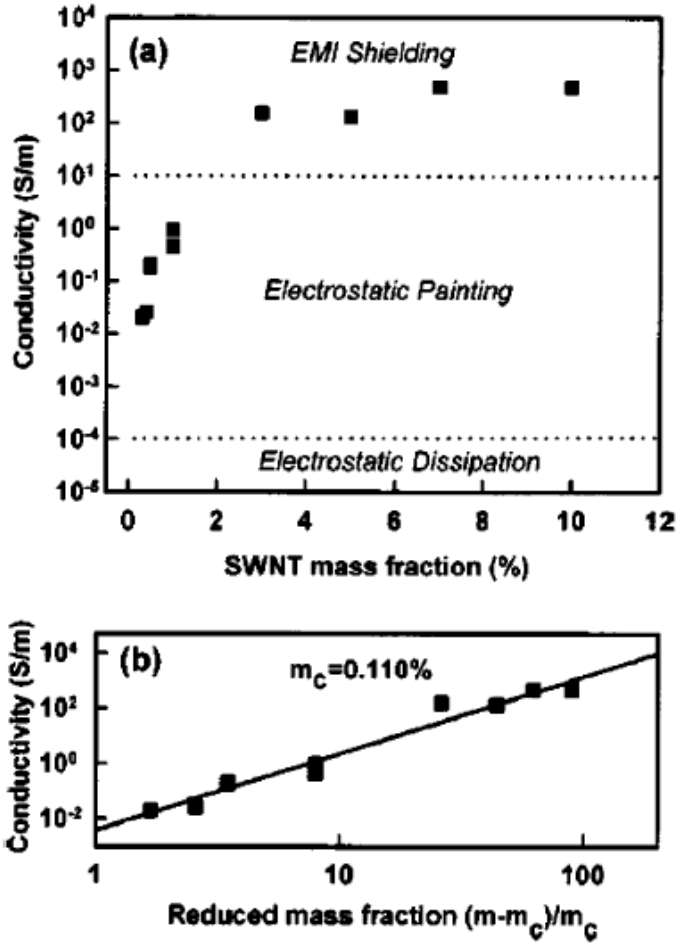

Figure 2.3 Establishing the percolation threshold through power law fits of electrical conductivity as function of weight fraction [48].

The percolation threshold reported for composites of polymer-CNF composites was usually higher than that of polymer-CNT composites. For example, Lozano et al [49] and Gordeyev et al [50] prepared PP-CNF composites via melt mixing and reported the percolation threshold to be 9 wt.% and 5 vol.% respectively.

2.3.2 Rheological Properties

The viscoelastic properties of polymer-CNT/CNF composites have both practical importance related to composite processing and scientific importance as a probe of the

composite dynamics and microstructure. Figure 2.4 shows the typical response of storage modulus (*G*') as a function of frequency for a polymer-CNT/CNF composite with good nanotube dispersion [51]. At high frequencies, the response is not sensitive to the filler loading, indicating that the short-range polymer dynamics are not influenced by the filler. At low frequencies, the rheological behavior progresses from a liquid-like response to a solid-like response (*G*' independent of *w*) as the filler loading increases. Similar, but less predominant trends are typical of loss modulus (*G"*). Applying a power law function to the appropriate rheological parameter as a function of the filler loading provides a rheological percolation threshold corresponding to the onset of solid-like behavior.

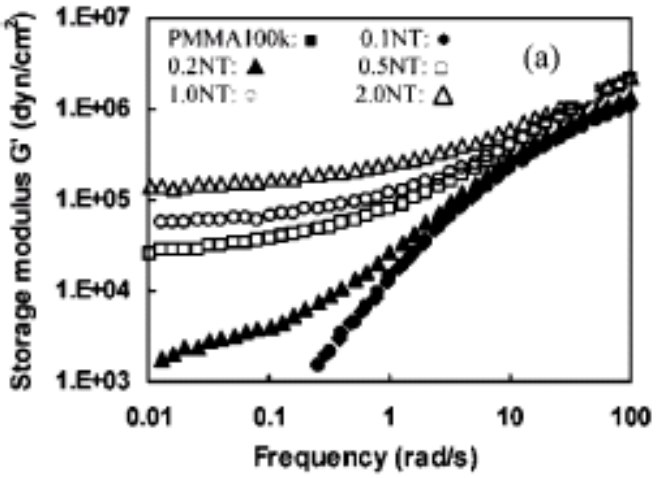

Figure 2.4 Storage modulus vs frequency for PMMA-SWNT composites [51].

Potschke et al. [21] found that the rheological percolation threshold is strongly dependent on temperature. In their PC-MWCNT composite, the percolation threshold decreased from 5 to 0.5 wt % MWCNT upon increasing temperature from 170 to 280 °C. They suggest that the superposition of the entangled polymer network and the combined nanotube-polymer network rather than the nanotube network alone dominates the

rheological properties. In fact, in a set of PMMA-SWCNT composites, Du et al. [10] found that the rheological percolation threshold, 0.12 wt %, was smaller than the percolation threshold for electrical conductivity, 0.39 wt.%. In contrast, Wu et al. [52] reported that the rheological and electrical percolation thresholds are not significantly different from one another.

2.3.3 Thermo-oxidative Properties

The thermo-oxidative properties of the polymer-CNT/CNF composites have been studied to mainly identify their thermal stability and the changes imposed by the presence of CNTs/CNFs on the polymer phase. Mahfuz et al. [22] reported that the thermal decomposition temperature of composites of Nylon with very low mass fraction of MWCNTs is significantly higher than the neat Nylon. Furthermore, they also reported similar behavior in various other nanoparticle reinforced polymers [53,54]. Xu et al. [55] conducted a thorough work on the thermo-oxidative behavior of PS-CNF composites and concluded that temperature at peak weight loss rate increases more significantly at lower loadings than higher loadings of CNFs when compared with the neat PS. They also reported that the CNFs in the nanocomposites decompose at a lower temperature compared to the pristine CNFs. Chatterjee et al. [56] studied the thermal and thermo-oxidative behavior of PP-CNF composites in nitrogen and air respectively. They reported that the degree of enhancement in thermal stability of the composites compared to the neat PP is more prominent in the presence of air, possibly due to the formation of a char layer that acts as a physical barrier between the uncombusted polymer and combustion zone. Similar observations about the increase in the thermal stability of the PP-CNF

[57,58] and polyol-CNF composites were reported in literature and they were attributed to the restriction in the mobility of the macromolecules imposed by the CNFs. In contrast, a few reports on epoxy-CNF composites in literature indicate either no influence [59] on or a slight decrease [60] in the thermal stability with increasing CNF loading.

2.3.4 Mechanical Properties

The strength of discontinuously-reinforced composites typically depend on two structural characteristics: *interfacial adhesion* and *dispersion*. First, there should be a high degree of load transfer between the matrix and the discontinuous reinforcement such as the nanoscale fillers. When the interfacial adhesion between the phases is weak, the nanoscale fillers behave as holes or nanostructured flaws, inducing local stress concentrations and reducing the transfer of the CNT/CNF properties to the matrix material. Second, the CNTs and CNFs should be well dispersed. If poorly dispersed, the CNTs/CNFs will fail by separation of the bundle rather than by failure of the individual CNTs/CNFs themselves. This may result in significantly reduced strength.

The outstanding potential of the SWCNTs to adhere to polymer matrices has been evident from the super tough composite fibers fabricated by Dalton et al. [61]. By optimizing the coagulation spinning method, they spun several hundred meters of composite fibers of PVA-SWCNT composites at 60 wt. % loading, which had a tensile strength of 1.8 GPa, comparable to that of a spider silk. Wagner et al [62] found that the average interfacial stress required to remove a single MWCNT from the polyethylenebutene matrix is 47 MPa, which is about 10 times larger than the adhesion level between the same type of polymer and CNFs; this example demonstrates the

importance of filler size on the interfacial strength. It suggests a good bonding between CNTs and polymer matrix. Therefore, efforts are underway to better understand the mechanism of interfacial adhesion at the molecular level to further optimize the interface in nanocomposite systems.

To date, the main challenges have been to improve the dispersion of CNTs/CNFs in a polymer matrix when processing these nanocomposites. To maximize the advantage of CNTs/CNFs as effective reinforcements in high strength composites, they should not form aggregates and must be well dispersed to prevent slippage. However, the problem is that CNTs/CNFs easily agglomerate, bundling together and entangling, leading to many defect sites in the composites, and limiting the efficiency of CNTs/CNFs on polymer matrices. Salvetat et al. [63] studied the effect of dispersion of CNTs on the mechanical properties of polymer-CNT composites, and found that poor dispersion and rope-like entanglement of CNTs led to drastic weakening of the composites.

To enhance the dispersion and improve mechanical properties, Gong et al. [29] used a non-ionic surfactant, polyoxyethylene-8-lauryl, and showed that with only 1 wt.% CNTs in the epoxy-CNT composites the elastic modulus increased by over 30%. Adding 1 wt.% MWCNTs in the PS-MWCNT composite films by the solvent processing, results in 36% and 25% improvements in tensile modulus and break stress, respectively. Andrews et al. [6] prepared drawn isotropic petroleum pitch-SWCNT composite fibers with 5 wt.% SWCNTs. The tensile strength, modulus and electrical conductivity of these pitch composite fibers are enhanced by ~90, ~150 and ~340%, respectively, due to the orientation of the SWCNTs. In general, the stiffening effect of CNTs/CNFs appears to be more prominent in semicrystalline rather than amorphous thermoplastics, possibly due to

the nucleation effects [31]. Although a linearly increasingly composite stiffness has been observed up to 15 wt.% of nanofibres [40], in many cases, a non-linear relationship is observed with increasing filler loading fraction.

While there has been much effort to understand and control the adhesion and dispersion of CNTs/CNFs in polymer matrices, there are still a wide range of improvements in mechanical properties being reported in the literature. Safadi et al. [14] found that at less than 1 vol.% of MWCNTs, there is a 40% increase in strength of PS-MWCNT composites. The modulus improved by a factor of 2 with respect to the neat polymer when 2.49 vol.% of CNTs were added. Tibbetts et al. [38] indicated that the addition of CNFs to a PP matrix had no effect on tensile strength, probably because of the increased brittleness of the polymer matrix, which resulted from PP's inability to further crystallize on deformation, a behavior due to the molecular restrictions caused by the fiber dispersion. At 5 wt.% CNF loading, modulus and compressive strength of the spun PP increased by 50% and 100%, respectively. Comparable loading fractions of MWCNTs, rather than CNFs, in both solution-cast [14,17] and extruded PS films, produced a more pronounced stiffness enhancement, indicating that the crystalline quality of the nanoscale filler contributes to the overall performance of the nanocomposite. Similarly, comparisons of different types of filler in PA-12 composite fibres showed that well-dispersed CNTs produce a greater improvement in stiffness than CNFs, but that the type of nanotube also has an effect [37]. In addition, a direct comparison of aligned versus unoriented nanotubes showed a significant enhancement of the composite stiffness for the aligned nanotubes [36].

In summary, none of the polymer-CNT/CNF composites fabricated so far at low filler loadings demonstrated enormous increases in mechanical properties. Thus, in order to truly realize high performance composites using these nanoscale fillers, it is important to understand the fundamental reinforcement mechanisms via the structure-property relationships. Eitan et al [64] present a thorough micromechanics model of the polymer-CNT/CNF composites suggesting that the high performance composites are possible only at high filler loadings.

2.4 Processing – Property Relationships

Most of the polymer nanocomposites works reported in literature, some of which are reviewed in 2.1-2.3, were processed by a specific technique to establish the processing-microstructure and the structure-property relationships, without much emphasis on investigating the processing-property relationships, i.e., influence of the type of process or processing parameters on the resulting properties. In novel material development, establishing the processing-property relationships is as important as establishing the processing-microstructure and structure-property relationships. There have been very few investigations, however, that attempted to address the processing-property relationships. Andrews et al. [6] compared the polymer-MWCNT composites that were processed by simple shear mixing with bench-scale extrusion and observed that extrusion aligns the MWCNTs, thereby increasing the electrical percolation threshold by at least an order of magnitude. Potschke et al [41] observed a similar decrease in electrical conductivity of extruded PC-MWCNT composites due to alignment at high draw down ratios. Furthermore, they reported a slight increase in the Young's modulus

and a slight decrease in % elongation to failure of the PC-MWCNT composites at high draw down ratios. However, they also report that similar behavior was observed in neat PC, thereby indicating that the observed property differences are mainly due to change in the microstructure of neat PC. Gallant et al. [65] quantitatively studied the burning rate in energetic microcomposites as a function of the screw speed and the screw design. Huang at al [66] prepared polydimethyloxane-MWCNT composites using a simple shear mixer and investigated the rheological properties of the composites as function of the mixing time. They reported that the viscosity of the composites exhibits an erratic behavior until a characteristic mixing time is reached when the dispersion of the MWCNTs in polydimethyloxane is reproducibly uniform. They claimed that the characteristic time, which is specific to each process, should be such that total energy supplied should be higher than van der Waals forces of attraction, which were reported to be ~10^{-4} J/m^3. In summary, there is a significant need for thoroughly investigating the processing-property relationships of polymer nanocomposites.

2.5 Processing – Structure Relationships: Extruded Polymer Composites

Conventional batch approaches to characterize the processing-structure-property relationships in polymer nanocomposites can be very time consuming. Approaches based on combinatorial materials science allow rapid characterization of both processing-structure and structure-property relationships. The following sections provide a review of the research conducted to rapidly characterize compositional gradients (i.e., structure) via combinatorial approaches, especially suited to extrusion.

2.5.1 Compositional Gradients for a Combinatorial Approach

TSE process is ideally suited for producing continuous compositional gradients [31]. Operating a twin screw extruder at one steady condition and dynamically changing the ingredient input proportions to produce a new formulation results in the extrudate changing from the original composition to a second one. Due to the inherent back mixing in the extruder, an abrupt change in ingredient addition results in a more gradual change in the composition of the extrudate. In this way, the continuous nature of the process is especially well suited to combinatorially [67-69] produce polymer nanocomposites. In contrast, the batch process is incapable of producing a smooth continuous transition. It is also be possible to vary the screw configuration of the extruder to alter and optimize the characteristics of the gradient architecture.

Gilman et al [31,70,71] produced extruded composites of Nylon6 or PS and purified organo-clay filler with specific emphasis on the combinatorial nature of the compositional gradients (CGs). They indicated that a single experiment can provide samples for in situ or a posteriori characterization over the entire compositional domain of interest. This significantly reduces the batch-to-batch variation and the time consumed in producing the samples at various compositions. Eidelman et al [72] produced thin film CGs of poly (L-lactic acid) with poly (D,L-lactic acid) using a three syringe pump system. Potyrailo et al [73] used a combinatorial extrusion system to generate polymeric CGs with two different material systems – PP with model additives and PC with titanium dioxide filler. However, in order to develop the combinatorial approach the CGs should not only be produced, but also rapidly characterized. Eidelman et al. [72] developed an elaborate fourier transform infrared microspectroscopy technique that monitors the

reflection-transmission spectra to obtain the composition. Potyrailo et al. [73] characterized the CGs in situ by using an optical probe signal that tracks the changes in color of the blend. However, all of the non-destructive in situ characterization approaches developed so far with optical probes are limited to low loadings of the filler in the composite. At higher loadings, especially of dark colored fillers, the optical probes tend to reach their saturation, i.e., detection limit. Furthermore, most of the prior works conducted to rapidly determine the CGs require a pre-calibration of the technique with known composition, thereby decoupling the processing from the evolution of the CG (i.e., structure).

In order to rapidly characterize such CGs, the effect of the transient variations in the ingredients and the operating conditions for a given screw configuration must be modeled i.e., the processing-structure relationship has to be established. Typically, the compositional variation in a graded composite can be described using a power law relation as follows:

$$V=(x/t)^p \tag{2.1}$$

where V is the volume fraction of one phase, x is the distance along the graded region (known as the *interlayer*), t is the thickness of the interlayer, and p is the gradient exponent. However, it does not give a complete description of processing-structure relationship. In order to establish the processing-structure relationship, it is necessary to understand the mixing characteristics in the twin screw extruder.

2.5.2 Residence Distributions as Measures of Mixing

Since the flow in the extruder is highly non ideal due to channeling, back-mixing and stagnation, obtaining a complete knowledge of the flow patterns that govern mixing is impractical [74]. Conventionally, mixing in extruders is understood via residence time distribution (RTD), which is a measure of the how long the material takes to pass a given point [75]. The corresponding concept in the volume domain is called a residence volume distribution (RVD), i.e., it is a measure of the volume of the material that passes a given point. These distributions are typically expressed as normalized functions of time and volume in the following forms:

$$\bar{f}(t) = \frac{f(t)}{\int_0^\infty |f(t)|\, dt} \tag{2.2}$$

$$\bar{g}(v) = \frac{g(v)}{\int_0^\infty |g(v)|\, dv} \tag{2.3}$$

where,

$$v = t \times Q \tag{2.4}$$

and $\bar{f}(t)$ is the normalized RTD, $\bar{g}(v)$ is the normalized RVD, Q is the throughput, t is time, v is volume, and f and g are the response functions associated with the amount of material that passes a given point in the extruder at the time, t, or along with a volume, v. In an earlier experimental work, Elkouss et al [76] confirmed that in an extruder with a fixed screw design, in spite of varying the polymer flow rates and extruder screw speeds, all the normalized RVDs superimpose (see figure 2.5) to form a single master curve, as long as the elastic effects were not predominant.

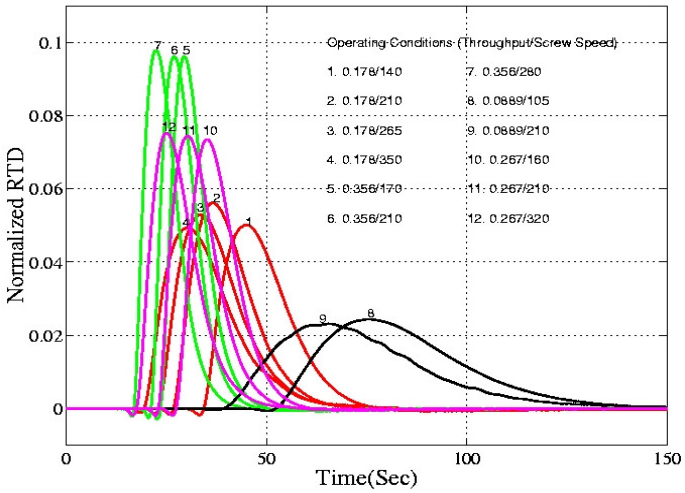

(a)

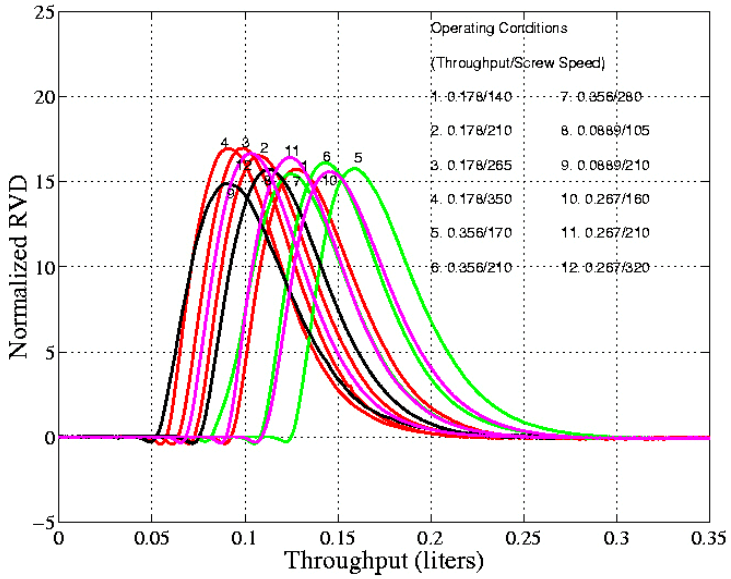

(b)

Figure 2.5 The (a) RTDs, and (b) RVDs at varying operating conditions. Note that the RVDs overlap, while the RTDs do not overlap [76].

This indicates that as long as the Weissenberg number is less than one, the normalized RVD can be used as a characteristic of the process that is independent of processing conditions.

3. Experimental Methods

The ingredients, equipment and procedures used for processing and characterization of polymer composites are explained in the following sections.

3.1 Ingredients

There are three kinds of ingredients utilized in this research investigation: (1) polymer matrix, (2) fillers, and (3) solvents. Impact modified Polystyrene was chosen as the polymer matrix material because it is a regular commodity plastic that can easily be processed using both solvent processing and extrusion. The nanoscale fillers, multi-walled carbon nanotubes and carbon nanofibers, were the primary motivation for this research investigation. An inexpensive, microscale filler, potassium chloride, was used to check the validity of the combinatorial approach developed across various size scales. Two different solvents, tetra-hydro furan and di-methyl formamide, were chosen because their potential for dissolving PS and dispersing the fillers.

3.1.1 Polymer Matrix

The impact modified Polystyrene (PS) (molecular weight ~ 150,000, polydispersity ~ 2.73) was obtained from Nova Chemicals Inc. It is a copolymer of styrene and butadiene and is used primarily in toys and product casings. While the styrene-rich phase provides the stiffness, the butadiene-rich phase provides the toughness, thereby improving its impact strength. The ease of processing with no pre-drying requirements makes PS a good model material for studying the processing-structure-

property relationships in polymer-CNT/CNF composites. The following is a list of properties of PS as provided by the manufacturer:

PS (Polystyrene,$(C_8H_8C_4H_6)_X$)
Vicat Softening Temperature: 91 C
Electrical Conductivity: 10^{-20} S/m
Specific Gravity: 1.04
Recommended Melt Temperature: 190-230 C
Thermal Decomposition Temperature: ~250 C
Tensile Modulus: 2.0 GPa
Tensile Strength: 16 MPa
Elongation to failure: 15%

3.1.2 Fillers

3.1.2.1 Graphitized Multiwalled Carbon Nanotubes

The graphitized Multiwalled CNTs (MWCNTs) were obtained from the University of Kentucky. The MWCNTs were vapor grown through the catalytic decomposition of a ferrocene–xylene mixture at 675°C in a quartz tube reactor and over quartz substrates, with a conversion of 25% of the total hydrocarbon feedstock [77]. The MWCNTs were further purified by annealing at 3000°C, i.e., graphitized, to remove the catalyst particles and microstructural defects as well as increase the thermal stability of the MWCNTs [78,79]. The manufacturer did not provide the properties, however some general characteristics of MWCNTs are as follows [1]:

MWCNT
Diameter: 10-50 nm *Length*: 5-10 micrometer *Tensile Modulus*: 3-30 GPa for defective MWCNTs from a CVD process, and 1 TPa for defect-free MWCNTs from an electric arc process. *Cost*: $50,000/Kg

The as-received MWCNTs were characterized using a scanning electron microscope (SEM) as shown in figures 3.1-3.3. The as-received MWCNTs were significantly agglomerated (~100 μm). This can be expected due to the high van der Waals attractions in nanoscale fillers due to their high surface area. This is especially true with MWCNTs due to the delocalized electron cloud on their surface that allows induced dipoles easily.

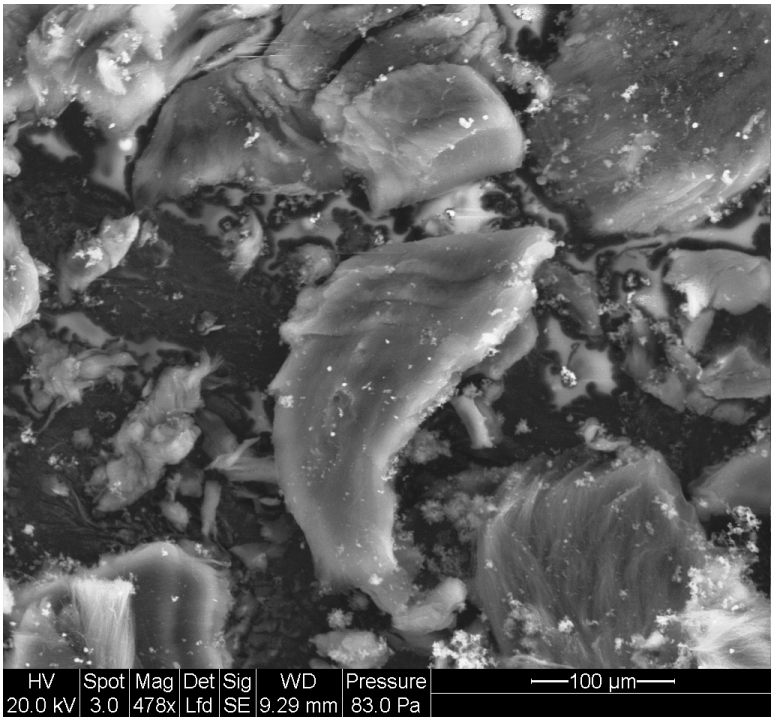

Figure 3.1 Scanning electron micrograph showing the as-received MWCNTs with large agglomerations.

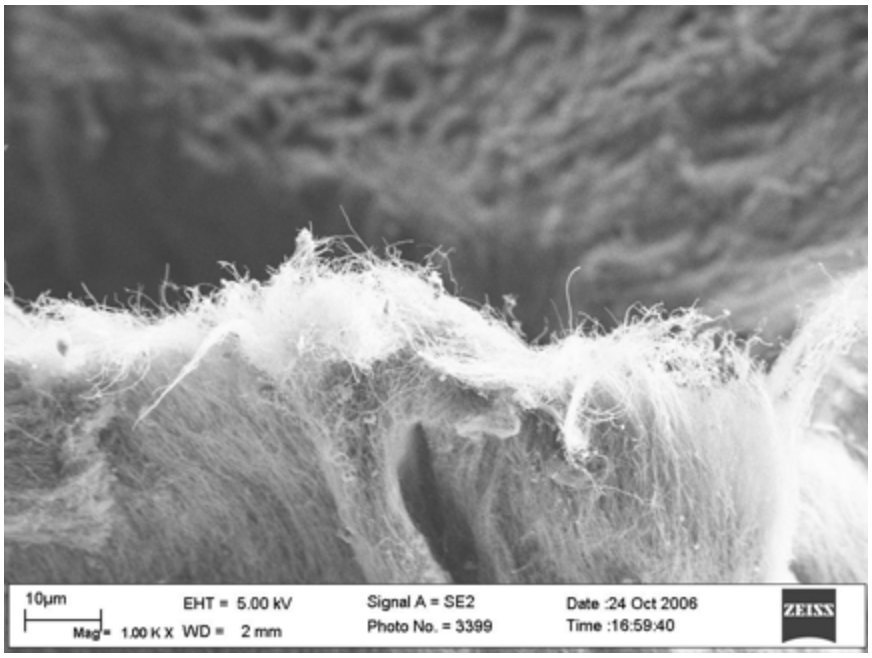

Figure 3.2 Scanning electron micrograph showing a single agglomerate of MWCNTs.

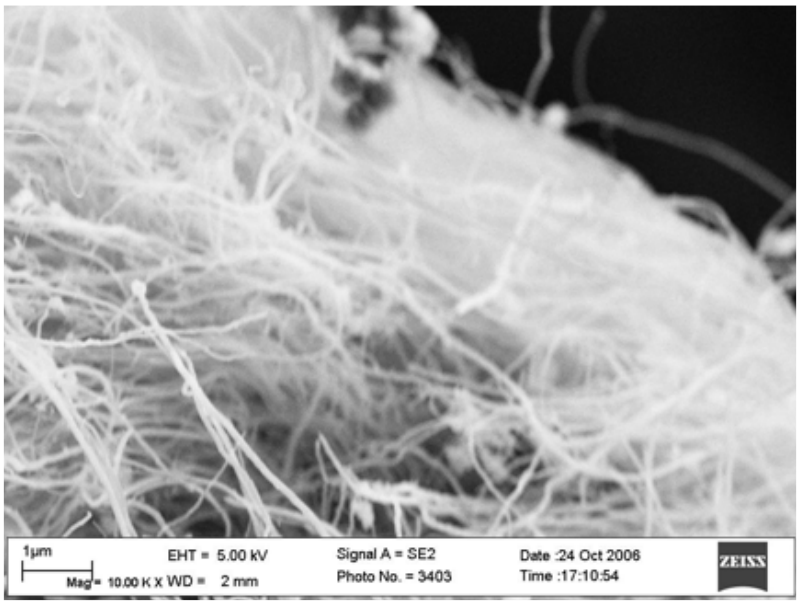

Figure 3.3 Scanning electron micrograph showing the individual MWCNTs, which are tens of nanometers in diameter.

The MWCNTs were also characterized using the x-ray fluorescence spectroscopy to study the elemental composition. Figure 3.4 below shows the spectrum of MWCNTs with

the sample holder and figure 3.5 shows the spectrum of the sample holder only. Comparing the two images, it can be concluded that the sample does not contain any contaminants.

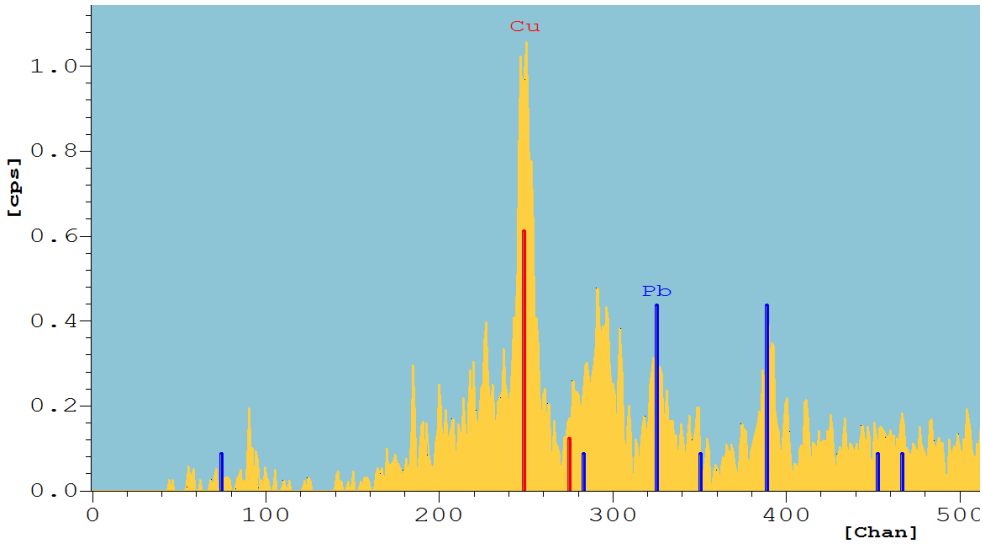

Figure 3.4 Spectrum of MWCNTs on the sample holder.

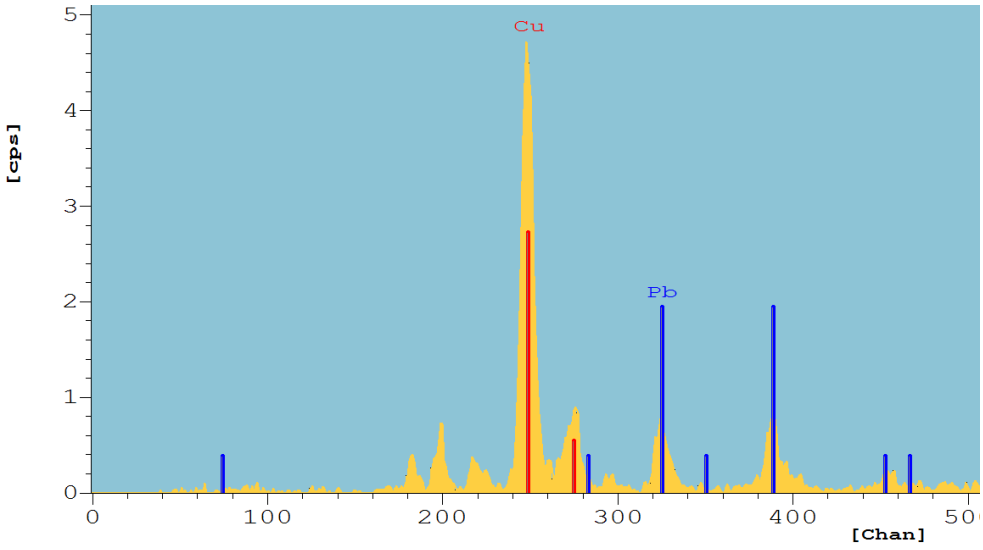

Figure 3.5 Spectrum of the sample holder only.

Furthermore, the MWCNTs were characterized using Raman spectrometry to study the nature of chemical bonding (see figure 3.6). Typically, single-wall carbon nanotubes (SWCNTs) consist of three major types of Raman bands: the low frequency bands around 160 – 200 cm^{-1}, intense peaks around 1500 – 1600 cm^{-1}, and bands around 1350 cm^{-1}, which are due to defects in the nanotubes. Figure 3.7 shows the typical Raman spectra of graphite powder with a more intense peak around 2570 cm^{-1} and less intense peaks at 1278 – 1291 cm^{-1} and 1591 – 1600 cm^{-1}. Thus figure 3.6 indicates that the MWCNTs show the low frequency bands similar to SWCNTs and that the MWCNTs show strong indications of graphitization. Furthermore, the presence of several other peaks indicates that the MWCNTs may contain a few gross defects that were not removed upon graphitization.

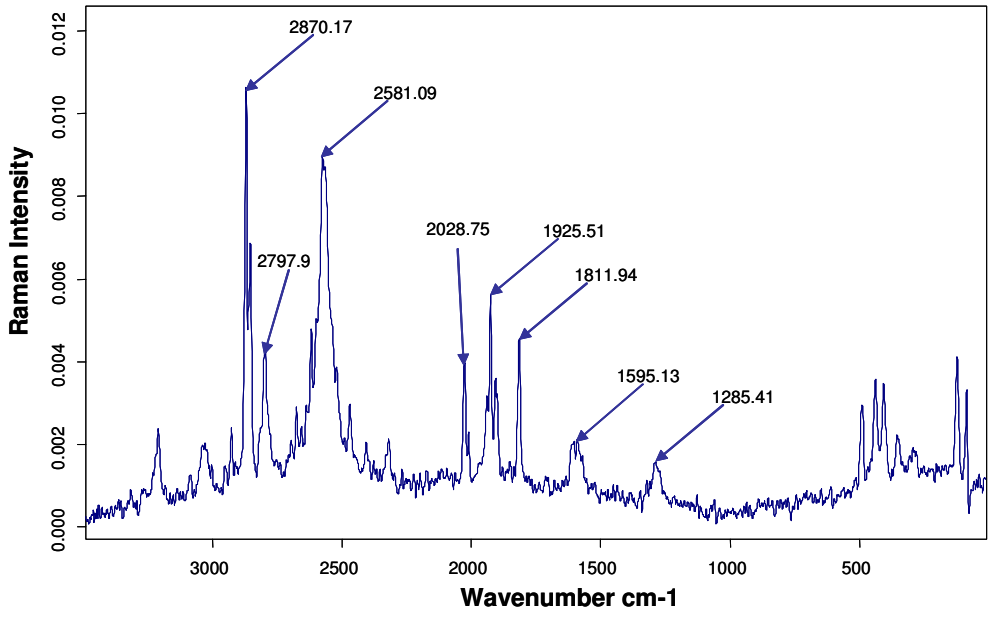

Figure 3.6 Raman spectra of MWCNTs shows that they are graphitized.

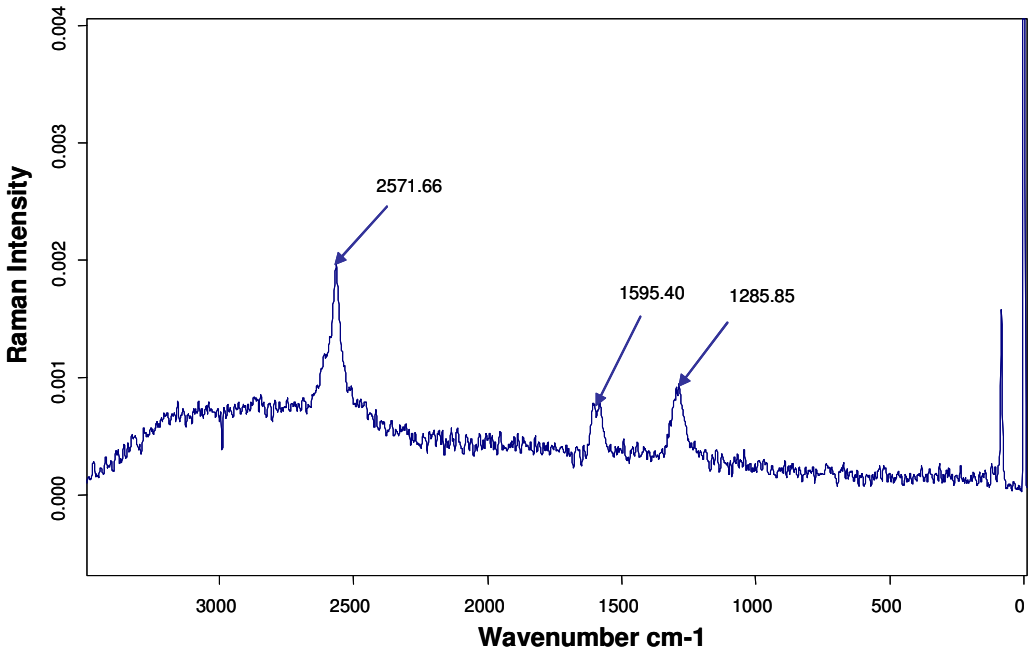

Figure 3.7 Raman spectra of graphite powder.

3.1.2.2 Pyrograf III Carbon Nanofibers

The Pyrograf®-III Carbon Nanofibers (CNFs) were obtained from Applied Sciences Inc. The CNFs were vapor grown to be much smaller than the conventional continuous or milled carbon fibers (~10 μm), but significantly larger than MWCNTs (~10 nm). Furthermore, the CNFs obtained were heat treated to remove the aromatics and partially organize the non-graphitic carbon. However, they still contain little quantities of iron catalyst and amorphous CVD carbon. CNFs are more affordable than the MWCNTs, and hence better suited for process development. The following is a list of properties and cost of the CNFs as provided by the manufacturer:

CNF
Diameter: 100-200 nm *Length*: 5-10 μm *Cost*: $500/Kg

The CNFs received were characterized using a scanning electron microscope (see figures 3.8-3.11). Similar to the MWCNTs, it was observed that the as-received CNFs were significantly agglomerated (~100 μm).

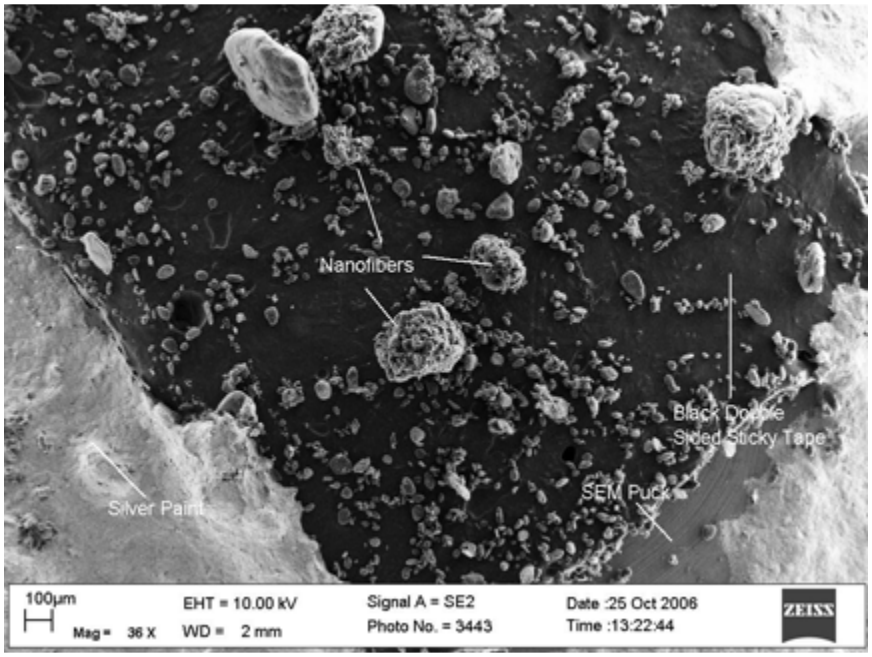

Figure 3.8 Scanning electron micrograph showing the as-received CNFs. Note that most of the agglomerates are several tens of microns.

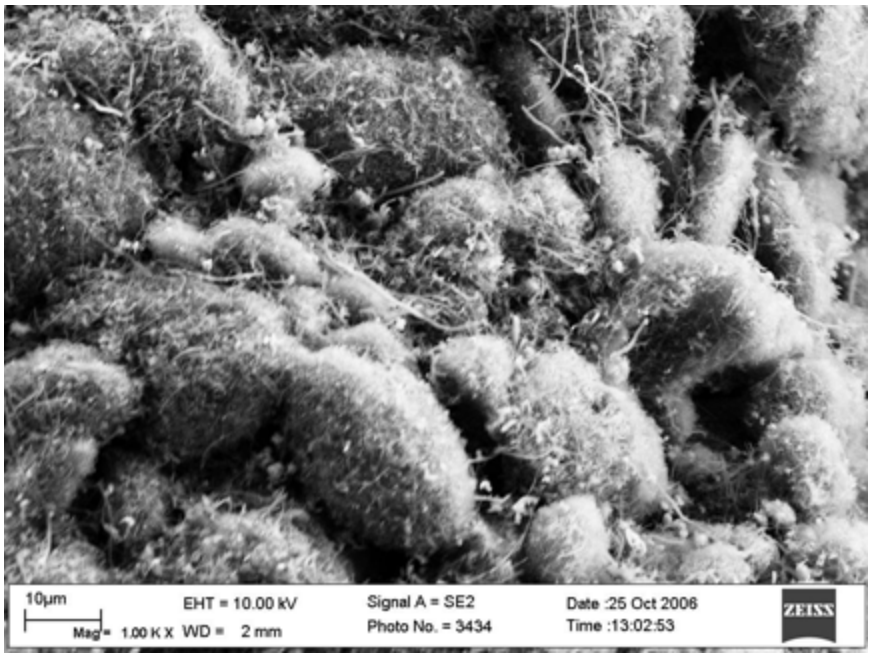

Figure 3.9 The as-received CNF agglomerates at a higher magnification.

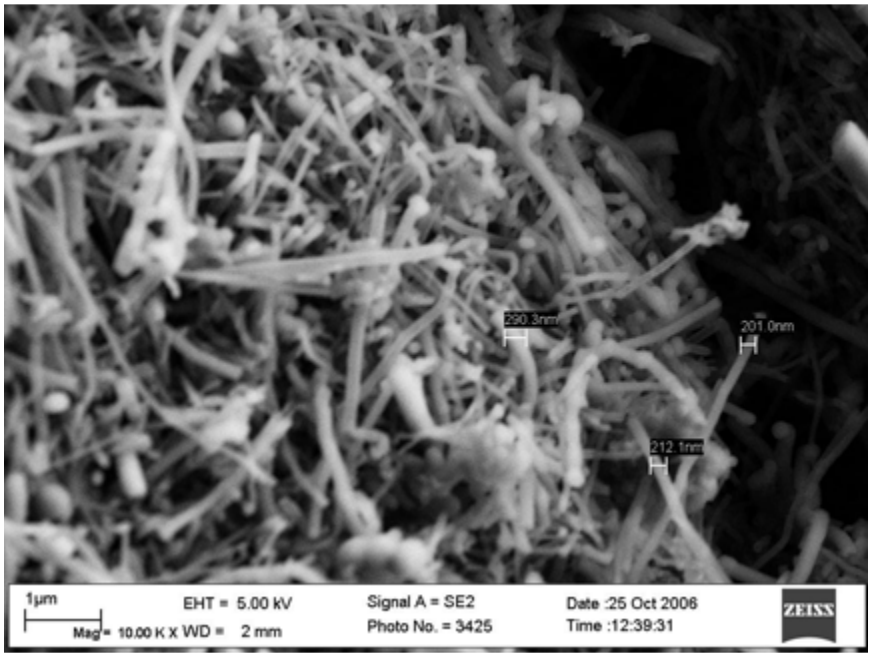

Figure 3.10 The diameter of the as-received CNFs is on the order of 100micrometer.

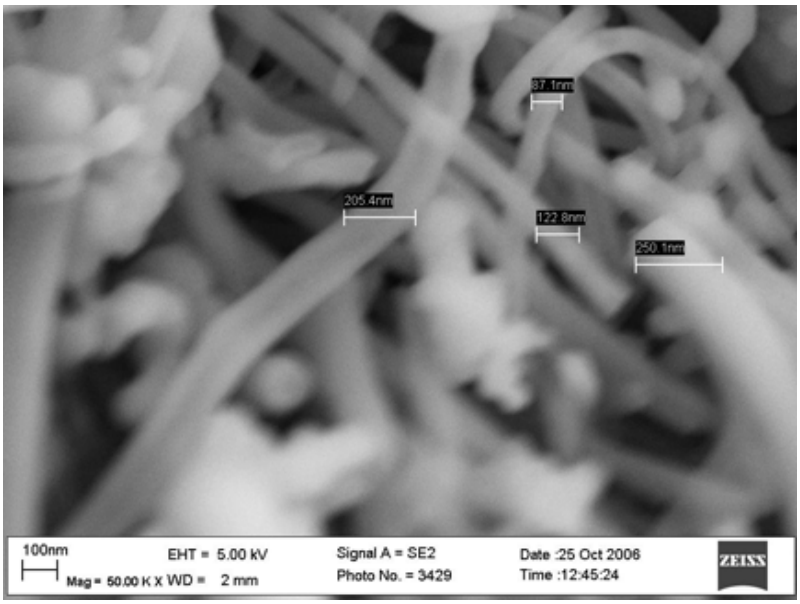

Figure 3.11 The as-received CNFs at a higher magnification.

The CNFs were also characterized using the x-ray fluorescence spectroscopy to study the elemental composition. Figure 3.12 shows the spectrum of CNFs with the sample holder and figure 3.13 shows the spectrum of the sample holder only. Comparing the two spectra, it can be concluded that the sample does not contain copper, but contains iron, which is the catalyst used during the synthesis.

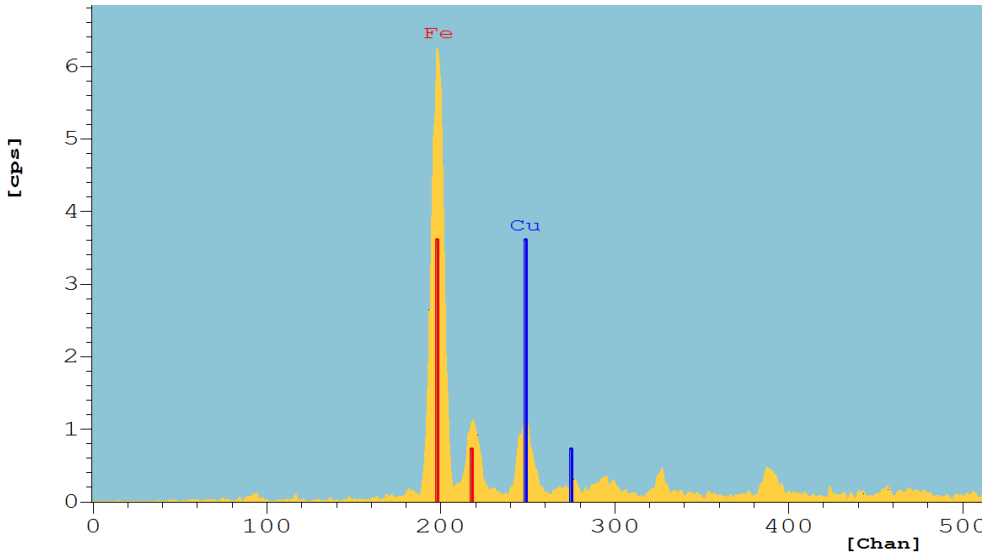

Figure 3.12 Spectrum of the CNFs with the sample holder

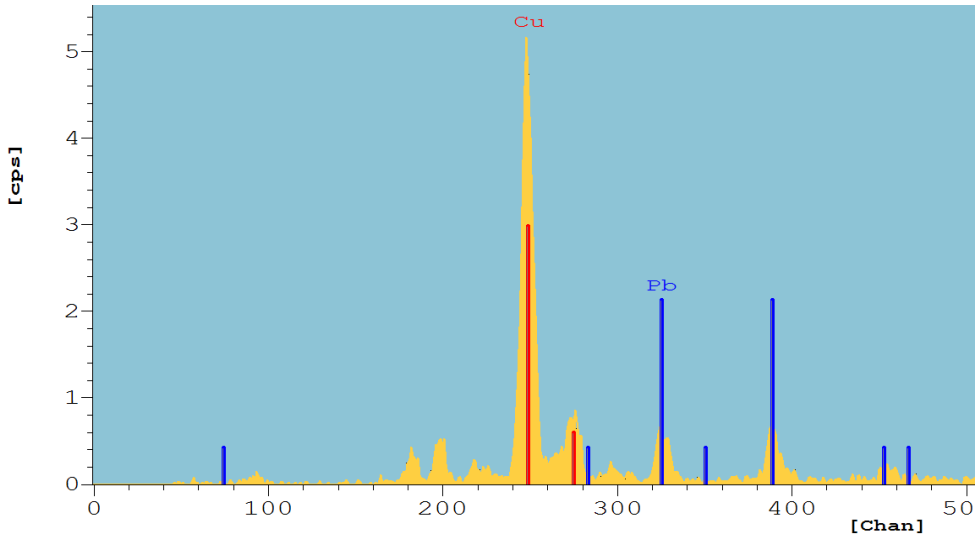

Figure 3.13 Spectrum of the sample holder only.

Furthermore, the CNFs were characterized using Raman spectrometry to study the nature of chemical bonding. The CNFs exhibited several peaks uncharacteristic of the MWCNTs indicating that they are significantly different in nature (see figure 3.14). This could be possibly due to the existence of several microstructural defects in CNFs.

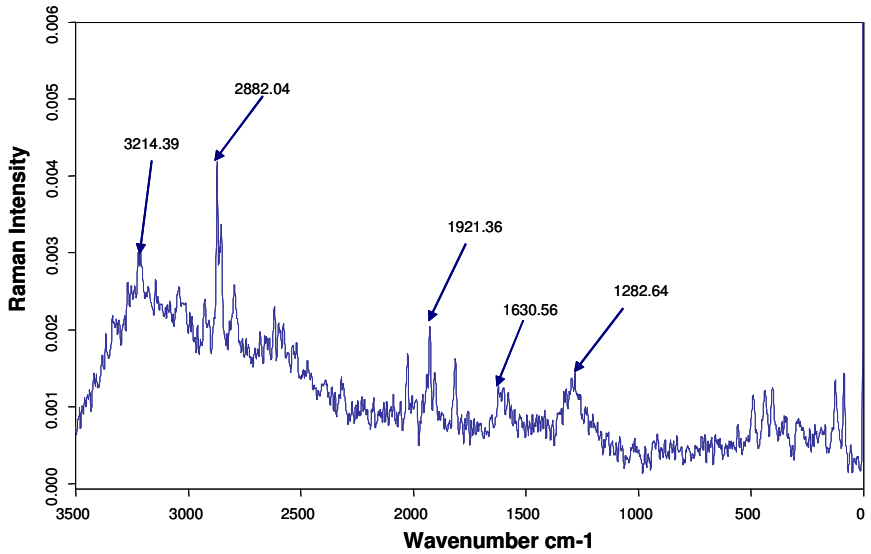

Figure 3.14 Raman spectra of CNFs shows that they are distinctly different from MWCNTs.

CNFs of two different bulk densities, low density (LD) and high density (HD), were used. While both of them exhibited similar agglomerates, elemental composition and chemical bonding, they differed in their aspect ratio. The average aspect ratio of the CNF LD and CNF HD were 50: 1 and 25:1, respectively.

3.1.2.3 Potassium Chloride

Technical grade potassium chloride (KCl) microparticles were obtained from NAVSEA-IHMD. This material was screened through a U.S. sieve size #60 corresponding to screen openings of 250 μm. The material passing through the 250 μm screen was used. KCl was used as a dummy filler to check the validity of the combinatorial approach developed across various size scales. Furthermore, it is inexpensive and allows quick characterization of the composition via thermal decomposition because the decomposition temperatures of PS and KCl are significantly different unlike PS and MWCNTs or CNFs.

3.1.3 Solvents

Research grade N,N di-methyl formamide (DMF) and tetra-hydro furan (THF) were obtained from Fisher Scientific. They were suggested to be good dispersants for MWCNTs [46,80] and hence used in this work study the effect of solvent on the material properties. The following are a few properties of DMF and THF as obtained from the manufacturer:

DMF (C_3H_7NO)	THF (C_4H_8O)
Specific Gravity: 0.94 *Boiling Point*: 153°C	*Specific Gravity*: 0.89 *Boiling Point*: 66°C

3.2 Processing of Polymer Nanocomposites

The polymer nanocomposites were processed using two different techniques: *solvent processing* and *twin screw extrusion* to compare the effect of processing on the structure-property relationships. Each of these techniques will be discussed in detail in the following sections.

3.2.1 Solvent Processing

The purpose of solvent processing is to create samples equivalent to the extruded version by using a minimum amount of MWCNTs/CNFs in a lab-scale, batch process. Known amounts of the filler and PS were measured to obtain the desired loading of filler in the composite. The desired solvent is added to two different beakers containing PS and the filler to make a 1 wt.% suspension and 5 wt.% solution respectively. The suspension of filler in the solvent is sonicated in an VWR 75D sonicator for ~2 hours. During the sonication the beaker is covered with a lid or an aluminum foil to avoid evaporation of the solvent. This is particularly essential for solvents with high vapor pressure such as THF. Simultaneously, in a separate beaker PS was dissolved in the solvent by stirring as shown in figure 3.15. The filler suspension was then mixed with the PS solution and allowed to stir covered for ~2 hours. As noted in an earlier work [46], it was observed

that periodic addition of solvent produced better dispersion. Subsequently, the solvent was allowed to evaporate leaving behind the polymer nanocomposite.

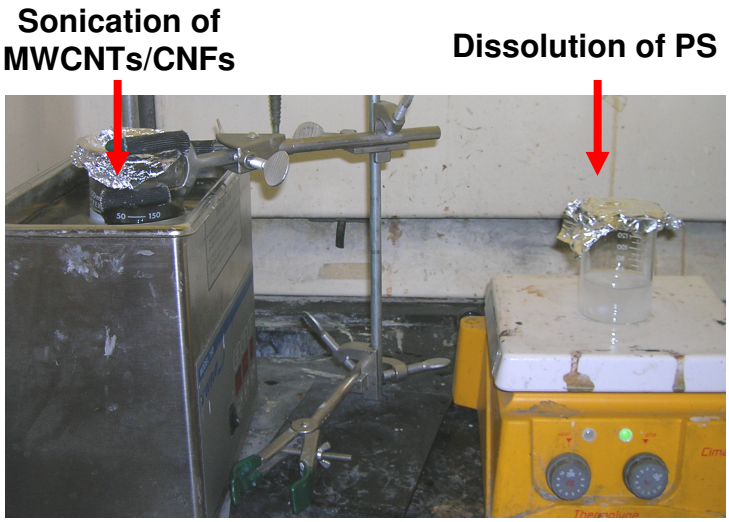

Figure 3.15 The solvent processing experimental setup showing the sonication of filler suspension and dissolution of polymer in the same solvent.

THF evaporates easily due to its high vapor pressure, but DMF usually requires solvent extraction. For solvent extraction, the mixture of filler suspension and the PS solution was gradually added into stirred water (non-solvent for PS) until all the polymer nanocomposite precipitates. The solvent extraction should be done gradually because it allows for the solvent (THF or DMF) to diffuse into the non-solvent phase leaving behind the polymer nanocomposites precipitate. The resultant mixture is filtered using a water aspirator-based vacuum filtration, as shown in figure 3.16, to obtain the precipitate. The PS-filler composite is then placed on a watch glass and dried in a vacuum oven for 12-24 hours at 100°C for the solvent to evaporate from the composite. Finally, the dried composite is hot-pressed into a 30 mm diameter disc specimen for electrical and rheological property characterization using a Beuhler Pneumet I hot press (see figure

3.17) at a temperature of 150°C under a pressure of 85 psi. Samples with various mass fractions of filler in PS were prepared by this method.

Figure 3.16 The vacuum filtration setup to separate the polymer nanocomposite precipitate after solvent extraction.

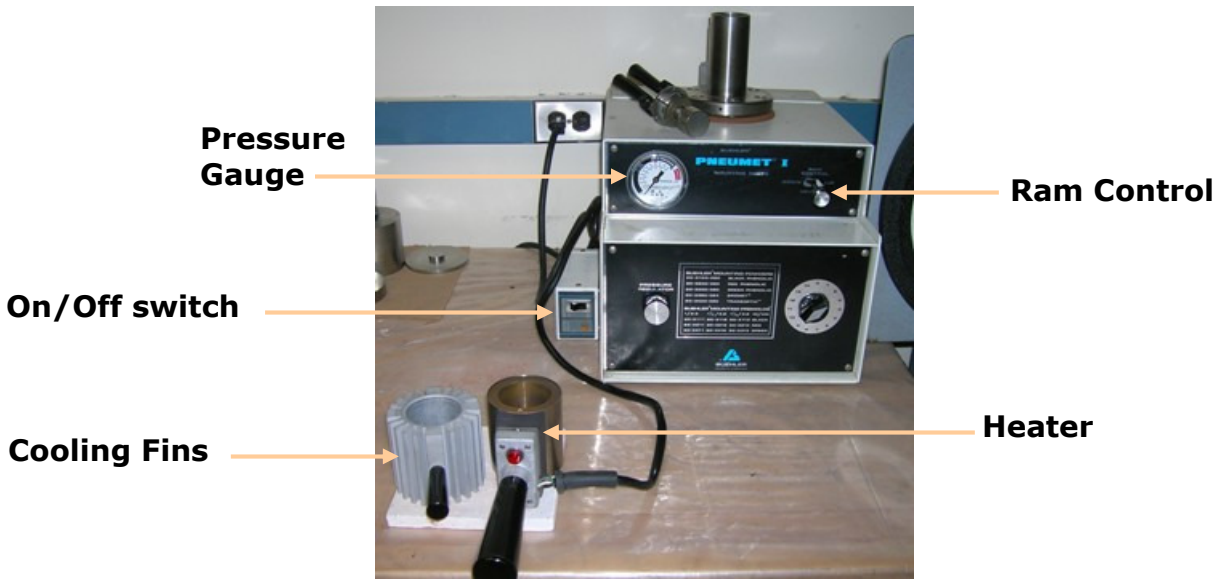

Figure 3.17 The Beuhler Pneumet I Hot Press

3.2.2 Twin Screw Extrusion

TSE is a type of melt mixing process that is utilized to manufacture a number of consumer and industrial goods, from snack foods and medical tubing to plastic pellets and military propellants. The process is a continuous type in that the twin screw extruder will produce a product as long as the ingredient supply is maintained. Because this type of process has so many advantages over batch type, it has found widespread utility across diverse industries. For most however the advantages are universal: economy, quality, environment, flexibility, and safety. Some of these advantages illustrate why the twin screw extruder shows great promise for producing functionally graded materials.

Furthermore the continuous process yields a more consistent product thus improving overall quality. There is significantly less variation in material, and the efficiency of mixing is better than batch methods. The process lends itself to on-line analysis allowing for the quick detection of anomalous conditions or material automatically diverting it to waste.

3.2.2.1 Equipment & Peripherals

For this research investigation, the TSE facility in the polymer processing laboratory at the University of Maryland was used. A laboratory scale Werner & Pfleiderer model ZDSK-28 twin screw extruder with co-rotating, fully-intermeshing screws was the focal point of the experimental set-up. The extruder and the related peripherals are shown in figures 3.18 and 3.19.

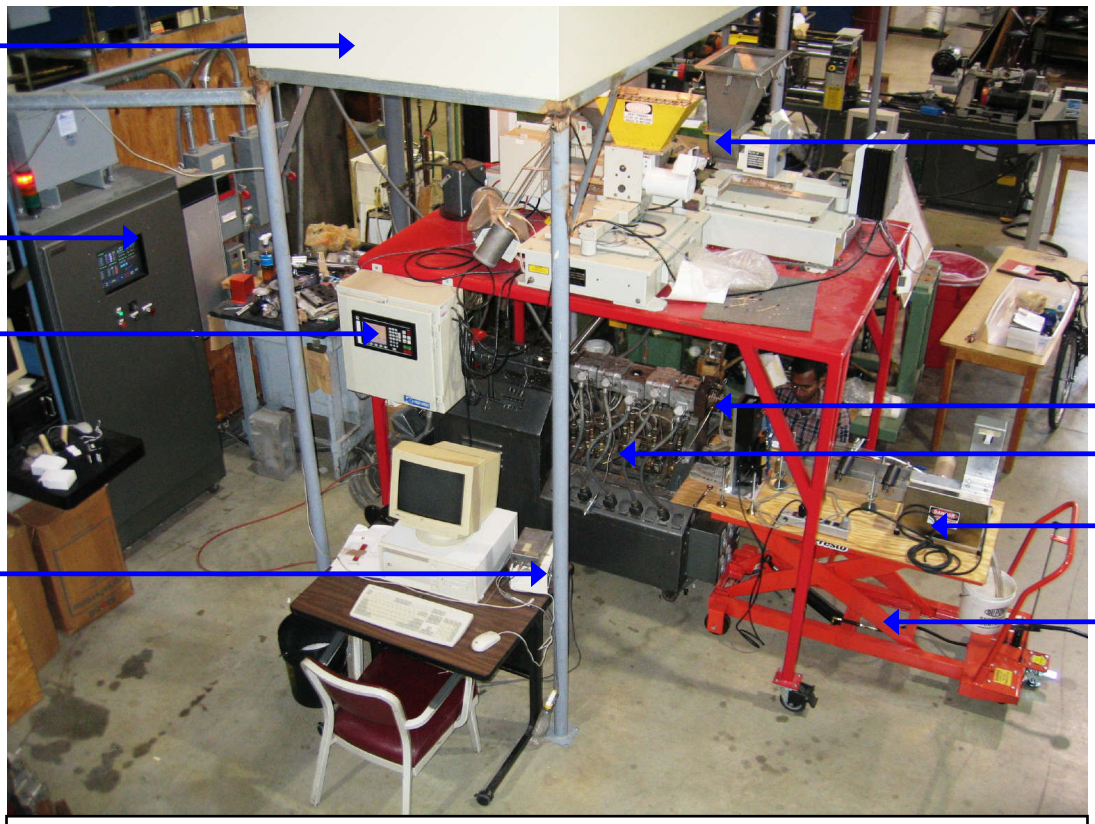

1 Extruder hood	4 Optical probe	7 Extruder
2 System control box	5 Feeder	8 Sample collecting
3 Feeder control box	6 Die	9 Adjustable height table

Figure 3.18 The twin screw extrusion facility overview

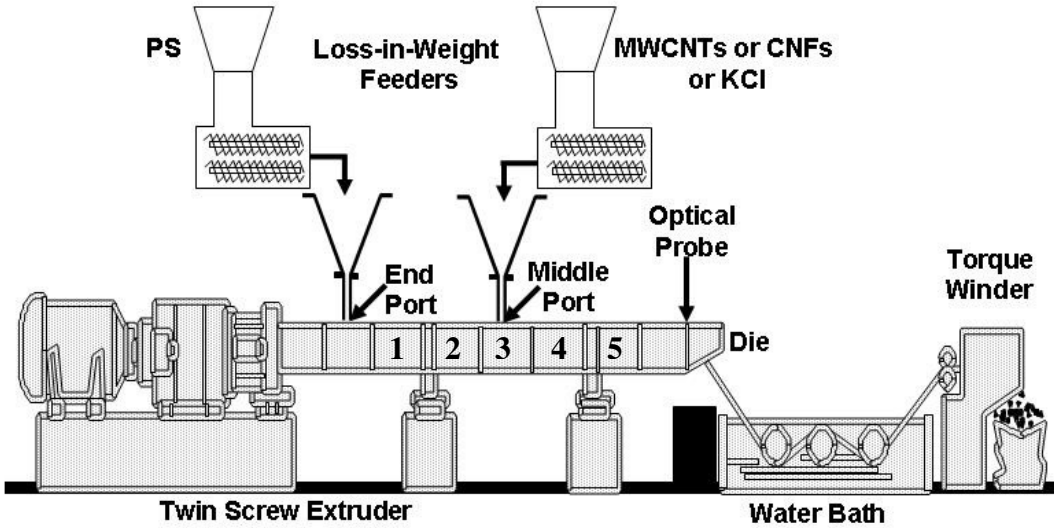

Figure 3.19 A schematic of the extrusion line with the loss-in-weight overhead feeders, optical probe and the automated extrudate collection system.

The extruder consisted of a main feed throat, called the 'end port', followed by five interchangeable sections, commonly referred to as the 'barrel zones' and the 'die zone' at the end to which the extrusion die was connected as shown in figures 3.19 and 3.20. The barrel zone 3 was called the 'middle port'. The middle port had an opening at the top that could be used either for feeding filler from the overhead feeders or devolatilization (i.e., removing the volatiles). When the middle port was used for devolatilization, the filler was fed along with the polymer through the end port. A Walsh R1402 vacuum pump was used to remove the air entrained with the nanoscale filler and other volatiles such as vapors from the extrudate. All the barrel zones were heated electrically and water-cooled such that five different temperature zones, one per barrel zone, were possible. The temperature can be controlled from ambient to ~300°C. The twin screws run through the barrel zone and the die zone.

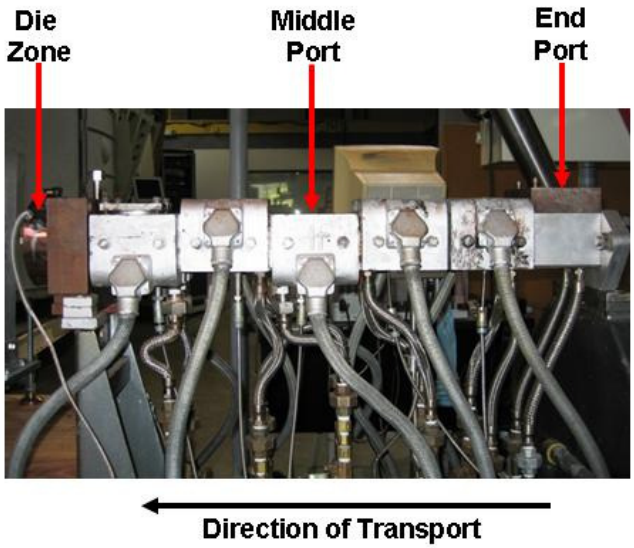

Figure 3.20 The interchangeable, electrically heated barrels showing the middle and end feed ports.

The die zone, which was at the end of the barrel zones, consisted of an eight-to-round adapter (see figure 3.21). This adapter houses the screw tips (i.e., end of the

screws) and directs the flow from the figure eight of the barrel to a round hole that comprises the die entrance. The adapter was designed to accommodate a wide variety of extrusion dies, the hardware that forms the final shape of the extruded product. The temperature of the adapter was controlled using a ceramic band heater figure 3.22.

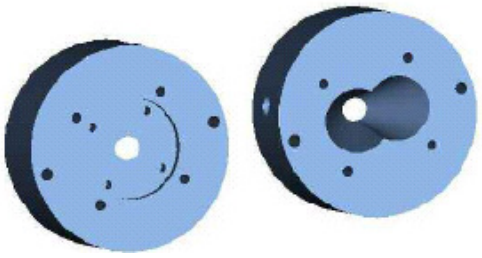

Figure 3.21 Eight-to-round adapter that guides the flow from the screws into the die.

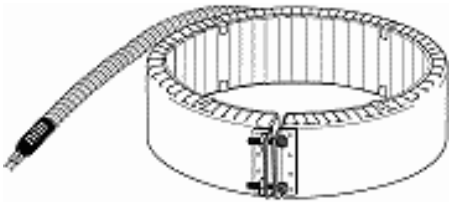

Figure 3.22 Ceramic band heater to control the temperature of the die zone.

The die was attached to the eight-to-round adapter. The slit die used in this work is 2.5 cm wide and 1 mm thick (see figure 3.23). The die is designed with a guillotine-edge arrangement that allows control over the thickness of the extrudate. This die was used to fabricate ribbon-like extrudate.

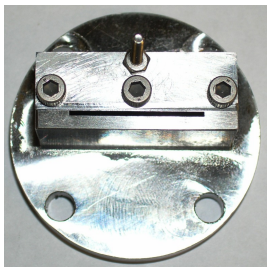

Figure 3.23 The slit die with guillotine-edge arrangement.

The twin screw extruder was controlled by a FACTS MI-101 control system (see figure 3.24). The FACTS MI-101 is a versatile data acquisition and control system specifically designed for extrusion line applications. The system has a broad range of capabilities including digital I/O and analog inputs, temperature and speed loop control, and PID loops that can be mixed and matched or cascaded together to provide complete extruder control. The system's configuration for different products may be stored as user defined product codes, allowing the user to change the entire system at the touch of a button to run a different product.

Figure 3.24 The FACTS control system was used mainly to control the temperature and the screw speed of the extruder.

The TSE facility contains three loss-in-weight feeders (see figure 3.25) to feed the polymer pellets or powder. The loss-in-weight control for solids allows strict feed rate control and verification of feeder stability. One is a pellet feeder and the other two are powder feeders. Only one of the two powder feeders was used at a time. All the feeders were a laboratory scale twin screw type; a type that exhibited better accuracy than the single screw or vibrating tray varieties. While one of the powder feeders could accurately

feed at high flow rates (>0.5 Kg/h), the other could accurately feed at lower flow rates (<0.25 Kg/h). The lower feed rates were especially suitable when using expensive fillers. A KCM control system was used to integrate and operate the feeders. The feeders rest on a mobile feeder platform that was designed to allow the feeders to be used with any of the extruders in the polymer processing laboratory. The feeders were connected to the feed port of the extruder with a finely polished stainless steel pipe.

Figure 3.25 The loss-in-weight over head feeders to feed powders and pellets.

During the course of the present work, the extrudate collection system was automated using a chill roll, water bath and a torque winder. Figure 3.26 shows a schematic of the automated extrudate collection system.

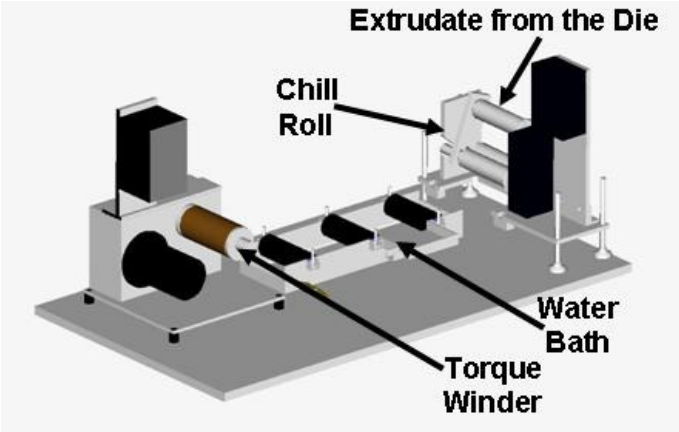

Figure 3.26 The automated extrudate collection system.

The chill roll (see figure 3.27) contains a top roller and two bottom rollers. The top roll and one of the bottom rollers are driven by a motor. The speed of the rollers is adjusted in accordance with the speed at which the extrudate comes out of the die. The rollers are cooled from inside with cooling water. It is also provided with sprinklers for additional cooling. The extrudate enters the chill roll upon exiting the die and is cooled. The extrudate passes over the top roller and between the bottom rollers before it is immersed in the water bath.

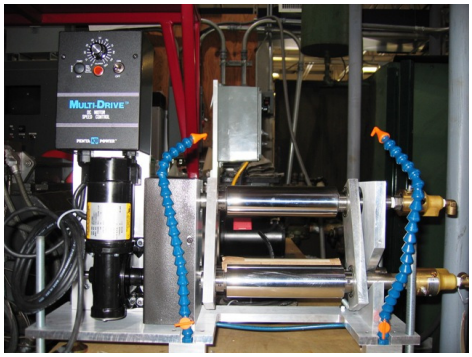

Figure 3.27 Chill roll

The water bath (see figure 3.28) consists of a steel trough with three rollers fixed to it. The trough, when filled with water, allows for the immersion and hence cooling of the extrudate. The extrudate upon exiting the bottom of the chill roll enters the water trough below the rollers and is conveyed further to the torque winder.

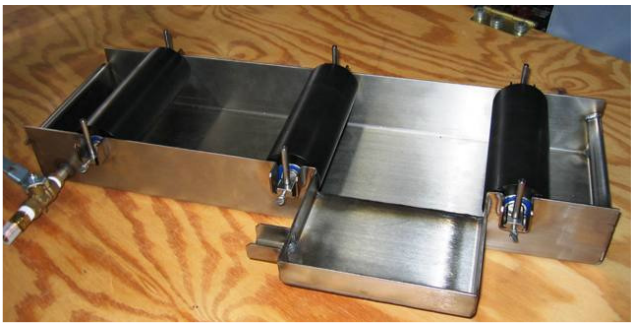

Figure 3.28 Water bath

The torque winder (see figure 3.29) contains a roller that is driven by a motor and used to wind up the extrudate into a roll. The torque on the torque winder can be adjusted and is set such that the extrudate is maintained under tension at all places. This ensures a smooth surface of the extrudate.

Figure 3.29 Torque winder

3.2.2.2 Screw Design

A twin screw extruder is mainly classified by the diameter of the screw and direction of rotation of one screw with respect to the other. In this work, co-rotating, intermeshing screws with a nominal diameter of 28 mm were used. The overall length to diameter ratio was greater than 26, which results in more options for screw element combinations to control the mixing and transport processes. Figure 3.30 shows the image of the screws.

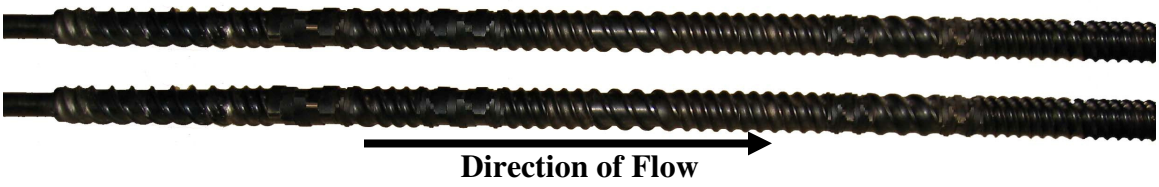

Figure 3.30 The twin screws when extracted out of the extruder.

The design of the screw plays a very important role in determining the degree of mixing achieved in the extruder. The geometry used for the screws is highly flexible in that individual element pairs of different shapes can be added together to result in specialized combinations for different material formulations. The screw designs used in this work contained three different zones – the melting zone, the conveying zone and the mixing zone. The conveying zone was in place to allow for the polymer relaxation, thereby, not decomposing the polymer chains at extremely high shear rates. Two different screw designs, one with a relatively low shear design (see figure 3.31) and another with a relatively high shear design (see figure 3.32) were used to investigate the influence of screw design on the structure-property relationships of the polymer nanocomposites.

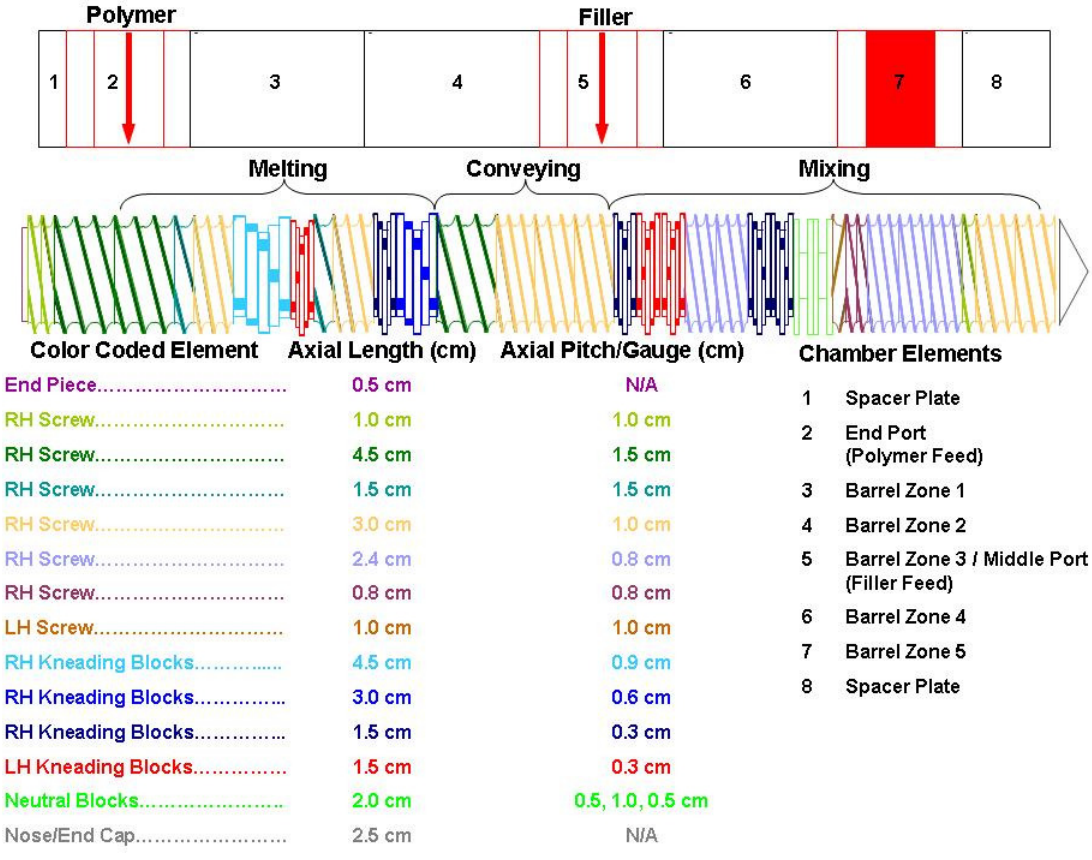

Figure 3.31 Low shear screw design

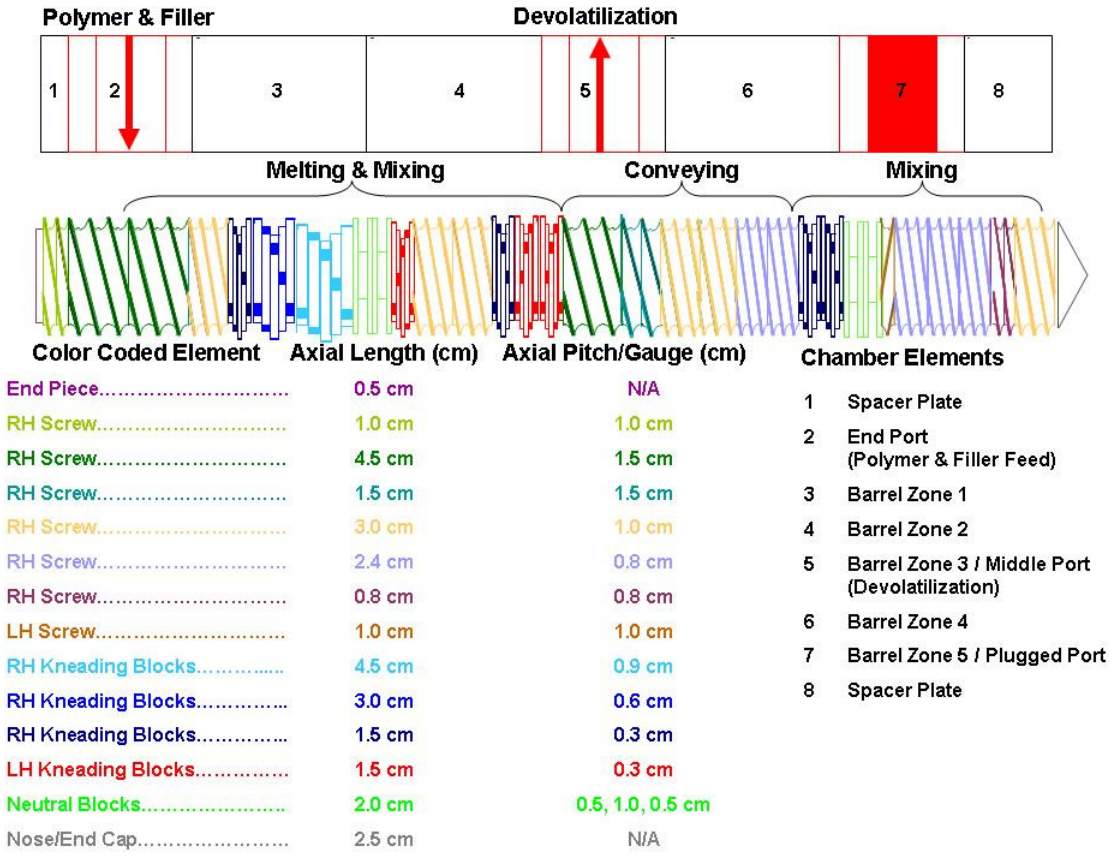

Figure 3.32 High shear screw design

The low shear screw design was configured such that the polymer could be fed through the end port and the filler could be fed through the middle port. In the low shear screw design, the polymer melted in the melting zone after entering the extruder the end port, got conveyed through the conveying zone, and subsequently the melt got mixed in the mixing zone with the filler that was introduced through the middle port. On the other hand, the high shear screw design was configured such that both the polymer and the filler could enter through the end port and a vacuum pump could be connected to the middle port for devolatilization. In the high shear screw design, the polymer and filler entered through the end port with simultaneous melting and solid mixing, followed by conveying in the conveying zone and eventually melt mixing in the mixing zone.

Compared to the low shear screw design, the residence time of the polymer and the filler, together, is longer in the high shear screw design. Furthermore, the number of shear elements such as kneading blocks and the reverse elements that occur during the polymer and filler transport is higher for the high shear screw design.

3.2.2.3 Procedure for Processing Polymer Nanocomposites

Processing the nanocomposites via TSE consists of melting the polymer, mixing the polymer melt with nanoscale filler in the twin screw extruder, extruding the nanocomposites through the die, and collecting the extrudate using the peripheral equipment. The following describes in the detail the various steps in the process.

Before the extruder is turned on, the feeder system has to be set up in the desired manner. The feeder system is calibrated to feed the desired material. The feeders are filled with the desired amounts of the polymer and the filler. The outlet of the feeder is connected to the desired feed port of the extruder and the aptness of the connection is ensured to avoid any polymer or filler spill. Following the feeder setup, the Facts Inc. control system, and the vent for exhaust gases are turned on. The barrel zones and the die zone are heated to the desired temperature. The temperatures of the barrel zones and the die zone depend on the polymer being used and is obtained from the manufacturer's specification of the recommended melt temperature for extrusion. For PS, the following temperature profile is used – barrel zone 1 at 375°F, barrel zone 2 at 425°F, barrel zone 3 at 425°F, barrel zone 4 at 425°F, barrel zone 5 at 425°F, and die zone at 325°F. The cooling water supply is turned on to ensure temperature control of the barrel zones. Furthermore, it is ensured that the feed zone does not get heated up too high to avoid

clogging the feed port due to softened polymer pellets. The desired screw speed is set and the extruder is turned on. The screw speeds used in this investigation ranged from 30 RPM to 200 RPM. Using the KCM feeder control unit, the desired feed rate of the polymer is set. The feed rates used in this work range from ~0.5 Kg/hr to ~2 Kg/hr. The screw speed and feed rate for a given polymer are set based on an insight into the degree of channel fill [81] and the maximum torque that can be achieved by the extruder motor for a given screw design. The pressure starts building up in the extruder as the screw channels gradually get filled up. Eventually, the extrudate comes out of the die (see figure 3.33).

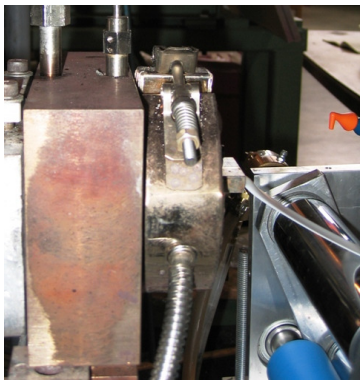

Figure 3.33 Extrudate exiting the slit die.

The initial extrudate may include the polymer and filler in the extruder from a previous run and must be purged. After the polymer melt attains a steady flow, the nanoscale fillers were added at the desired flow rate through the desired feed port, i.e., end port of middle port an impulse or step input. The experiments with impulse input of the CNFs were conducted to obtain the residence distributions as described in 3.3.2. The experiments with step input of the CNFs were conducted to establish the processing-microstructure and structure-property relationships as described in 4.1 and 4.2.2. Experiments with step input of CNFs and KCl were also conducted to demonstrate the

combinatorial approach as described in 4.4. In the step input experiments, the flow rate of the filler is chosen to produce the desired loading of filler in the composite.

The extrudate from TSE is collected using the peripheral equipment – chill roll, water bath and torque winder. The cooling water system is turned on and the extrudate is fed to the chill roll followed by the water bath and the torque winder. The speed of the chill roll and the speed of the rollers of the torque winder are controlled until the extrudate is steadily collected, as a roll, with uniform cross-section. Figure 3.34 shows a snap shot from steady collection of extrudate. Notice the PS roll wound up on the roller of the torque winder. The thickness of the extrudate could be tuned by varying the speed of the chill roll.

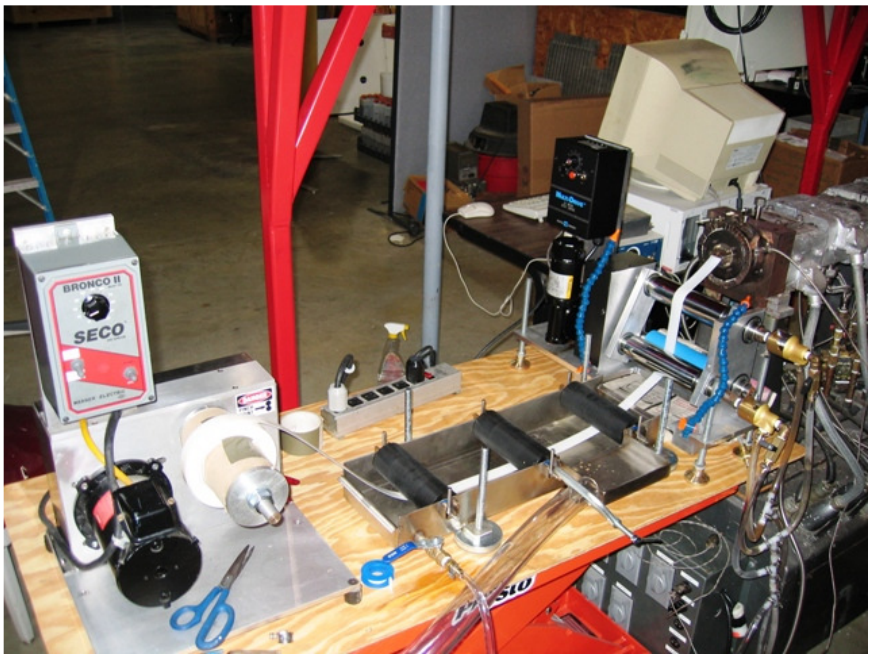

Figure 3.34 Automated collection of extrudate samples

Experiments with step input of filler were conducted with and without a vacuum pump connected to the middle port for devolatilization. This resulted in composites with varying porosity, as described in 4.1.6, that were studied to determine the influence of

porosity on material properties. Furthermore, as mentioned in 3.2.2.2, step input experiments were also conducted with high shear and low shear screw designs to investigate the influence of screw design on the structure-property relationships of the polymer nanocomposites.

3.2.3 Annealing the extruded PS-CNF composites

The extruded PS-CNF composites at various CNF loadings were further annealed to investigate the influence of annealing on their microstructure, electrical and rheological properties. The composites were placed on a steel plate and heated to a temperature well above the softening point of PS (90°C), up to the recommended melt temperature (~210°C) in an inert atmosphere. In essence, it was ensured that there was no imposed stress on the PS-CNF composite, such as that imposed during the shear flow through the die. This led to relaxation of the percolated network of CNFs as described in 4.1.4 and improvement in electrical properties as described in 4.2.2.2.

3.3 Characterization of Structure & Microstructure

3.3.1 Thermogravimetric Analysis: Composition

Composition of the filler in the composites is the important structural parameter that has to be determined not only to establish the structure-property relationships, but also as a quality check for the processing related material losses. Determining the KCl loading in the PS-KCl composites was relatively easier because the thermal decomposition temperatures of PS and KCl are significantly different. Hence, it was easy to combust PS completely without affecting the KCl. Knowing the initial weight (w_o) of

the PS-KCl composite and the final weight (w_f) after the combustion of PS, the KCl loading can determined as,

$$Wt.\%\ KCl = 100 \times \frac{w_f}{w_o} \tag{3.1}$$

However, it is more complicated for the PS-MWCNT and PS-CNF composites because the combustion of CNFs and MWCNTs starts before the complete combustion of PS. Thus a more sophisticated technique like thermogravimetric analysis (TGA), with controllable temperature ramp and continuous weight monitoring, is required to determine the loading of MWCNTs and CNFs in the composites.

In this work, a Cahn TG 2131 TGA was used to determine the loading of MWCNTs and CNFs in the composites. In all the TGA tests conducted, the initial weight of the composite sample was consistently maintained to be ~100 mg. The weight fluctuations experienced by the empty sample holder were subtracted from the raw TGA data before analyzing the weight loss of the sample. Figure 3.35 shows the thermogravimetric response of the neat ingredients i.e., neat PS, neat MWCNTs and neat CNFs, in the temperature range of 25-1000^{o}C at a temperature ramp of 10^{o}C/minute in an air atmosphere. It is evident that the PS shows two distinctly different weight losses and decomposes completely by 550^{o}C. While the former weight loss corresponds to the styrene-rich phase, the latter corresponds to the butadiene-rich phase. The two-stage combustion of PS in an air atmosphere is in agreement with an earlier work by Castaldi et al [82]. The neat MWCNTs start to decompose around 750^{o}C. The neat CNFs start to decompose around 600^{o}C and are nearly completely consumed by 1000^{o}C.

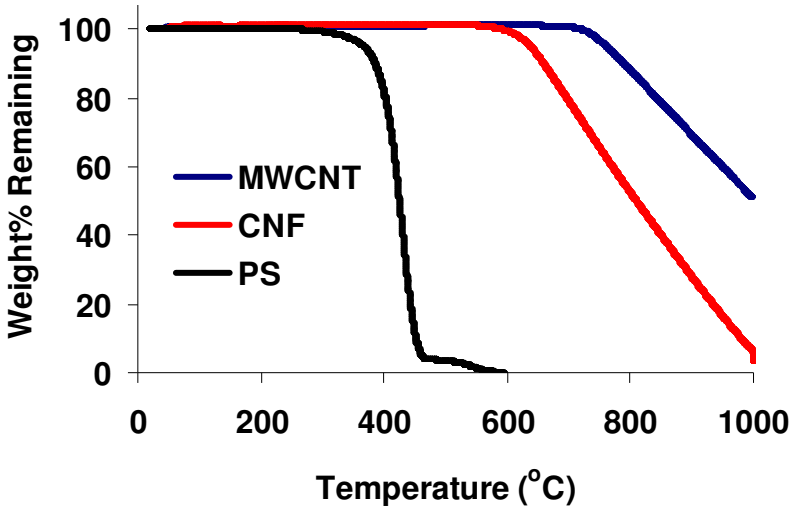

Figure 3.35 The weight loss curves of the neat PS, neat MWCNTs and the neat CNFs.

Consequently, the TGA of the PS-MWCNT and PS-CNF composites was conducted in an air atmosphere using the following temperature profile – hold isothermal at room temperature for 10 minutes, ramp at 10°C/minute up to 600°C and hold isothermal for 30 minutes at 600°C. Figure 3.36 shows the representative weight percent and weight loss rate (WLR) profiles obtained when the PS-CNF composites were studied using the TGA procedure described above. The two distinct weight losses corresponding to PS and the third weight loss corresponding to the CNFs are evident. The three corresponding peaks in WLR are also distinct. The behavior of PS-MWCNT composites was very similar to the PS-CNF composites except the higher decomposition temperature of MWCNTs. The loading of the MWCNTs or CNFs in the composite was determined from the weight percent remaining at the time corresponding to the point of inflection between the second and third peaks of the WLR curve (i.e., when the second derivative of weight percent is zero). This is a rigorous and consistent technique to characterize the materials of unknown composition produced via combinatorial approaches [31].

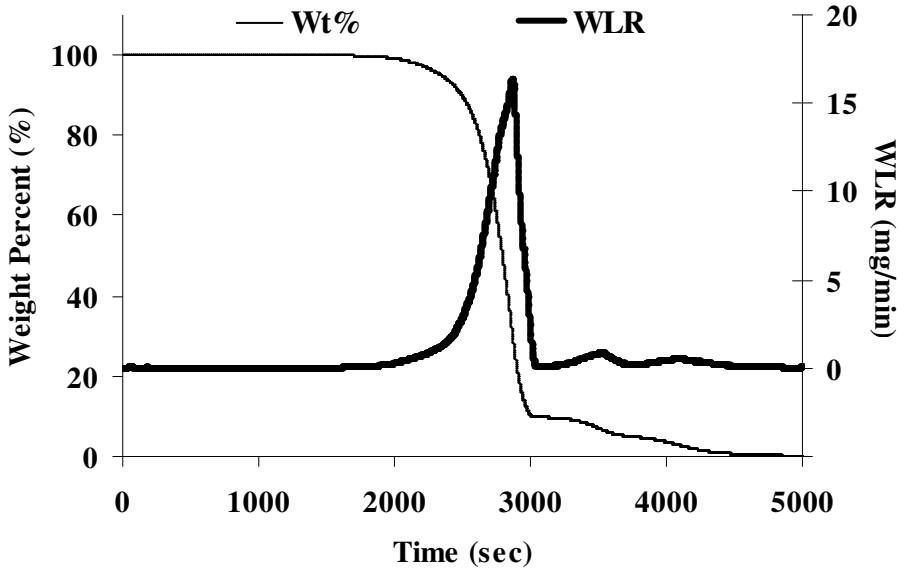

(a)

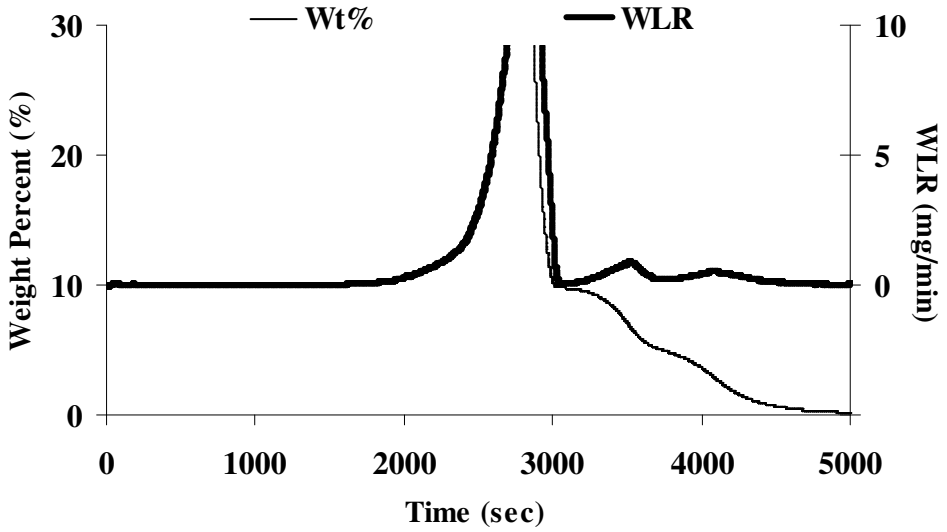

(b)

Figure 3.36 (a) Representative weight% and WLR profiles for PS- CNF composites. **(b)** Zoomed in view more clearly indicating the presence of a third peak. The weight percent remaining at the inflection point between the second and third peaks represents the loading of the filler in the composite.

Although TGA is a precise and accurate technique to determine the loading of the filler in the composite, it is also a time consuming and destructive. Hence, it is less suitable for determining the compositional gradients of polymer nanocomposites.

3.3.2 In-Situ Absorbance Measurement: Residence Distributions

As described in 2.5.2, residence distributions are a convenient measure of the average mixing occurring in extrusion due to channeling, back-mixing and stagnation. In this work, a Cuda I-150 optical probe was used to obtain the residence time distribution of the extrusion process. The optical probe was mounted in the die zone as shown in figure 3.37.

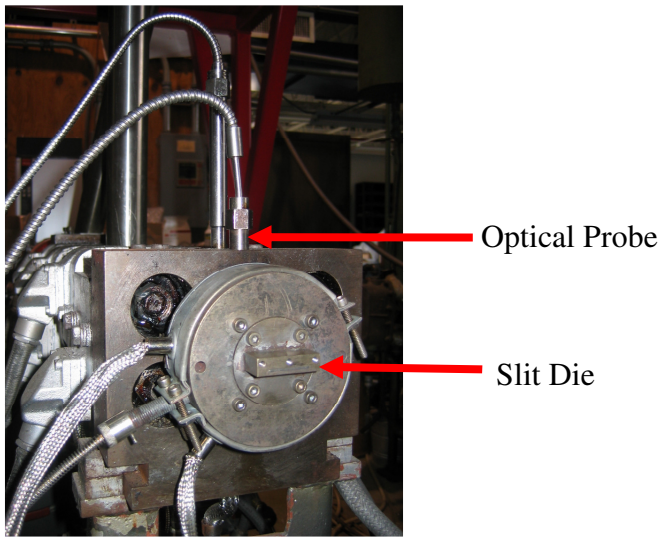

Figure 3.37 The die zone with the optical probe mounted.

While the PS melt is white, the MWCNTs/CNFs are black in appearance. An impulse input of the filler material would result in a gradual change in the color and hence the absorbance of the melt. The optical probe tracked the changes in absorbance of the melt, thereby tracking the amount of material flowing past a stationary point. The maximum output signal of the optical probe had a voltage of 1V DC. The intensity of the optical

probe was adjusted to produce an output signal between 0.44V DC and 0.46V DC when neat PS melt passes beneath the probe during the extrusion process. The curve obtained by tracking the change in the optical absorbance of the melt as a function of time after an impulse input of the filler material is the residence time distribution (RTD). The optical probe data was acquired by an automated data acquisition system at a frequency of 10 Hz and filtered using a low-pass butterworth filter to avoid any noise from electrical interference. By trial and error, the best filtering parameters were obtained to be a cutoff frequency of 0.02 Hz, filter order of 1 and no decimation (i.e., decimation factor of 1). Furthermore, in order to compare the RTDs resulting from different processing conditions, they were normalized (i.e., the area under the RTD curve was set to unity) as given by equation (2.2). Figure 3.38 shows a normalized RTD resulting from the TSE process. The impulse input of the filler is followed by a brief delay time (t_D) following which there is a sharp increase in the absorbance of the melt. The end time (t_E) marks the flow of the entire input amount of the filler past the optical probe. For any given time interval (t_0), the area under the curve represents the amount of material with that flowed past the optical probe. The mean residence time is defined as the time at which half of the total amount of material flowed past optical probe. The mean residence times of the filler in the extruder when fed through the middle port and the end port were found to be ~5 minutes and ~15 minutes respectively. Furthermore, the normalized RTDs can be converted to normalized residence volume distributions (RVDs) as given by equations (2.3) and (2.4). The normalized RVDs thus obtained were modeled as a series of perfect batch mixers, and convoluted with a step input to predict the compositional gradient as described 4.4.1. Since this technique is rapid and non-destructive when compared to the

TGA, it is suitable for combinatorial approaches to fabricate and characterize polymer nanocomposites.

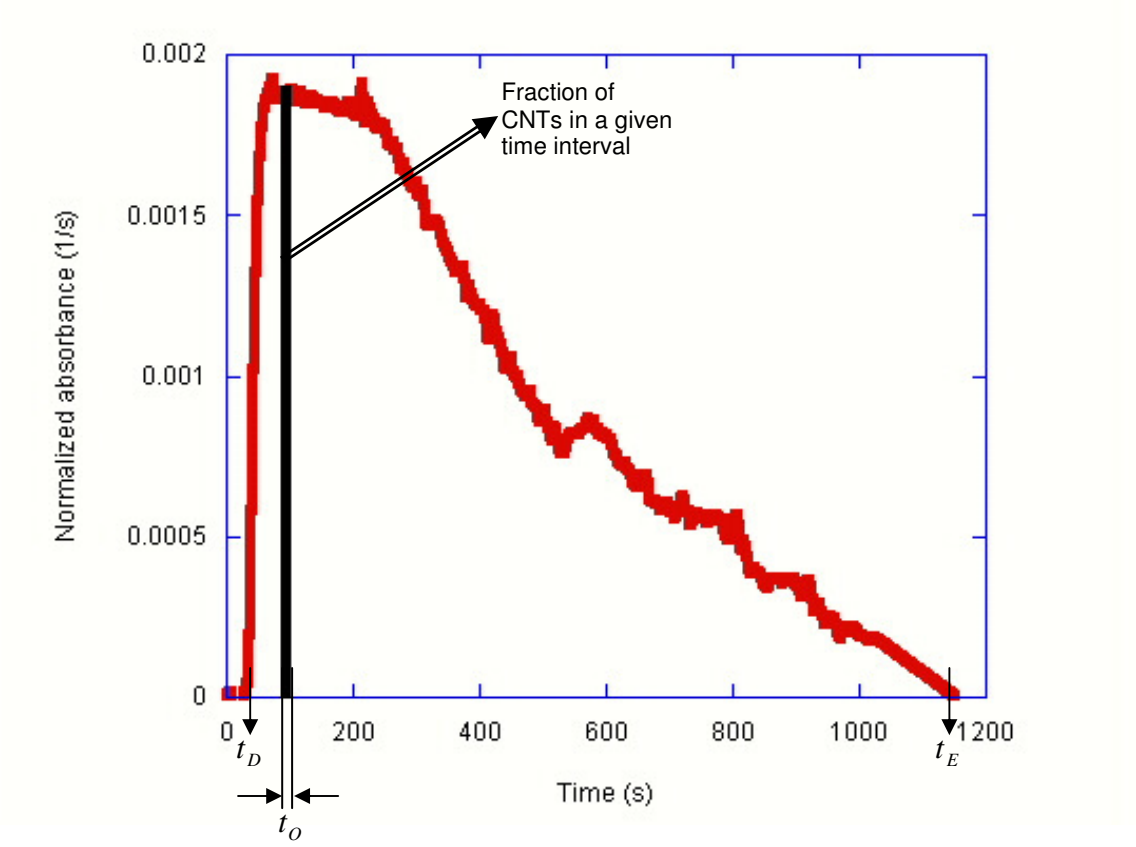

Figure 3.38 Representative normalized Residence Time Distribution (RTD).

3.3.3 Distribution, Dispersion, Aspect Ratio and Alignment: Microscopy

To characterize the microstructural features, several microscopy techniques, optical microscopy, confocal microscopy, scanning electron microscopy (SEM), and transmission electron microscopy (TEM), were employed. Each technique is beneficial in characterizing a particular microstructural feature. The following is a list of microstructural features of interest and the associated microscopy techniques used in this research to study them:

1. Distribution of Agglomerates (*optical*)

2. Dispersion of MWCNTs/CNFs (*SEM*)
3. Aspect ratio CNFs (*TEM*)
4. Alignment of CNFs (*confocal*)

The macroscopic distribution of agglomerates of CNFs and MWCNTs and the porosity in the composites was characterized using a Leica optical microscope. Since the as-prepared surface of the extruded composites did not exhibit any features (see 4.1.2), it had to be polished with 800 grit and 1200 grit size SiC polishing papers followed by 3 μm, 1 μm and 100 nm diamond suspensions to expose the porosity and the agglomerates.

The dispersion of MWCNTs or CNFs and the morphology of the PS-MWCNT and PS-CNF composites were examined using a Quanta FEG 200 scanning electron microscope (SEM). The surface and the cross-section of the nanocomposites were imaged as-prepared and after polishing. While imaging composites with low MWCNT loadings under the SEM, it was observed that using a low energy electron beam (~5 kV) circumvented the charge accumulation on the surface. However, the composites with low CNF loadings had to be coated with gold in order to avoid the charge accumulation.

In order to characterize the aspect ratio of the CNFs in the composites processed via solvent processing or extrusion, the CNFs were separated from the PS matrix by refluxing the PS-CNF composites with THF in the absence of shear (stirring, sonication etc.), followed by further dilution. A drop of the dilute CNF suspension was mounted on a grit and characterized using the Jeol TEM to measure the aspect ratio of the CNFs.

The alignment of the CNFs in the composites was evaluated using a laser confocal microscope (Carl Zeiss Model LSM510). The confocal microscope utilizes coherent laser light and collects reflected light exclusively from a single plane with a

thickness of 100 nm (a pinhole sits conjugated to the focal plane and rejects light out of the focal plane). A red laser (λ = 633 nm) was used as the coherent light and images were taken with an Epiplan-Neofluar 100x/1.30 oil-pool objective. A filter (Rapp Optoelectronic LP385) was used to limit the lower spectra of reflected light. One hundred two-dimensional images (optical slices with 512 pixels x 512 pixels), with scan size 92.1 x 92.1 μm, were taken at a spacing of 100 nm by moving the focal plane. Images were further analyzed using the NIH Image software program.

3.4 Characterization of Properties

3.4.1 Electrical Conductivity

The electrical conductivity of the composites was measured in accordance with ASTM D4496. Samples of a known cross-sectional area and thickness were placed between copper electrodes and the DC resistance was measured using an Agilent 34401A precision digital multimeter. The surfaces of the sample in contact with the electrodes were coated with silver paint in order to reduce discrepancies arising from micro-roughness. It was ensured that the surface area of the electrodes exceeded the cross-sectional area of the discs.

3.4.2 Rheological Properties

Dynamic rheological measurements were performed on a Rheometrics RDAIII rheometer (see figure 3.39 below) using 2.5 cm parallel plates. Sample discs of 2.5 cm diameter were placed between the plates with due care given to the sensitive transducer of the instrument. The oven was then heated to the desired temperature under a nitrogen

atmosphere to avoid degradation of PS. The melt rheology was conducted at temperatures of 170, 180, 190, 200 and 210ºC with a gap of about 1 mm between the plates. After attaining the desired temperature, the plates were further pushed together by approximately 0.1 mm to ensure that the sample completely fills the volume between the plates. Any additional material overhanging the plates was trimmed using a metal spatula. The storage modulus, loss modulus and complex viscosity were measured as functions of frequency (0.01 – 100 rad/s) within the linear viscoelastic regime (less than 0.5% strain) of the sample. Before recording each frequency sweep, the sample was equilibrated at the test temperature usually for a period of 30 min. Three different samples were tested at each loading of the filler.

Figure 3.39 The RDA III parallel plate rheometer.

3.4.3 Thermo-oxidative behavior

In addition to determining the loading of the filler, the thermo-oxidative behavior of the composites was also studied using the TGA. In specific the temperature at and magnitude of the peak weight loss rate corresponding to the styrene rich phase and the weight loss of the filler were studied as function of the type of process and the extrusion processing parameters.

3.4.4 Mechanical Properties

For the mechanical tests, samples were prepared according to the ASTM D-638 'Standard Test Method for Tensile Properties of Plastics' (see figure 3.40) and the prescribed test procedure was followed. A Tinius Olsen load frame with a 25 KN load cell was used. The sample was loaded as close to parallel as possible to crosshead motion to reduce shear stress. The grips were approximately 100 mm apart to provide a suitable gage length for strain measurement. Samples were preloaded to approximately 4 lb_f to reduce the error in strain measurement. The tests were conducted at 5 mm/min. After the test was complete, the data was saved and then reduced using the gauge length and the cross-sectional area of the sample to obtain stress-strain curves.

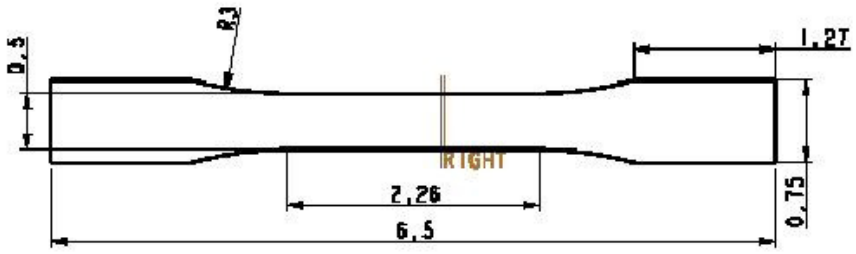

Figure 3.40 The sample used for mechanical testing.

4. Results and Discussion

4.1 Processing – Microstructure Relationships

The microstructure of solvent processed PS-MWCNT, solvent processed PS-CNF and extruded PS-CNF composites was studied using one or more of optical, confocal, scanning and transmission electron microscopy and compared when applicable.

4.1.1 Microstructure of Solvent Processed PS – MWCNT Composites

The as-received agglomerates of MWCNTs (see figure 3.2) were sonicated and mixed with the PS using the solvent processing technique described in 3.2.1. An SEM image of the surface of the solvent processed PS-MWCNT composite with 5 wt.% MWCNT loading is shown in figure 4.1. The surface revealed a random, isotropic dispersion with two distinctly different kinds of MWCNTs – non-interacting MWCNTs that are reinforcing the polymer matrix and percolated MWCNTs that form a scaffold-like structure. It was also observed that the diameter of the processed MWCNTs ranged from 30-50 nm and the length ranged from 2-5 μm thereby indicating no evidence of tube breakage. The loading of MWCNTs is qualitatively consistent with the volume fraction calculations (see 4.2.1.1). Furthermore, the significant increase in electrical (see 4.2.1.1) and rheological (see 4.2.1.2) properties is due to the scaffold-like characteristics of the continuous phase of percolated MWCNTs.

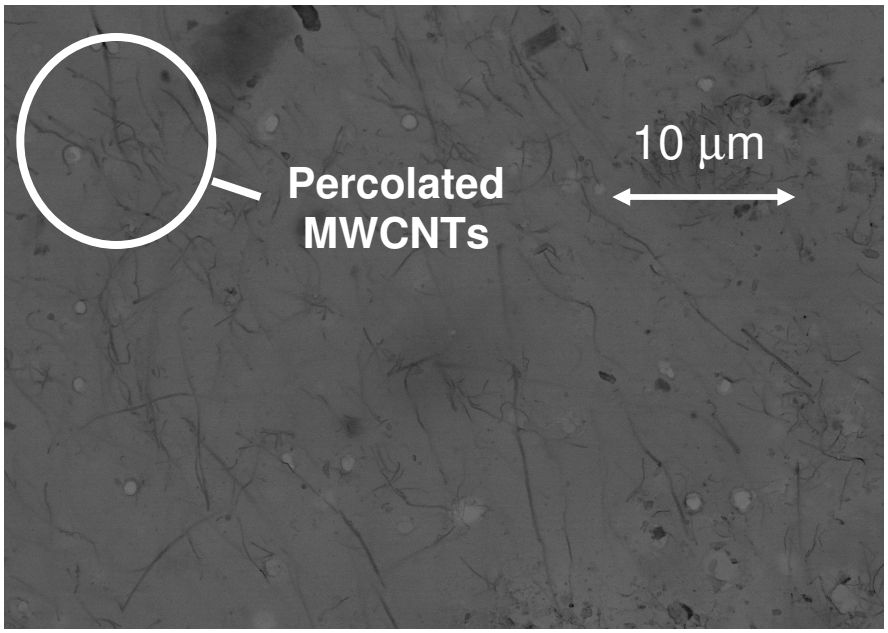

Figure 4.1 Random, isotropic dispersion of MWCNTs at a 5wt.% loading. Note the continuous phase of percolated MWCNTs with a scaffold like structure.

The microstructure of the PS-MWCNT composites with 5 wt.% loading prepared using two different solvents, DMF and THF, was also compared. SEM images of a macroscopic crack initiated by shearing the composite are shown in figure 4.2.

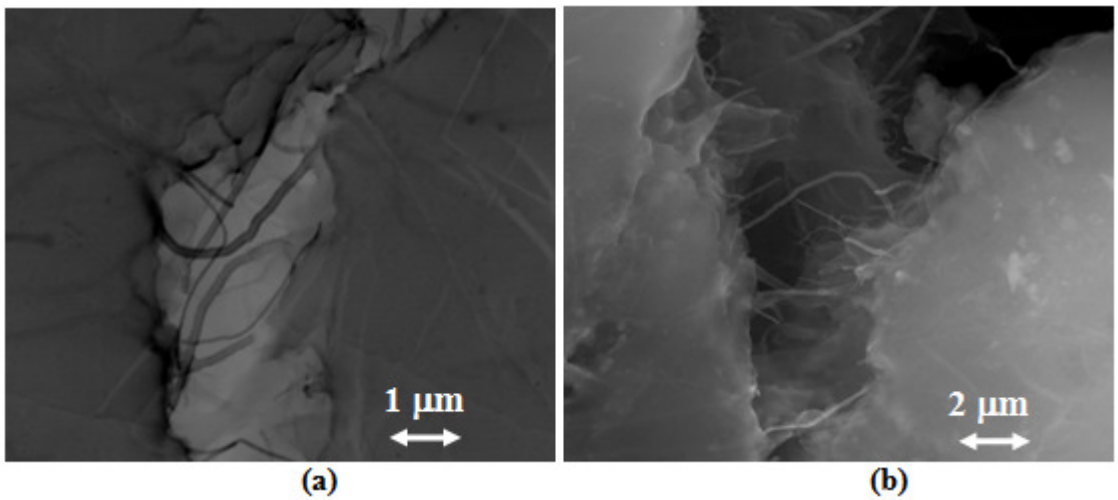

Figure 4.2 A macroscopic crack in the PS-MWCNT composites processed using **(a)** DMF and **(b)** THF reveals pull out of MWCNTs indicating poor adhesion between MWCNTs and PS.

Both images show that the MWCNTs are pulled out as the crack propagates, thereby providing some potential insight into the interfacial adhesion between the MWCNTs and the PS. These results indicate that there is a low level of interfacial adhesion associated with the use of solvents, which could have a deleterious effect on the macroscopic mechanical behavior.

4.1.2 Microstructure of PS – CNF Composites: Solvent Processed & Extruded

In order to understand the effect of the mixing mechanism on the dispersion of CNFs, the microstructure of the solvent processed PS-CNF composites was studied and compared with the extruded ones. Figure 4.3 shows the SEM images of the surface of the solvent processed and extruded PS-CNF composites with 5 wt.% CNF loading.

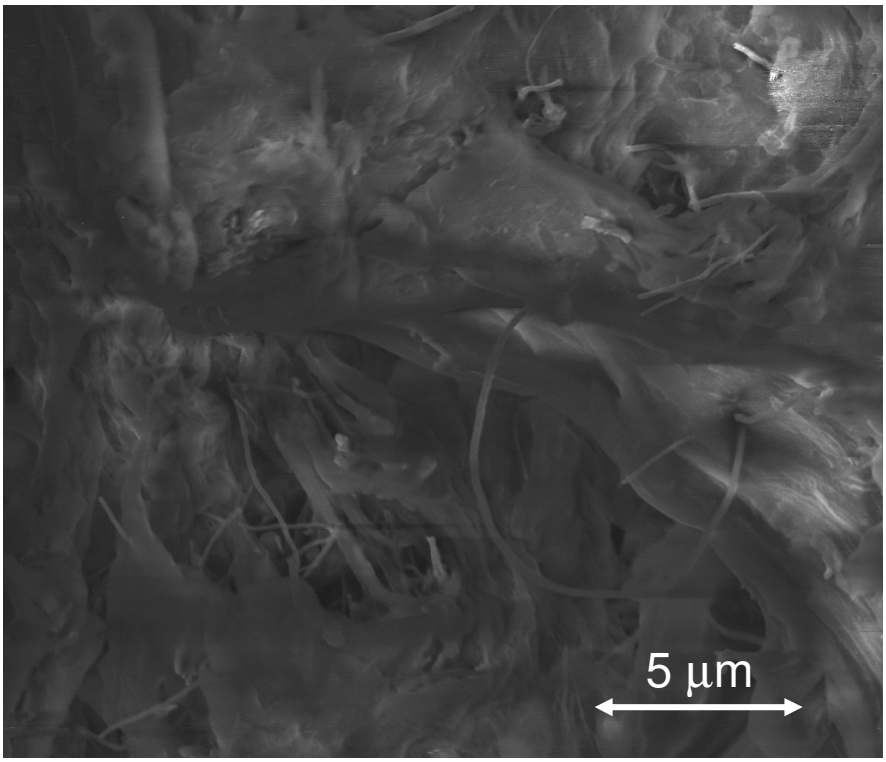

(a)

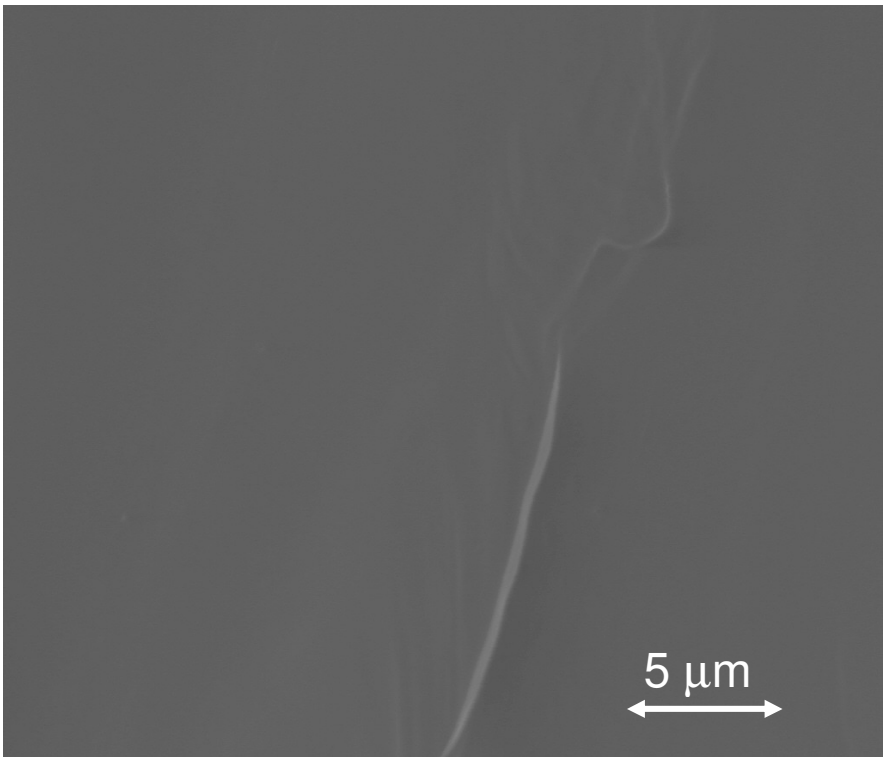

(b)

Figure 4.3 Surface of the **(a)** solvent processed and **(b)** extruded PS-CNF composites. While CNFs are present on the surface of the solvent processed composites, they tend to stay below the surface for the extruded composites.

It is evident from the figures that the CNFs are present on the surface of the solvent processed composites, but depleted on the surface of the extruded composites. The depletion of CNFs at the surface was consistently observed in spite of varying operating conditions in the extrusion process. Such filler phase segregation at the surface of the extruded composites was observed in earlier works too [24]. It can be attributed to the alignment of the CNFs imposed by the shear flow in the die. Since the shear rate (or velocity gradient) is maximum at the die wall, which is in contact with the surface of the extrudate, the likelihood of alignment of CNFs is more at the surface of the extrudate. To align in the direction of the flow, the CNFs rotate around their center of mass, thereby staying below the surface.

Since the surface of the extruded composites did not offer sufficient information about the dispersion of CNFs, the cross-section was studied and compared with that of the solvent processed composites. Figure 4.4 shows the SEM images of the cross-section of the solvent processed and extruded PS-CNF composites with 5 wt.% CNF loading. It is evident from the figures that the solvent processed composites show a random dispersion of CNFs and the extruded composites show agglomerates of CNFs with an average size of 50 μm. The dispersion of CNFs in the solvent processed PS-CNF composites is similar to the dispersion of MWCNTs in the solvent processed PS-MWCNT composites.

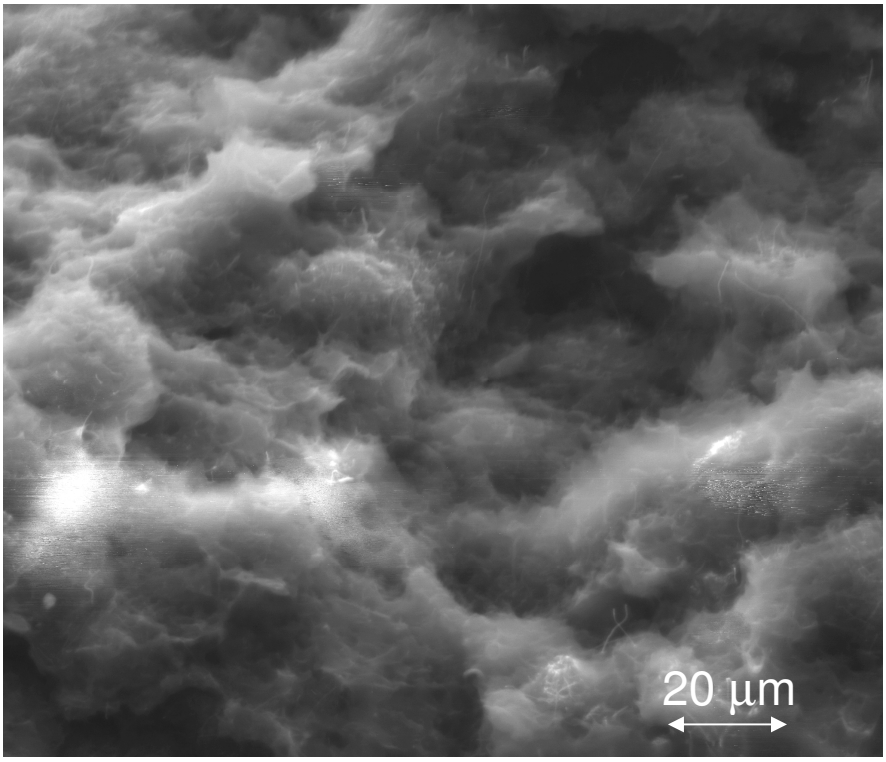

(a)

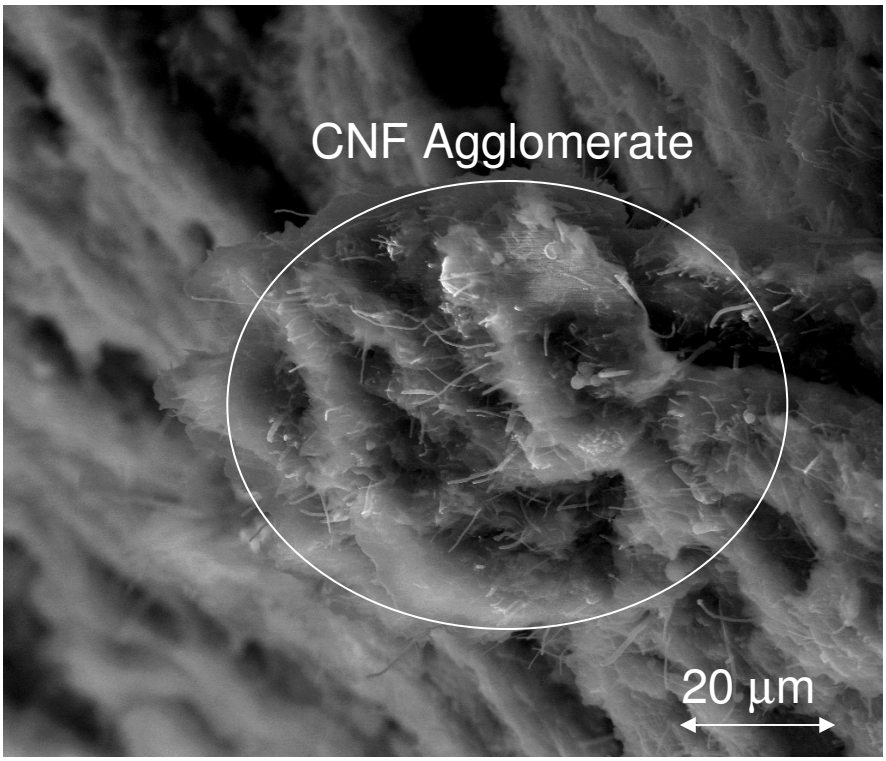

(b)

Figure 4.4 Cross-section of the **(a)** solvent processed and **(b)** extruded PS-CNF composites. While CNFs are randomly dispersed in the solvent processed composites, agglomerates are present in the extruded composites.

4.1.3 Aspect Ratio of CNFs: Solvent Processed & Extruded

The aspect ratio of CNFs in the solvent processed and extruded PS-CNF composites was measured as described in 3.3.3 to determine the effect of processing on the mechanical degradation of the filler. Figure 4.5 shows a representative TEM image each of the CNFs separated from the solvent processed and the extruded PS-CNF composites. It was found from 120 such measurements that the average aspect ratio of the solvent processed CNFs was 35:1 and that of the extruded CNFs was 25:1. The lower aspect ratio of the extruded CNFs indicates that the magnitude of shear rate in extrusion (attrition) is higher than that in solvent processing (sonication).

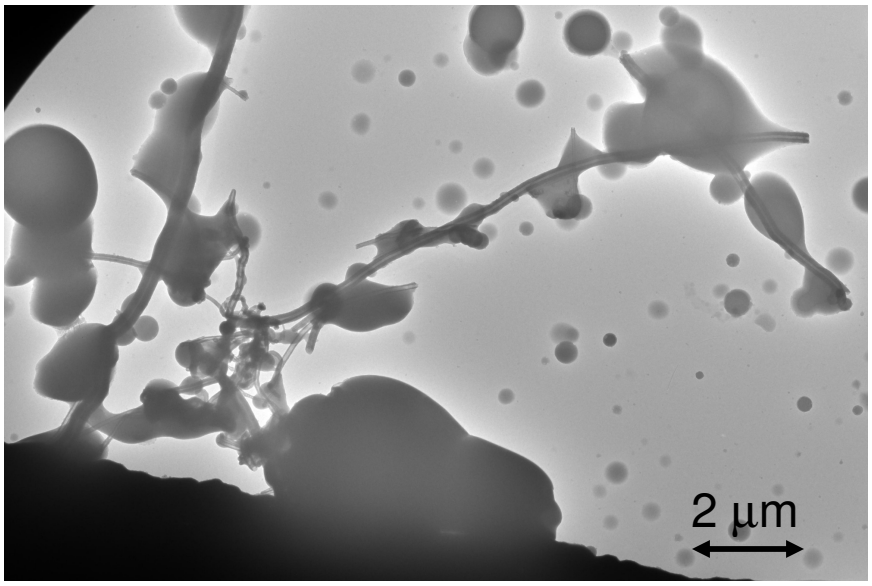

(a)

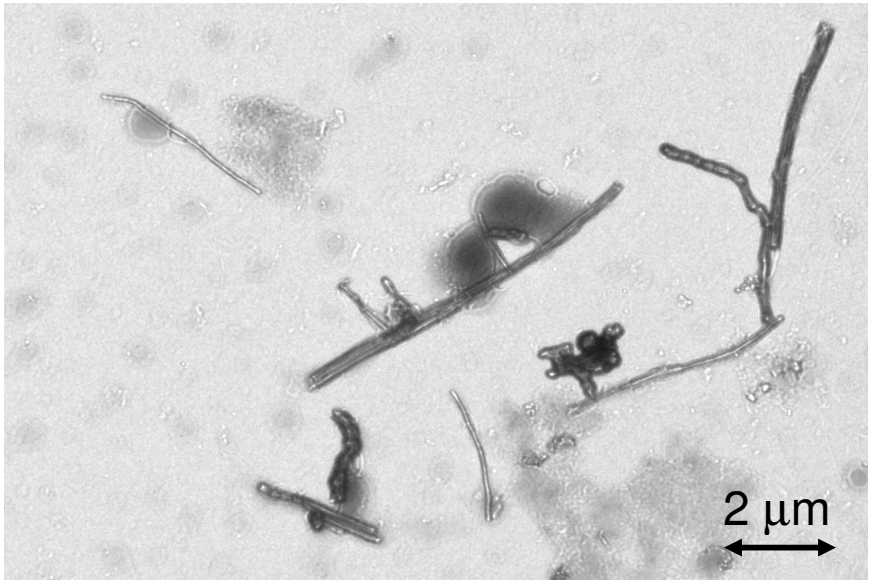

(b)

Figure 4.5 Representative TEM images of **(a)** solvent processed and **(b)** extruded CNFs. Note the higher aspect ratio of the solvent processed CNFs (35:1) when compared to that of the extruded CNFs (25:1).

However, as discussed in 4.1.2, the extruded composites exhibit agglomerates of CNFs, while the solvent processed ones exhibit random dispersion of CNFs. This can be attributed to the lower residence time in extrusion (5-10 minute) when compared to that in solvent processing (2-4 hour). An important conclusion can be drawn from these

observations: *deagglomeration is a critical combination of both the magnitude of shear and the residence time*.

4.1.4 Alignment of CNFs: Extruded & Annealed PS-CNF Composites

As will be discussed in 4.2.2.1, the electrical properties of the solvent processed PS-CNF composites were better than those of extruded ones. Furthermore, annealing the extruded composites as described in 3.2.3 improved the electrical properties, as will be discussed in 4.2.2.2. In order to understand the microstructural changes associated with the improvement in electrical properties, the extruded and annealed PS-CNF composites were characterized using confocal microscopy. Confocal microscopy was chosen over SEM or TEM in order to obtain the configuration of CNFs at various depths below the surface, without disturbing the surface. Representative images of the unannealed and annealed PS-CNF composites with 10 wt.% CNF loading can be seen in figure 4.6.

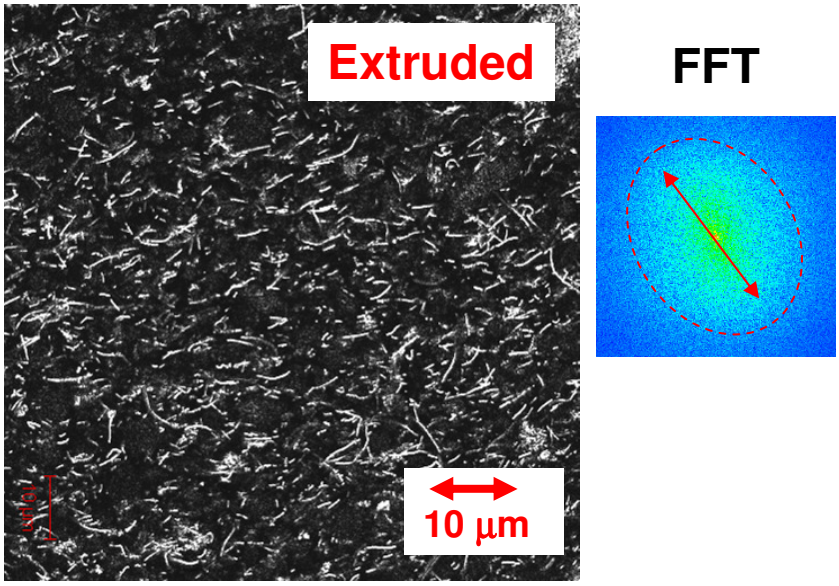

(a)

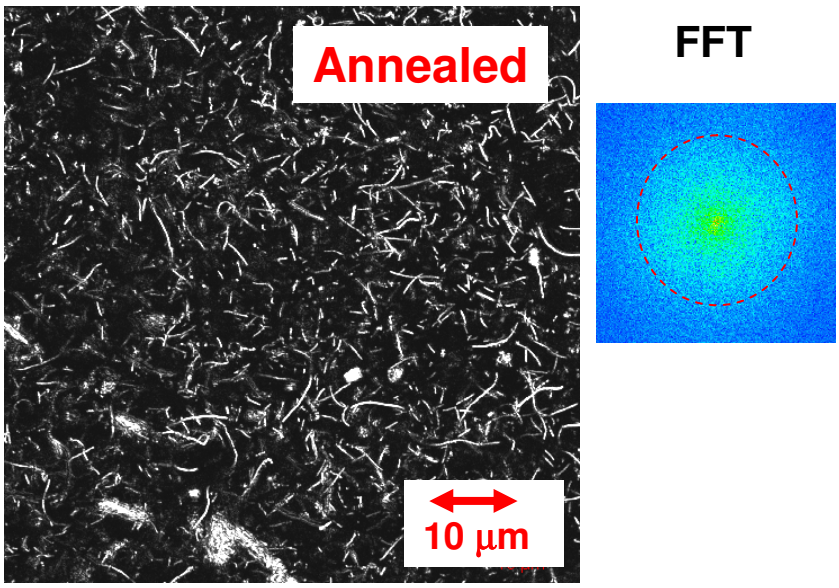

(b)

Figure 4.6 Microstructure of the **(a)** extruded and **(b)** annealed PS-CNF composites. While the extruded composites show a preferential alignment of CNFs, the annealed composites show a relatively random distribution.

The image of the unannealed composite tends to indicate a preferential alignment of the CNFs. In order to better assess the level of alignment, the Fourier transform of the image was obtained. An anisotropic pattern was obtained that is elongated normal to the apparent alignment direction in the image. Thus, it is clearly evident that the CNFs are preferentially aligned, presumably due to the shear flow through the die. In contrast, the image of the annealed composite exhibits a relatively random distribution of the CNFs, and the corresponding Fourier transform has a more isotropic pattern An important conclusion about the processing-microstructure relationships can be drawn from these observations: confocal microscopy indicates that *annealing restores a random distribution of CNFs, which implies the re-establishment of interconnectivity of CNFs* that is necessary for the improvement in electrical properties.

4.1.5 Microstructure of Extruded PS – CNF Composites: Influence of Screw Speed

In order to investigate the influence of screw speed on the size and distribution of the CNF agglomerates, the extruded PS-CNF composites were polished and characterized with the SEM. Figures 4.7a and 4.7b show the surface of the extruded PS-CNF composites, processed at the minimum (30 RPM) and the maximum (200 RPM) screw speed respectively, with agglomerates of CNFs that were exposed by polishing. It is evident from the images that the agglomerates in the composites processed at 30 RPM are relatively bigger than those processed at 200 RPM. While the composites processed at 30 RPM show an average agglomerate size of ~100 μm with an aspect ratio of 2:1, the composites processed at 200 RPM show an average agglomerate size of ~30 μm with an aspect ratio of 1:1. An important conclusion about the processing-microstructure relationships can be drawn from these observations: *increasing screw speed, which corresponds to increased shear rate, reduces the aspect ratio and size of the agglomerates, but does not disperse them into individual CNFs*.

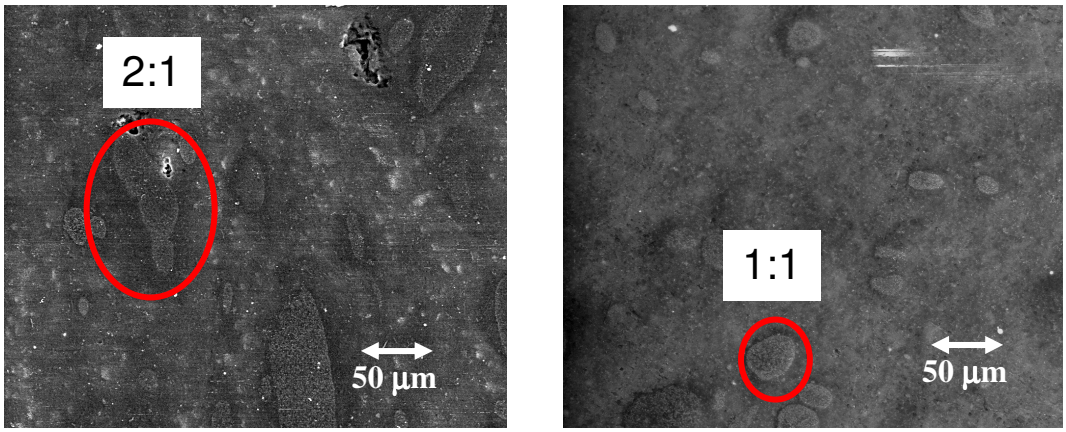

(a) **(b)**

Figure 4.7 Scanning electron micrographs of the extruded PS-CNF composites processed at a screw speed of (a) 30 RPM showing the relatively bigger agglomerates of CNFs, and **(b)** 200 RPM showing the relatively smaller agglomerates of CNFs.

4.1.6 Porosity of Extruded PS – CNF Composites

The porosity of the extruded PS-CNF composites, caused by the air entrained in the CNFs, was controlled by using a vacuum pump as described in 3.2.2.3 in order to study the effect of porosity on material properties. The qualitative distribution of pores in the PS-CNF composites, with and without a vacuum pump in the extrusion line, was characterized using optical microscopy as shown in figure 4.8. It is evident that using the vacuum pump reduces porosity in the composites, but does not eliminate it completely.

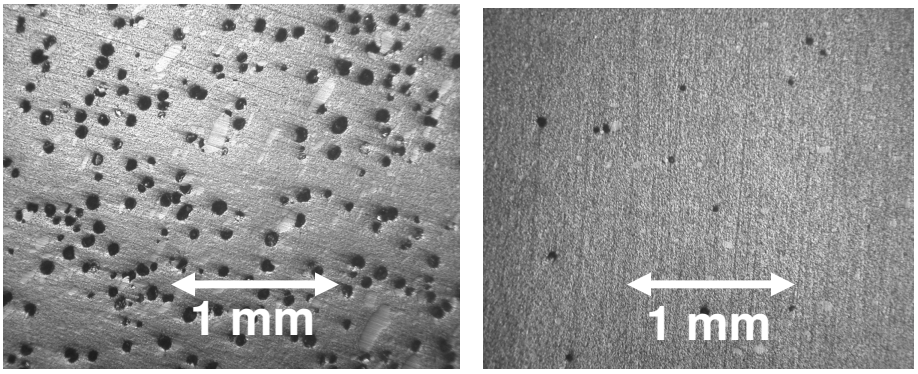

Figure 4.8 Representative optical micrographs of extruded PS-CNF composites showing porosity in the **(a)** absence, and **(b)** presence of a vacuum pump.

4.2 Structure – Property & Processing – Property Relationships

The material properties of the solvent processed PS-MWCNT, solvent processed PS-CNF and extruded PS-CNF composites were studied as a function of their structure (i.e., composition) and compared when applicable. Furthermore, the affect of processing parameters, within a type of process, on the properties was also studied. Table 4.1 gives an overview of the properties investigated. '√' or 'X' indicate that the property was investigated or not investigated, respectively.

Table 4.1 List of composites and material properties investigated for structure-property relationships. √ = Investigated, X= Not Investigated.

	Solvent Processed PS-MWCNT	Solvent Processed PS-CNF	Extruded PS-CNF
Electrical	√	√	√
Rheological	√	√	√
Thermo-oxidative	X	√	√
Mechanical	X	X	√

4.2.1 Solvent Processed PS – MWCNT Composites

4.2.1.1 Electrical Conductivity

Figure 4.9 shows the experimentally determined electrical conductivity (σ_c) of PS-MWCNT composites, processed using DMF and THF, as a function of the MWCNT loading. Each data point on the plot represents the average of measurements on 6-8 different samples, and the scatter in the data was within 5% of this average value. The conductivity of neat PS is ~10^{-20} S/m. Upon adding the MWCNTs, the conductivity of the composites increased by 20 orders of magnitude approaching a value of 1 S/m. At low loadings of MWCNTs, closer to the onset of percolation, the composites processed using DMF exhibit higher electrical conductivity than those processed using THF. The conductivity data are classically interpreted by a percolation model, which gives the following power law expression for conductivity as a function of particle volume fraction β:

$$\sigma_c^{PL} = \sigma_{PS} + A(\beta - \beta_c)^{\lambda} \qquad (4.1)$$

Here, σ_c^{PL} is the conductivity of the composite predicted by the power law fit, σ_{PS} is the electrical conductivity of the neat PS, A is a constant based on the interconnectivity of the MWCNTs, β_c is the percolation threshold and λ is the critical

exponent. The percolation threshold corresponds to the formation of a CNT network that allows electron transport by tunneling or electron hopping along CNT interconnects.

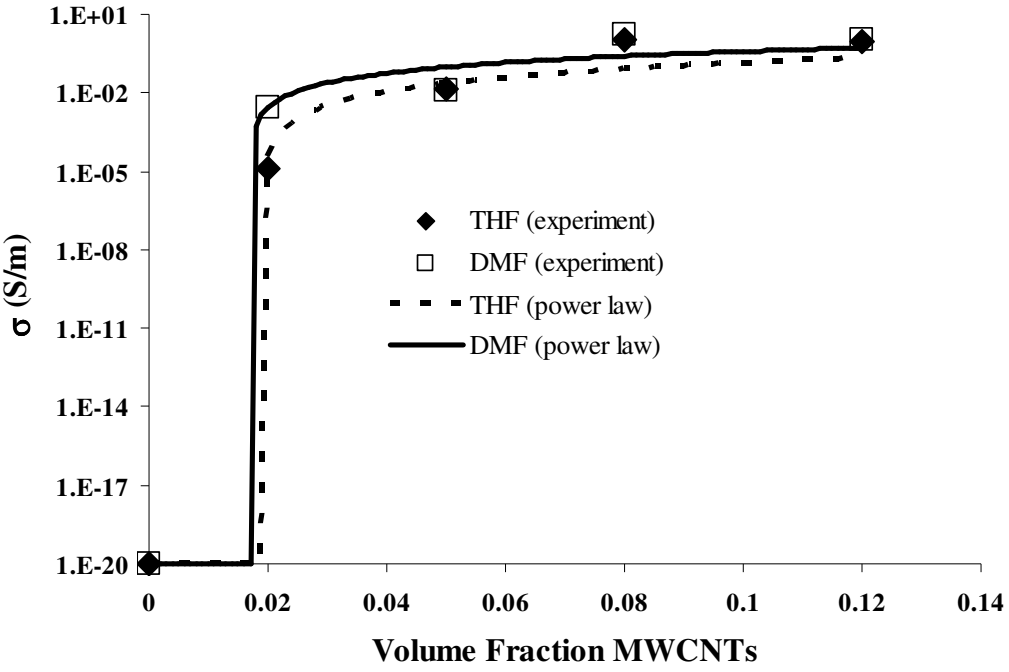

Figure 4.9 Electrical conductivity of the PS-MWCNT composites solvent processed using THF and DMF at various MWCNT loadings with the corresponding power law fits.

The conductivity data for PS-MWCNT composites in figure 4.9 were fit using equation (4.1) and the best fit parameters are listed in table 4.2. For the curve fit, mass fractions (w) were converted to volume fractions (values in table 4.3) using the simple rule of mixtures as shown in equation (4.2).

$$\beta = \frac{w\,\rho_{PS}}{\rho_{filler} + w\,(\rho_{PS} - \rho_{filler})} \qquad (4.2)$$

Here, ρ_{PS} is the density of PS and ρ_{filler} is the density of the filler, i.e., MWCNTs. The power law fits to the electrical conductivity data of both the DMF and THF-processed composites yielded a normalized cross-correlation coefficient of 1.00.

Table 4.2 The power law fit parameters for the electrical conductivity of the PS-MWCNT composites processed using THF and DMF solvents.

Power law parameter	THF (σ_c)	DMF (σ_c)
A	16	16
β_c	0.019	0.017
λ	1.9	1.5

Table 4.3 Relationship between mass and volume fractions for PS-MWCNT composites.

Mass Fraction	Volume Fraction
0.01	0.02
0.03	0.05
0.05	0.08
0.07	0.12

From figure 4.9, it can be seen that percolation begins near a volume fraction of 0.017 in the DMF processed composites and 0.019 in the THF processed ones. Beyond this point, there are distinct differences in the percolation behavior depending on the solvent used. The composites that are solvent processed with DMF percolate more rapidly than those processed with THF as described by the critical exponents 1.5 and 1.9 respectively. However, the choice of solvent does not appear to affect the conductivity of the fully-percolated composite, which in both cases is ~ 1 S/m. This value is reached at about 8 vol.% MWCNTs. Thus, the interconnectivity of MWCNTs is only slightly better using DMF than THF. An important conclusion can be drawn about the processing-property relationships in solvent processed PS-MWCNT composites from these observations: the difference in the percolation thresholds for the two solvents indicates that *the choice of solvent does not have a significant effect on electrical properties*.

4.2.1.2 Rheological Properties

The structure-property relationships for solvent processed PS-MWCNT composites were further investigated for their dynamic melt rheological properties to compare with those of the solvent processed PS-CNF composites that will be discussed in 4.2.2.3. Figures 4.10-4.13 show the various rheological parameters obtained from the THF processed PS-MWCNT composites. Figures 4.10a and 4.10b show the storage modulus G' and the loss modulus G'' as functions of frequency. Data collected over a temperature range of 170°C-210°C have been shifted using the time-temperature superposition principle to extend the frequency range, and are reported at the median temperature of 190°C. Both G' and G'' increase with MWCNT loading.

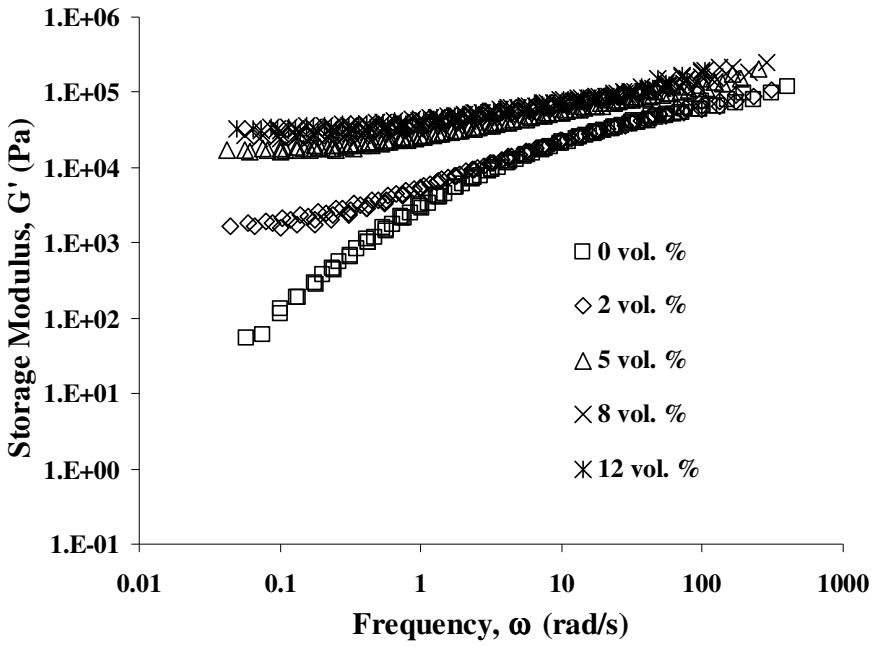

(a)

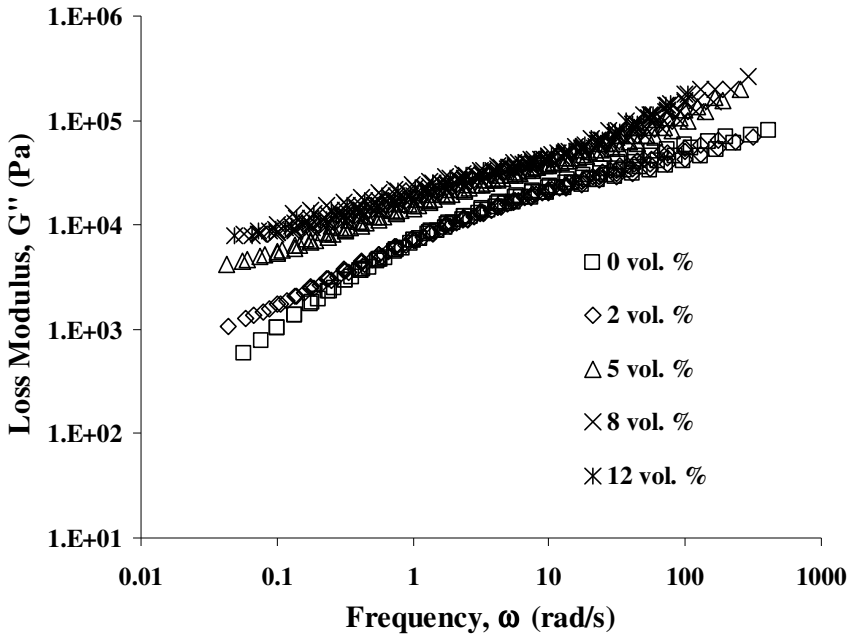

(b)

Figure 4.10 (a) Storage modulus (G') and **(b)** loss modulus (G'') of the solvent processed PS-MWCNT composites as a function of frequency. Data are shown for a range of MWCNT loadings. Note the plateau in G' at low frequencies for all of the MWCNT loadings indicating the presence of a pseudo-solid like phase in the composite formed by percolated MWCNTs.

More importantly, at loadings exceeding 2 vol.%, G' reaches a plateau at low frequencies indicating that the percolated MWCNTs may be forming a pseudo-solid like network with strong interactions between polymer and particles [83,84].

Evidence of the formation of a pseudo-solid like network of percolated MWCNTs can also be seen in Figure 4.11, where the variation of G' and G'' with frequency is compared for the neat PS sample and for the composite with the highest MWCNT loading of 12 vol. %. While the neat PS melt shows a typical transition from elastic to viscous behavior ($G'' > G'$) at a critical frequency of 13 rad/s, the composite shows a predominantly elastic response ($G' > G''$, plateau in G') over the entire frequency range.

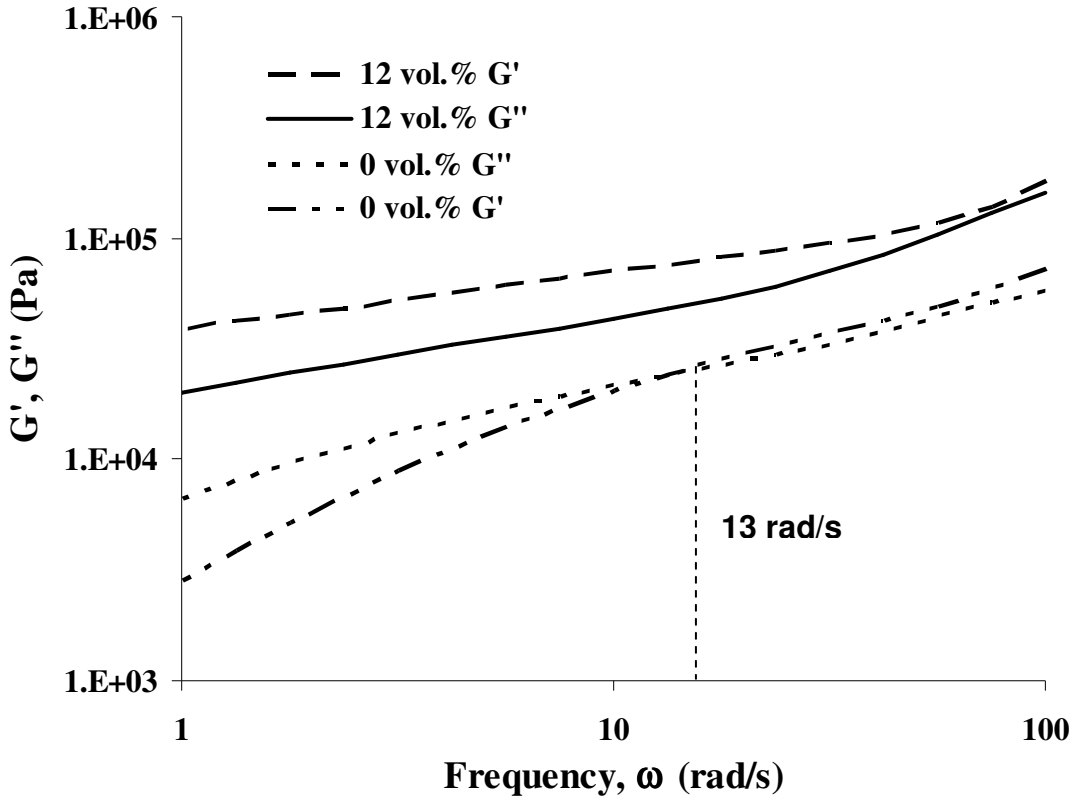

Figure 4.11 Cross-over point of the G' and G" curves for the neat PS and the 12 vol.% MWCNT composites. While the neat PS shows a viscous response at lower frequencies, the 12 vol.% MWCNT composite shows a predominantly elastic response over the entire frequency range.

Differences in rheological response upon addition of MWCNTs can also be noted in the complex viscosity η^*. It can be seen from figure 4.12a that the neat PS melt shows a newtonian plateau in η^* at low frequencies. On the other hand, the η^* curves for non-zero MWCNT loadings do not show a plateau over the frequency range, indicative of elastic behavior in the PS-MWCNT composites due to interactions between the MWCNTs. As the loading of MWCNTs increases, a percolated network forms and the composite develops a finite yield behavior. Correspondingly, a plot of η^* vs. the complex modulus G^* exhibits divergence at loadings above 2 vol.%, as shown in figure 4.12b [85].

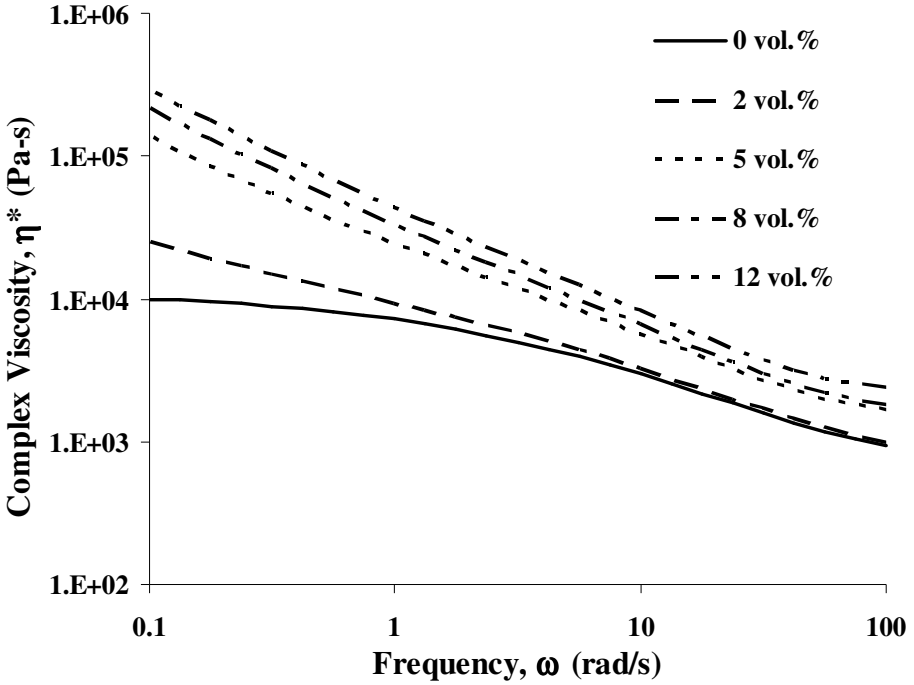

(a)

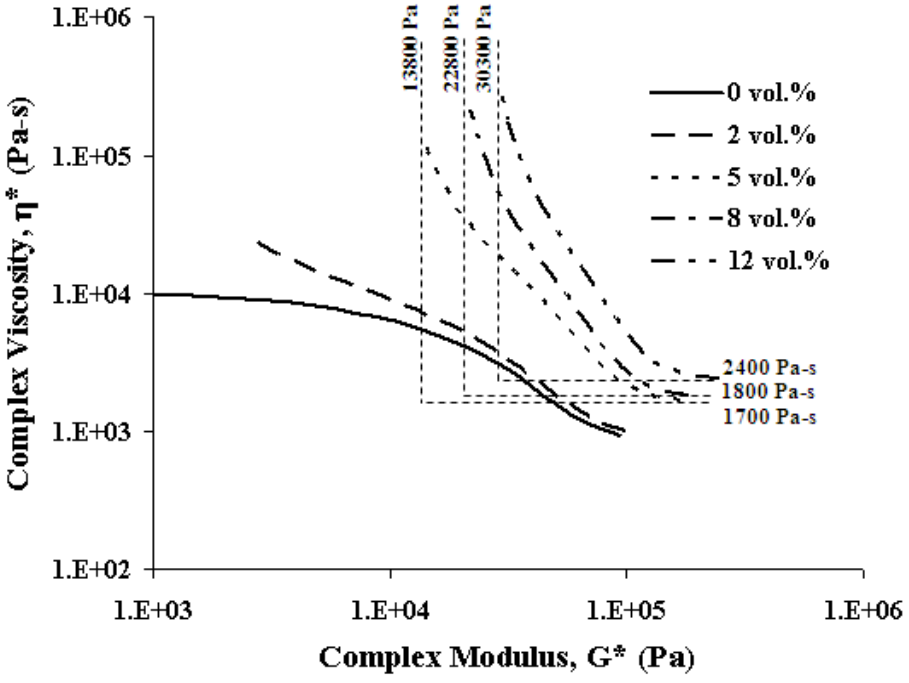

(b)

Figure 4.12 Complex viscosity (η^*) as a function of **(a)** frequency (ω), and **(b)** complex modulus (G^*) for the PS-MWCNT composites processed with THF and tested at a temperature of 190°C. Data are shown for a range of MWCNT loadings. Note the plateau in complex viscosity in the high complex modulus regime.

The asymptotic complex modulus increases from 13800 Pa at an MWCNT loading of 5 vol. % to 30300 Pa at 12 vol. %. In addition, while neat PS exhibits a plateau in complex viscosity in the low complex modulus regime, the diverging curves of PS-MWCNT composites exhibit complex viscosity plateaus, ranging from 1700 Pa-s at 5 vol. % to 2400 Pa-s at 12 vol. %, in the high complex modulus regime.

Additional insight into the interaction between the MWCNTs and the PS matrix can be obtained from the inverse loss tangent (G'/G''), which is a measure of the damping characteristics or firmness of the material [86]. As shown in figure 4.13, the inverse loss tangent increases with MWCNT loading, especially at low frequencies. This indicates a hindrance to energy dissipation and relaxation of the polymer chains due to the percolation of the MWCNTs.

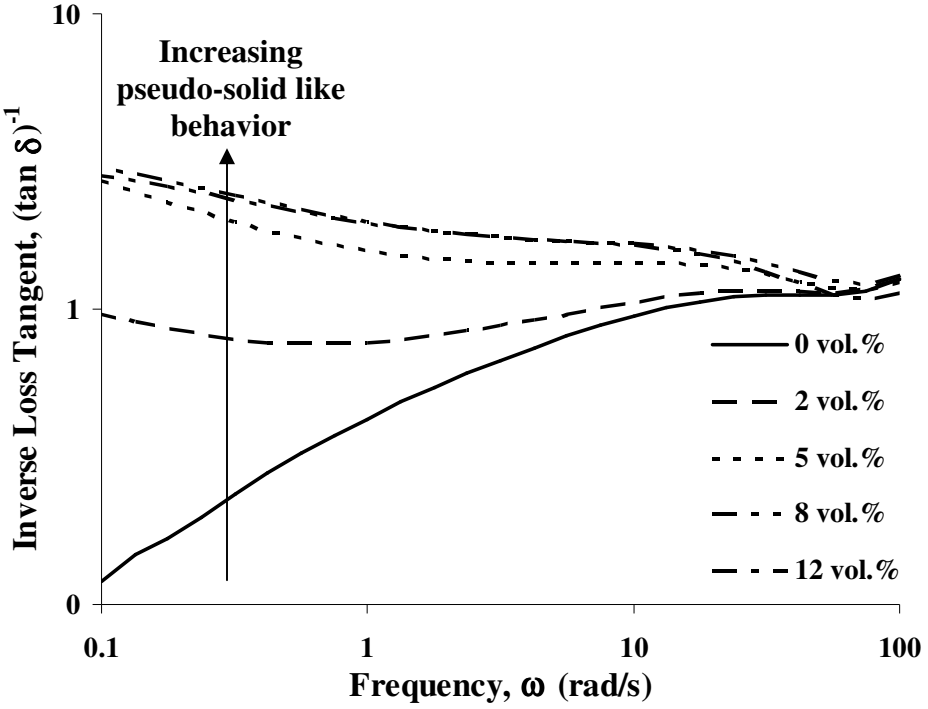

Figure 4.13 Inverse loss tangent as a function of frequency. Note the increase in inverse loss tangent with MWCNT loading.

4.2.1.3 Comparison of Electrical and Rheological Percolation

The inter-relationship between electrical and rheological properties in terms of the structure-property relationships of PS-MWCNT composites was also investigated to understand the difference in using these properties to establish percolation of MWCNTs. A closer examination of the low frequency (0.1 rad/s), microstructure sensitive regime of figures 4.10-4.13 shows an increase in all the rheological parameters with MWCNT loading for the THF processed composites. As expected from previous research investigations [14,84], the parameter whose absolute values are most sensitive to particle loading is the storage modulus G', which increased by more than 2 orders of magnitude upon adding MWCNTs. Over the same range of MWCNT loadings, the absolute values of η^*, G'', and G'/G'' each increased by about an order of magnitude.

Similar to the electrical percolation threshold, rheological percolation threshold is correlated with the onset of power law dependence of a rheological property on the volume fraction. However, there is no agreement on which quantity to use in this regard: for example, while Du et al [51] report the percolation based on G', Kharchenko et al [83] report the percolation based on G'/G''. In order to understand which rheological parameter describes percolation better, the normalized-log values of various directly measured ($\overline{\log G'}$ and $\overline{\log G''}$) and derived rheological parameters($\overline{\log \eta^*}$ and $\overline{\log(G'/G'')}$) are plotted in figure 4.14, and compared with the normalized-log values of electrical conductivity ($\overline{\log \sigma_c}$) and the power law predictions of electrical conductivity ($\overline{\log \sigma_c^{PL}}$). In addition, a power law of the form described by equation (4.1) was used to

fit the G'' and η^* data (fit parameters in table 4.4) and the normalized log-values of the modified power law predictions ($(\overline{\log G''} \ \& \ \overline{\log \eta^*})^{PL}$) are also plotted in figure 4.14.

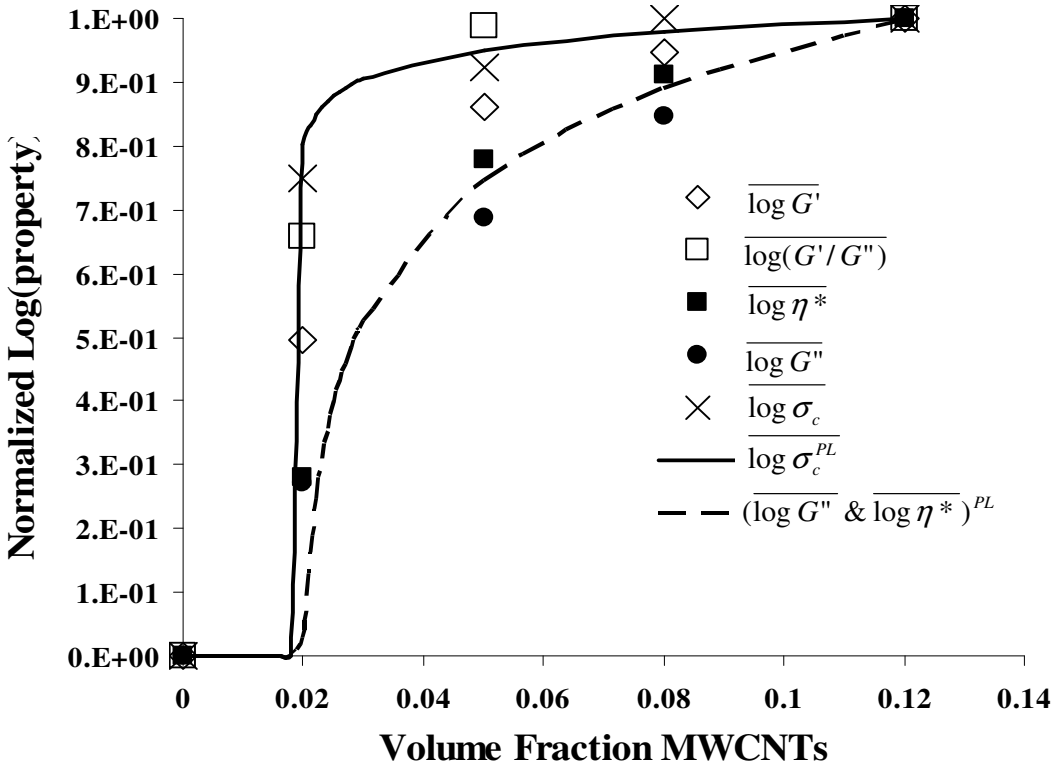

Figure 4.14 The log-normalized values of storage modulus ($\overline{\log G'}$) , loss modulus ($\overline{\log G''}$), complex viscosity ($\overline{\log \eta^*}$) and inverse loss tangent ($\overline{\log(G'/G'')}$), electrical conductivity ($\overline{\log \sigma_c}$) and the power law fit for electrical conductivity ($\overline{\log \sigma_c^{PL}}$) as a function of the MWCNT loading at 190°C for THF processed composites. The rheological data were obtained from figures 4.10, 4.12 and 4.13 at a frequency of 0.1 rad/s. The viscous rheological parameters, $G''\&\eta^*$, exhibit a gradual percolation rate, and hence a modified power law fit ($(\overline{\log G''} \ \& \ \overline{\log \eta^*})^{PL}$) was used.

Table 4.4 The power law fit parameters for the rheological properties of the PS-MWCNT composites processed using THF.

Power law parameter	**THF ($\overline{\log G''} \ \& \ \overline{\log \eta^*}$)**
A	16
β_c	0.019
λ	7

An inspection of figure 4.14 reveals that $\overline{\log G''}$ and $\overline{\log \eta^*}$ exhibit a percolation behavior that is far more gradual when compared to $\overline{\log G'}$ and $\overline{\log G'/G''}$ and $\overline{\log \sigma_c}$. Quantitative comparisons between fits were made using normalized cross-correlation coefficient values (table 4.5). Both $\overline{\log G''}$ and $\overline{\log \eta^*}$ seem to match well with $(\overline{\log G''} \ \& \ \overline{\log \eta^*})^{PL}$ yielding normalized cross-correlation coefficients of 0.97 and 0.98 respectively, as opposed to 0.86 and 0.87 respectively when compared with $\overline{\log \sigma_c^{PL}}$. At lower loadings of MWCNTs, closer to the electrical percolation threshold, $\overline{\log G'/G''}$ matches better with $\overline{\log \sigma_c^{PL}}$ when compared to $\overline{\log G'}$. At higher loadings, both $\overline{\log G'}$ and $\overline{\log G'/G''}$ match well with $\overline{\log \sigma_c^{PL}}$. Overall, comparing $\overline{\log G'}$ and $\overline{\log G'/G''}$ with $\overline{\log \sigma_c^{PL}}$ yielded normalized cross-correlation coefficients of 0.95 and 0.98 respectively, as opposed to 0.92 and 0.84 respectively when compared with $(\overline{\log G''} \ \& \ \overline{\log \eta^*})^{PL}$.

Table 4.5 Normalized cross-correlation values for the normalized log of rheological parameters for PS-MWCNT nanocomposites processed with THF solvent when compared with the normalized log of the power law fits to the electrical conductivity measurements for THF processed PS-MWCNT nanocomposites and the fits to $\overline{\log G''} \ \& \ \overline{\log \eta^*}$ in figure 4.14.

Rheological Parameter	**Power law** $(\overline{\log \sigma_c^{PL}})$	**Power law** $(\overline{\log G''} \ \& \ \overline{\log \eta^*})$
G'	0.95	0.92
G'/G''	0.98	0.84
G''	0.86	0.97
η^*	0.87	0.98

It can be noted that while G' and G'' are directly measured rheological parameters, η^* and G'/G'' are derived rheological parameters that have physical significance in terms

of the flow and firmness of the nanocomposites. An important conclusion can be drawn from figure 4.14: *to report rheological percolation, G´ is a good choice among the directly measured rheological parameters, and G´/G˝ is a good choice among the derived rheological parameters due to the steep increase in their values at low MWCNT loadings*. Microstructurally, this indicates that the elastic load transfer and electrical conductivity are far more sensitive to the onset of percolated MWCNTs than the viscous dissipation mechanisms as quantified by the change in the power law exponent.

4.2.1.4 Effect of Solvent on Rheological Percolation

In order to study the influence of solvent on rheological percolation, the variation of η^* with G^* obtained from the DMF-processed composites (figure 4.15) was compared with that obtained from the THF-processed ones (figure 4.12b). In figure 4.15, the asymptotic complex modulus increases from 11600 Pa at 5 vol. % MWCNTs to 37500 Pa at 12 vol. %. Comparing with figure 4.12b, the G^* value at 12 vol. % is 25% greater for the DMF-processed composites as compared to the THF ones. The diverging curves of the DMF-processed composites exhibit complex viscosity plateaus similar to those observed with THF ones and their values range from 1350 Pa-s at an MWCNT loading of 5 vol. % to 2300 Pa-s at 12 vol. %. However, the complex viscosity plateau for the fully percolated (12 vol.%) composites does not vary significantly with the choice of solvent.

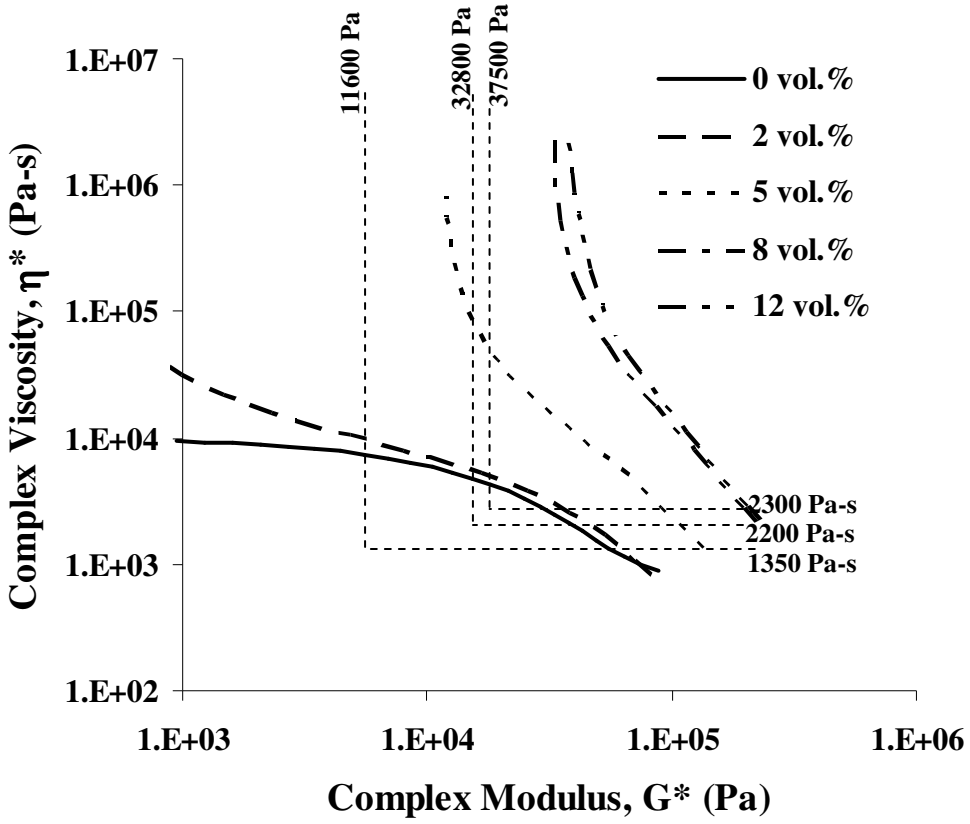

Figure 4.15 Complex viscosity (η^*) as a function of complex modulus (G^*) for the PS-MWCNT composites processed with DMF and tested at a temperature of 190°C. Data are shown for a range of MWCNT loadings. Note the plateau in complex viscosity in the high complex modulus regime.

Next, the normalized log-values of various rheological parameters and electrical conductivity obtained from the DMF-processed composites (figure 4.16) were compared with those obtained from the THF-processed ones (figure 4.14) using the normalized cross-correlation coefficients (table 4.6).

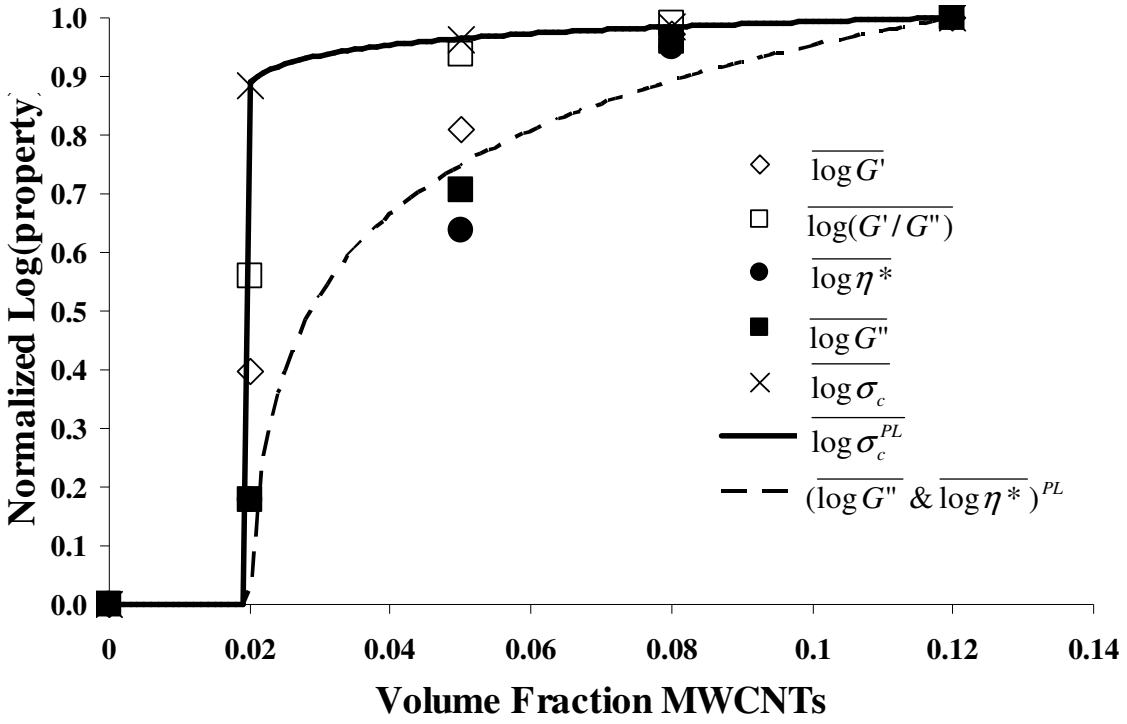

Figure 4.16 The log-normalized values of storage modulus ($\overline{\log G'}$) , loss modulus ($\overline{\log G''}$), complex viscosity ($\overline{\log \eta^*}$) and inverse loss tangent ($\overline{\log(G'/G'')}$), electrical conductivity ($\overline{\log \sigma_c}$) and the power law fit for electrical conductivity ($\overline{\log \sigma_c^{PL}}$) as a function of the MWCNT loading at 190°C for DMF processed composites. The rheological data was obtained at a frequency of 0.1 rad/s. Note that η^* and G'' percolate similar to that predicted by the modified power law ($(\overline{\log G''}\ \&\ \overline{\log \eta^*})^{PL}$) for THF processed composites. However, G' and G'/G'' percolate more gradually compared to σ_c . This is in contrast to that observed with the THF processed composites.

Table 4.6 Normalized cross-correlation values for the normalized log of rheological parameters for PS-MWCNT nanocomposites processed with DMF solvent when compared with the normalized log of the power law fits to the electrical conductivity measurements for DMF processed PS-MWCNT nanocomposites and the fits to $\overline{\log G''}\ \&\ \overline{\log \eta^*}$ in figure 4.16.

Rheological Parameter	**Power law ($\overline{\log \sigma_c^{PL}}$)**	**Power law ($\overline{\log G''}\ \&\ \overline{\log \eta^*}$)**
G'	0.88	0.95
G'/G''	0.94	0.89
G''	0.76	0.98
η^*	0.77	0.99

Figure 4.16 reveals that in DMF-processed composites, $\overline{\log G''}$ and $\overline{\log \eta^*}$ exhibit a percolation behavior that is more gradual when compared to $\overline{\log G'}$, $\overline{\log G'/G''}$ and $\overline{\log \sigma_c^{PL}}$. Both $\overline{\log G''}$ and $\overline{\log \eta^*}$ seem to match well with $(\overline{\log G''}\ \&\ \overline{\log \eta^*})^{PL}$ yielding normalized cross-correlation coefficients of 0.98 and 0.99 respectively, as opposed to 0.76 and 0.77 respectively when compared with $\overline{\log \sigma_c^{PL}}$. This behavior is similar to that observed in the THF processed composites. However, in the DMF-processed composites, unlike the THF-processed ones, both $\overline{\log G'}$ and $\overline{\log G'/G''}$ increase more gradually when compared with $\overline{\log \sigma_c^{PL}}$ yielding normalized cross-correlation coefficients of 0.88 and 0.94 respectively, as opposed to 0.95 and 0.89 respectively when compared with $(\overline{\log G''}\ \&\ \overline{\log \eta^*})^{PL}$. This indicates that DMF influences the electrical conductivity more than the elastic behavior of the composites, unlike THF. Thus, an important conclusion can be drawn about the processing-property relationships in solvent processed PS-MWCNT composites from these observations: *the choice of solvent has a slight effect on the differences between rheological and electrical percolation*. All of these results are consistent with previous investigations [87] on the effect of solvents on electrospinning of PS, where the conductivity of the PS solutions with DMF was found to be 2.4 μS/cm, compared to ~0 μS/cm with THF, and the surface tension was found to be 34.339 mN/m with DMF, compared to 24.735 mN/m with THF.

4.2.1.5 Modeling as an Interpenetrating Phase Composite

In order to gain further insight into the relationship between electrical and rheological percolation, the PS-MWCNT composite is considered as a combination of two phases: a continuous PS phase reinforced by non-interacting MWCNTs, and a continuous phase consisting of a pseudo-solid like network of percolated MWCNTs, as identified in 4.1.1. In order to quantify the distribution of MWCNTs among the phases, the *degree of percolation* ($\overline{C}(\beta)$) is proposed as:

$$\overline{C}(\beta) = \frac{\sigma_c^{PL}(\beta)}{\sigma_c^{PLPT0}(\beta)} \tag{4.3}$$

where $\sigma_c^{PLPT0}(\beta)$ is the value of electrical conductivity according to the power law fit when the percolation threshold is 0 vol. % (i.e., instantaneous percolation). Thus, the degree of percolation reflects the offset in the connectivity of the MWCNTs that begins above the percolation threshold. The degree of percolation $\overline{C}(\beta)$ as a function of volume fraction can be seen in figure 4.17.

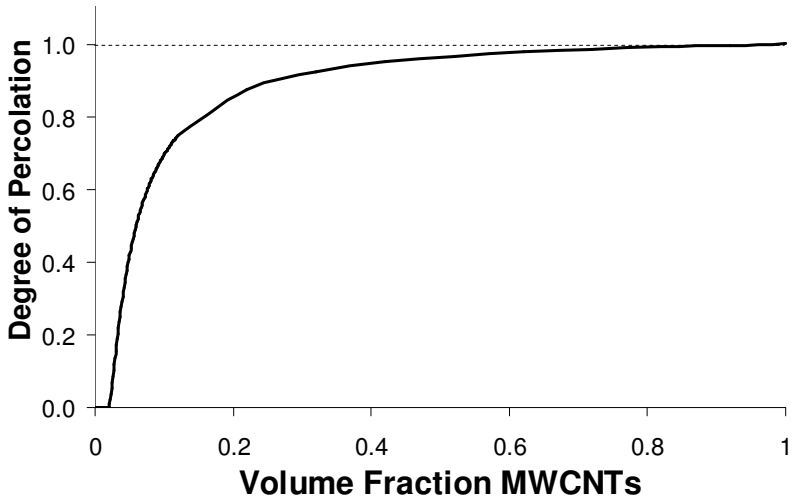

Figure 4.17 Degree of percolation at various MWCNT loadings.

The $\overline{C}(\beta)$ based on the power law model converges to the theoretical maximum above a volume fraction of 0.6, which is close to the classical theoretical maximum packing fraction for cylinders of 0.79 where full percolation of the microstructure would have to occur. This indicates that the degree of percolation obtained from the power law fit can provide a physically reasonable prediction of the distribution of MWCNTs among the interpenetrating phases. The degree of percolation corresponding to each of the compositions that was characterized is shown in table 4.7.

Table 4.7 The degree of percolation calculated from the electrical conductivity measurements for each composition using the power law fit.

Mass Fraction	Volume Fraction	Degree of Percolation
0.01	0.02	0.00
0.03	0.05	0.42
0.05	0.08	0.62
0.07	0.12	0.75

By using a linear rule-of-mixtures formulation commonly employed for predicting the properties of interpenetrating phase composites [88,89], the product of the degree of percolation and the volume fraction can be used to quantify the contribution of each phase to the dynamic rheological properties of the composite: $\beta\overline{C}(\beta)$ for the continuous phase consisting of a pseudo-solid like network of percolated MWCNTs and $1-\beta\overline{C}(\beta)$ for the continuous phase of PS reinforced by non-interacting MWCNTs. Accordingly, the storage modulus, *G'*, and the loss modulus, *G''*, can each be represented as a function of the degree of percolation, $\overline{C}(\beta)$, frequency, ω, and MWCNT volume fraction, β, as shown in equations (4.4)-(4.9). The relationships in equations 4.4-4.9 are obtained from classical formulae used for describing the rheological response of

polymers, including the effect of non-interacting particles and the viscoelastic behavior of a solid [90-94]. The continuous phase of percolated MWCNTs is modeled using a frequency-dependent behavior of a elastic-viscoplastic solid observed in clay suspensions [90], while the unpercolated MWCNTs are modeled by using the classical Nielsen formula that introduces the concept of maximum packing using a generalized Kerner equation [94].

$$G'(\beta,\overline{C}(\beta),\omega)=\beta\,\overline{C}(\beta)\left[G'_{PMWCNT}(0)+\eta'_{PMWCNT}(\infty)\,\omega^{c}_{PMWCNT}\left(\left(\frac{\omega}{\omega^{c}_{PMWCNT}}\right)^{.5}+\left(\frac{\omega}{\omega^{c}_{PMWCNT}}\right)\right)\right]+$$
$$+(1-\beta\overline{C}(\beta))\left[\frac{1+A\left(\frac{G'_{RMWCNT}/G'_{PS}(\omega)-1}{G'_{RMWCNT}/G'_{PS}(\omega)+A}\right)\varphi(\beta)}{1-\left(\frac{G'_{RMWCNT}/G'_{PS}(\omega)-1}{G'_{RMWCNT}/G'_{PS}(\omega)+A}\right)\varphi(\beta)\psi(\varphi(\beta))}\right]G'_{PS}(\omega) \tag{4.4}$$

$$G''(\beta,\overline{C}(\beta),\omega)=\beta\,\overline{C}(\beta)\left[G''_{PMWCNT}(0)+\eta''_{PMWCNT}(\infty)\,\omega^{c}_{PMWCNT}\left(\left(\frac{\omega}{\omega^{c}_{PMWCNT}}\right)^{.5}+\left(\frac{\omega}{\omega^{c}_{PMWCNT}}\right)\right)\right]+$$
$$+(1-\beta\overline{C}(\beta))\left[\frac{1+A\left(\frac{G''_{RMWCNT}/G''_{PS}(\omega)-1}{G''_{RMWCNT}/G''_{PS}(\omega)+A}\right)\varphi(\beta)}{1-\left(\frac{G''_{RMWCNT}/G''_{PS}(\omega)-1}{G''_{RMWCNT}/G''_{PS}(\omega)+A}\right)\varphi(\beta)\psi(\varphi(\beta))}\right]G''_{PS}(\omega) \tag{4.5}$$

where,

$$G'_{PS}(\omega)=G^{p}_{PS}\frac{\left(\frac{\omega}{\omega^{c}_{PS}}\right)^{2p}}{\left(1+\left(\frac{\omega}{\omega^{c}_{PS}}\right)^{p}\right)^{2}} \tag{4.6}$$

$$G''_{PS}(\omega) = \eta_{PS}(0)\frac{\omega}{\left(1+\left(\frac{\omega}{\omega^{c}_{PS}}\right)^{q}\right)^{2}} \tag{4.7}$$

$$\psi(\varphi(\beta)) = 1 + (1-\varphi_m)\varphi(\beta)/\varphi_m^{\,2} \tag{4.8}$$

$$\varphi(\beta) = (\beta - \beta\overline{C})/(1-\beta\overline{C}) \tag{4.9}$$

and the following constants are determined by applying equations (4.4)-(4.7) to the experimental melt rheology data:

$G'_{PMWCNT}(0)$ = storage modulus of the continuous phase of percolated MWCNTs as $\varpi \to 0$

$\eta'_{PMWCNT}(\infty)$ = real part of complex viscosity for the continuous phase of percolated MWCNTs as $\varpi \to \infty$

G'_{RMWCNT} = effective storage modulus of the MWCNT reinforcement in the continuous PS phase

G^{p}_{PS} = plateau modulus of neat PS

$G''_{PMWCNT}(0)$ = loss modulus of the continuous phase of percolated MWCNTs as $\varpi \to 0$

$\eta''_{PMWCNT}(\infty)$ = imaginary part of complex viscosity for continuous phase of percolated MWCNTs as $\varpi \to \infty$

G''_{RMWCNT} = effective loss modulus of the MWCNT reinforcement in the continuous PS phase

$\eta_{PS}(0)$ = viscosity of neat PS as $\varpi \to 0$

$p,q,$ = power law indices

ω_{PS}^{c} , ω_{PMWCNT}^{c} = critical frequencies related to the relaxation of neat PS and percolated MWCNTs

A = shape and orientation factor of reinforcement

ϕ_M = maximum theoretical volume fraction of non-interacting MWCNTs

Thus, the degree of percolation obtained from the electrical conductivity measurements provides a means of distinguishing the effect of percolated and unpercolated MWCNTs. This essentially results in a modification of the Nielsen equation for unpercolated suspensions to include the effects of percolation.

The fits to the experimental data obtained from using the new rheological models and the degree of percolation can be seen in figure 4.18. These results indicate good correlation between the fits and the experimental data, and verify the appropriateness of the new rheological models for capturing the formation of the interpenetrating phase composite from the percolation of the MWCNTs. Thus, the new rheological models permit, for the first time, determination of the properties of the continuous phase consisting of a pseudo-solid like network of percolated MWCNTs. These values can be seen in table 4.8. The continuous phase of percolated MWCNTs exhibits an elastic solid like behavior at low frequencies with a complex modulus, $G_{PMWCNT}^{*}(0) = \sqrt{\left(G_{PMWCNT}^{'}(0)\right)^2 + \left(G_{PMWCNT}^{''}(0)\right)^2}$ = 360 kPa, and then transitions at higher frequencies to a viscoplastic solid like behavior with a complex viscosity, $\eta_{PMWCNT}^{*}(\infty) = \sqrt{\left(\eta_{PMWCNT}^{'}(\infty)\right)^2 + \left(\eta_{PMWCNT}^{''}(\infty)\right)^2}$ = 6 kPa-s/rad.

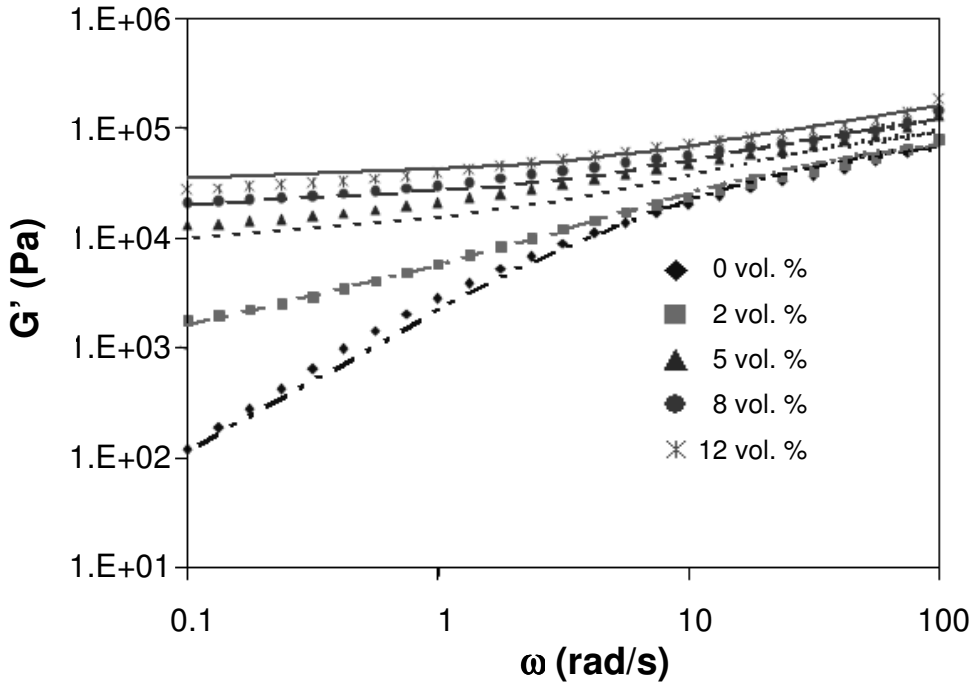

(a)

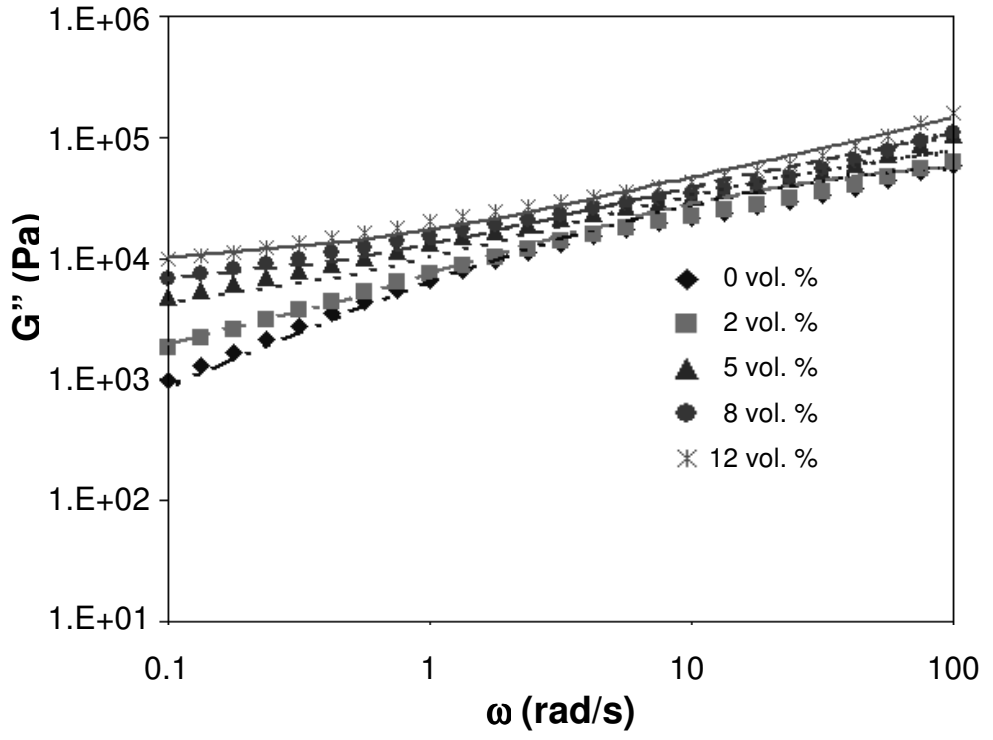

(b)

Figure 4.18 (a) Storage modulus (G') and **(b)** loss modulus (G'') of the composites as a function of frequency. Data are shown for a range of MWCNT loadings. Note that the fits from the proposed rheological model match well with the experimental data.

Table 4.8 Values of material properties determined from fitting experimental data for PS-MWCNT composite with the new rheological models

Constant	Value
$\eta'_{PMWCNT}(\infty)$	4 kPa-s/rad
$G'_{PMWCNT}(0)$	350 kPa
G'_{RMWCNT}	200 kPa
G^{p}_{PS}	100 kPa
$\eta''_{PMWCNT}(\infty)$	5 kPa-s/rad
$G''_{PMWCNT}(0)$	80 kPa
G''_{RMWCNT}	60 kPa
$\eta_{PS}(0)$	10 kPa-s/rad
P	0.70
Q	0.55
ω^{c}_{PS}	12 rad/s
ω^{c}_{PMWCNT}	80 rad/s
A	1000
ϕ_M	0.65

Simultaneously, it is possible to isolate the effects of the non-interacting MWCNTs that reinforce the PS. The reinforcing MWCNTs behave like an elastic solid with an effective complex modulus, $G^{*}_{RMWCNT}(0) = \sqrt{\left(G'_{RMWCNT}(0)\right)^2 + \left(G''_{RMWCNT}(0)\right)^2} = 208$ kPa.

The frequency response at low and high frequencies provides direct insight into the nature of the continuous phase of percolated MWCNTs. The normalized complex modulus, $G^{*}(\omega)/G^{*}(0)$, and the normalized complex viscosity, $\eta^{*}(\omega)/\eta^{*}(0)$, seen in figure 4.19 are consistent with the frequency independent modulus of an elastic solid at low frequencies and frequency independent viscosity of a viscoplastic solid at high frequencies. This behavior is indicative of a scaffold-like microstructure that exhibits a stick-slip friction mechanism at higher frequencies.

This aspect of the research has a very important implication: *it provides a new methodology for quantifying the continuous phase formed by the percolation of nanostructures in polymer nanocomposites* through the properties obtained using equations (4.4)-(4.9). It can be applied to functionalized nanostructures being developed for [95,96]: (a) controlling the percolation of the nanostructures through self-assembly, (b) enhancing their interaction with the continuous reinforced polymer phase, (c) enhancing the cohesion between nanostructures. This is possible because the continuous reinforced polymer phase stabilizes the state of the continuous phase of percolated nanostructures, which is similar in principle to the stabilization of proteins using formalin-fixed, paraffin-embedded tissue blocks for histopathology.

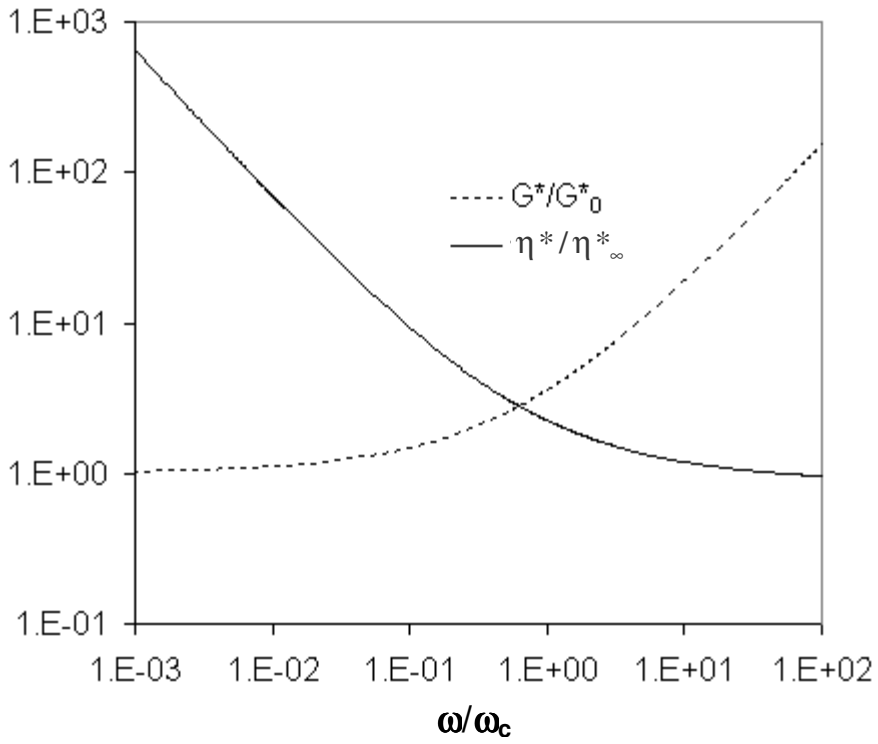

Figure 4.19 Normalized rheological properties of the continuous phase of percolated MWCNTs indicating elastic-viscoplastic behavior with a crossover in behavior from elastic to viscoplastic at the normalized frequency of 1.

4.2.2 PS – CNF Composites: Solvent Processed & Extruded

In order to further investigate the effects of processing on the structure-property and processing-property relationships in polymer nanocomposites, CNFs were used instead of MWCNTs to allow for larger quantities of less expensive but structurally and chemically similar nanoscale ingredients to be used in a commercial scale twin screw extruder. To rigorously investigate the effects of processing, the effect of the CNF ingredients on the structure-property relationships for solvent processed nanocomposites had to also be investigated as previously outlined in Table 4.1.

4.2.2.1 Electrical Conductivity: Solvent Processed

Figure 4.20 shows the experimentally determined electrical conductivity (σ_c) of solvent processed PS-CNF composites, processed using DMF, as a function of the CNF loading. Each data point on the plot represents the average of measurements on 6-8 different samples, and the scatter in the data was within 5% of this average value. The conductivity of neat PS is ~10^{-20} S/m. However, the detection limit of our measurements was ~10^{-8} S/m. Hence, all electrical conductivity values, which were below the detection limit, were assumed to be equal to 10^{-8} S/m. Upon adding the CNFs, the conductivity of the composites increased by 8 orders of magnitude approaching a value of 1 S/m with 10 wt.% CNF loading. Similar to the PS-MWCNT composites, the conductivity data of the PS-CNF composites were fit using the power law of the form shown in equation (4.10):

$$\sigma_c^{PL} = \sigma_{PS} + A(w - w_c)^{\lambda} \tag{4.10}$$

Here, σ_c^{PL} is the conductivity of the composite predicted by the power law fit, σ_{PS} is the electrical conductivity of the neat PS (assumed to be 10^{-8} S/m), A is a constant based on

the interconnectivity of the CNFs, w_c is the percolation threshold and λ is the critical exponent. The data were modeled in terms of weight fractions instead of volume fractions because the density of CNFs is unknown. The best fit parameters are listed in table 4.9.

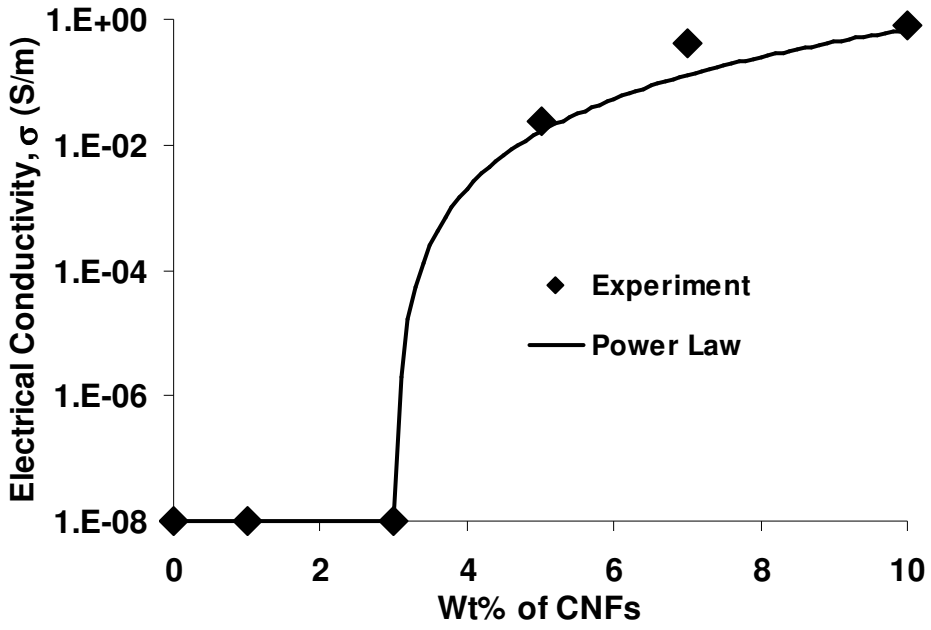

Figure 4.20 Electrical conductivity of the PS-CNF composites solvent processed using DMF at various CNF loadings. The corresponding power law fits are also shown.

Table 4.9 The power law fit parameters for the electrical conductivity of the PS-CNF composites processed using DMF.

Power law parameter	DMF (σ_c)
A	0.002
w_c	3
λ	3

It must be noted that the percolation threshold of the solvent processed PS-CNF composites is 3 wt.%, compared to 1 wt.% of the PS-MWCNT composites. Furthermore, the plateau in electrical conductivity was seen at ~10 wt.% for PS-CNF composites, compared to ~5 wt.% for the PS-MWCNT composites. However, the value of the peak electrical conductivity seems to asymptotically reach 1 S/m in both cases. From these

results a very important conclusion can be drawn about the effect of ingredients on structure-property relationships: *the differences in percolation threshold and the plateau in electrical conductivity can be attributed to the lower aspect ratio of CNFs (~30:1) when compared with MWCNTs (~100:1*).

4.2.2.2 Electrical Conductivity: Extruded & Annealed

The effect of processing on the structure-property relationships of the PS-CNF composites was further studied by comparing the electrical properties of the extruded polymer nanocomposites before and after annealing. Figure 4.21 shows the experimentally determined electrical conductivity (σ_c) of the solvent processed and extruded PS-CNF composites as a function of CNF loading. It is evident that the extruded composites exhibit a higher percolation threshold of 7 wt.%, compared to 3 wt.% of the solvent processed composites. At 10 wt.%, the extruded composites show an electrical conductivity of ~5 x 10^{-4} S/m, which is 3 orders of magnitude lower than ~0.8 S/m of the solvent processed composites. As described in 4.1.4, the higher percolation threshold and lower conductivity of the extruded composites can be attributed to the preferential alignment of CNFs, presumably due to the shear flow through the die.

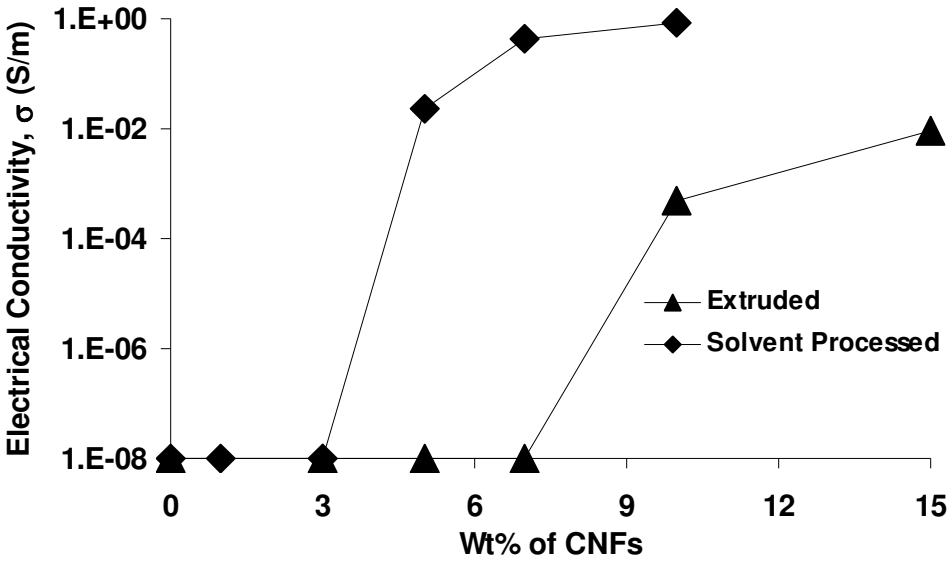

Figure 4.21 Electrical conductivity of the extruded and solvent processed PS-CNF composites at various CNF loadings.

Furthermore, it was observed that the electrical conductivity of the extruded PS-CNF composites changed significantly upon annealing. Figure 4.22 shows the influence of annealing temperature on the electrical conductivity of the extruded PS-CNF composites. The conductivity data for composites annealed at 170 and 200°C for 30 min are presented. It is evident that conductivity can be recovered by annealing at high temperatures. In the absence of annealing, i.e., for the as-extruded composites, a percolation threshold of 7 wt.% was observed with appreciable conductivities at 10 wt.% and 15 wt.% CNF loading. Annealing at 170°C for 30 min did not change the percolation threshold, but increased the conductivity by ~2 orders of magnitude. Annealing at 200°C for 30 minutes lowered the percolation threshold to 3 wt.% by imparting appreciable conductivities to the composite with 5 wt.% and 7 wt.% CNF loading. It was also observed that the choice of annealing temperature is crucial: higher than the softening point of PS (~ 150°C), but well below its thermal degradation temperature (~ 250°C). It

must be noted that all the electrical conductivity measurements were made at room temperature.

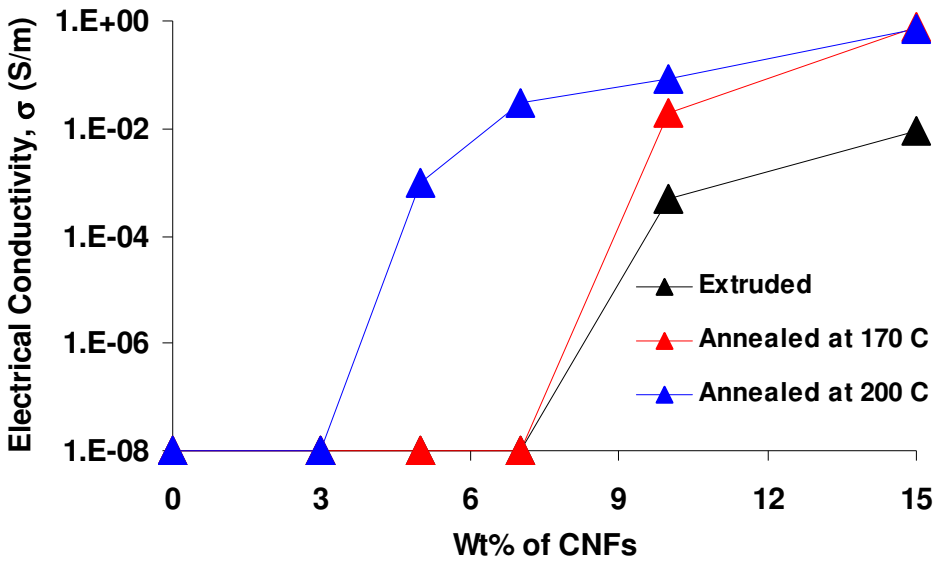

Figure 4.22 Effect of annealing temperature on electrical conductivity of extruded PS-CNF composites. The composites were annealed for 30 minutes. Note the lower percolation threshold at higher annealing temperature.

Figure 4.23 shows that in addition to annealing temperature, the annealing time also has an effect on the electrical conductivity of the PS-CNF composites. The conductivity data for composites annealed for 3 min and 30 min at 200°C are presented. It is evident that conductivity can be recovered by annealing for longer time. Annealing for 3 min at 200°C lowered the percolation threshold to 5 wt.% and increased the conductivity by ~2 orders of magnitude. Annealing for 30 minutes at 200°C lowered the percolation threshold to 3 wt.% by imparting appreciable conductivities to the composite with 5 wt.% and 7 wt.% CNF loading.

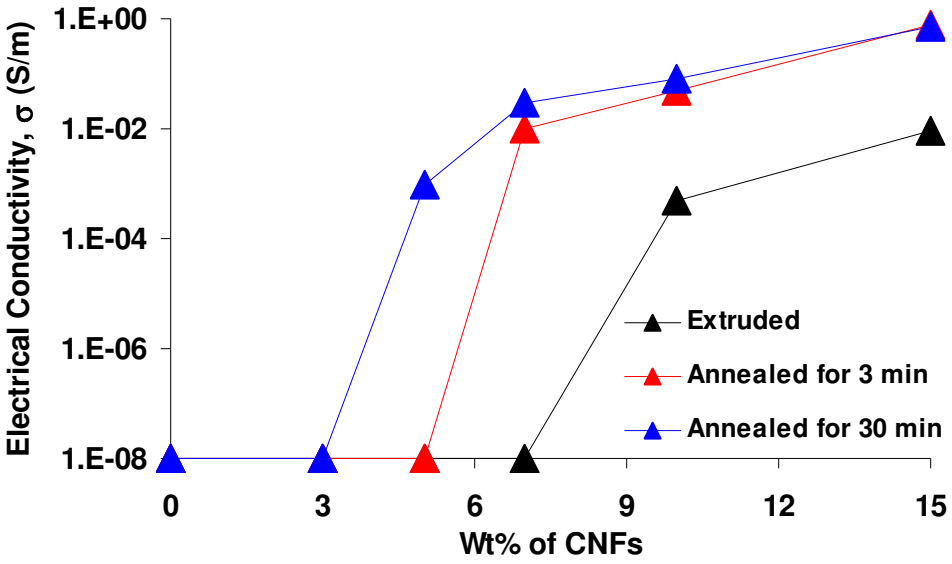

Figure 4.23 Effect of annealing time on electrical conductivity of extruded PS-CNF composites. The composites were annealed at 200°C. Note the lower percolation threshold at longer annealing times.

From these results an important conclusion can be drawn about the effect of processing on structure-property relationships: as described in 4.1.4, *annealing re-establishes the interconnectivity of preferentially aligned CNFs in the extruded composites* (see figure 4.6), thereby enhancing the electrical conductivity. The increase in electrical conductivity with increasing annealing temperature and annealing time suggests that the phenomenon is diffusion controlled. However, nanocomposites are typically non-Brownian systems due to their high matrix viscosity and the extended geometry of the filler particles [83,97-99]. Nevertheless, while translational diffusion may be limited, the particles may still be able to rotate and re-orient, even under non-Brownian conditions. Annealing at higher temperatures will promote such re-orientation because of the decrease in matrix viscosity and the increased thermal diffusivity. It is evident from figures 4.22 and 4.23 that the nanocomposites with higher particle loadings recover their conductivity after annealing at lower temperatures and for shorter times. At higher

loadings, the particles are sufficiently close to each other that they can re-form interconnects quite easily. However, at lower loadings, the particles need to re-orient and/or diffuse appreciable distances to form a link with their nearest neighbors. Similar reorganization under quiescent conditions at high temperatures (after shear, for example) was reported for clay particles in polymer/clay nanocomposites [98,99]. A further driving force for the re-orientation of clay particles was postulated to arise from strong attractive interaction between particles [99]. This may be a factor in the PS-CNF composites too, since it is known that CNFs experience stronger van der Waals interactions than clay particles due to their highly conductive nature.

4.2.2.3 Rheological Properties: Solvent Processed

The solvent processed PS-CNF composites were investigated for their dynamic rheological properties. Figure 4.24 shows the storage modulus G' and the loss modulus G'' of the DMF processed PS-CNF composites as functions of frequency. Both G' and G'' increase with CNF loading. At 3 wt.% loading of CNFs and above, G' reaches a plateau at low frequencies indicating that percolated CNFs may be forming a pseudo-solid like network with strong interactions between polymer and particles [83,84]. Similar, but less predominant effects are observed in G''.

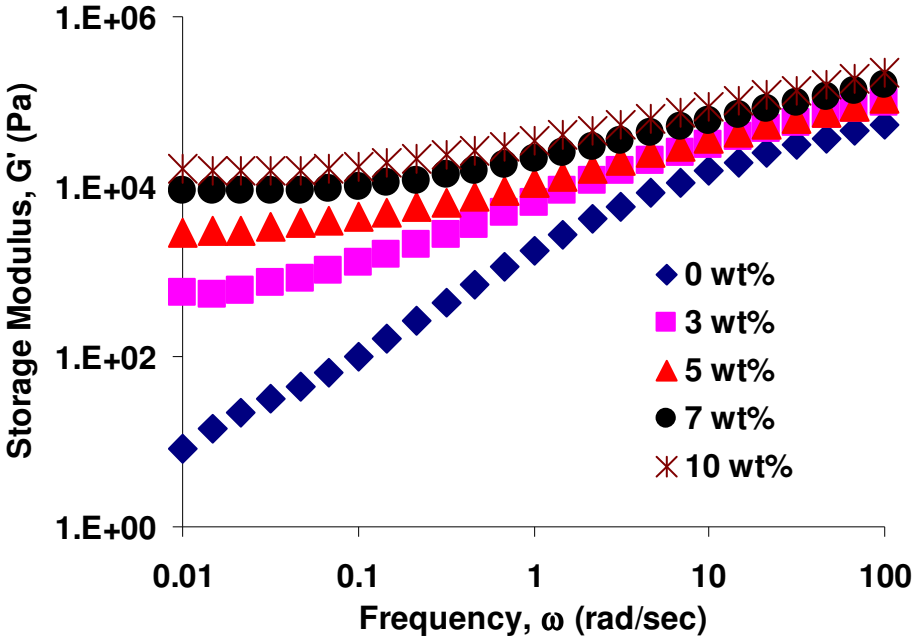

(a)

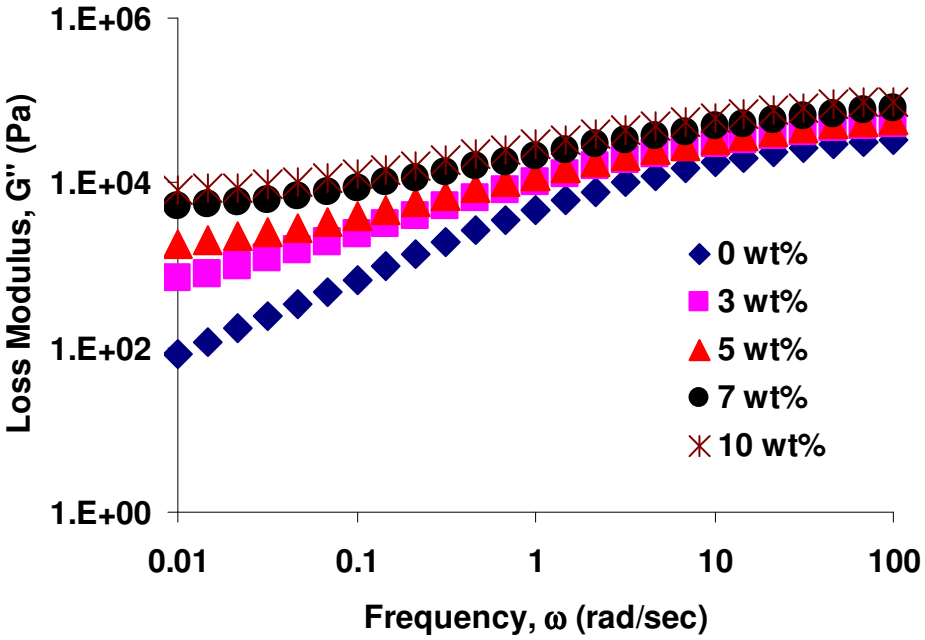

(b)

Figure 4.24 (a) Storage modulus (G') and **(b)** loss modulus (G'') of the solvent processed PS-CNF composites as a function of frequency at a temperature of 190°C. Data are shown for a range of CNF loadings. Note the plateau in G' at low frequencies for all of the CNF loadings indicating the presence of a pseudo-solid like phase in the composite formed by percolated CNFs.

Thus, the rheological percolation threshold qualitatively matches well with the electrical percolation threshold of the solvent processed PS-CNF composites. In addition, comparing figures 4.10 and 4.24, it is evident that the rheological behavior of the solvent processed PS-MWCNT and PS-CNF composites is similar, but the values of G' and G'' are consistently higher for the former. From these results, an important conclusion can be drawn about the effect of ingredients on the structure-property relationships: *due to the higher aspect ratio of MWCNTs when compared to the CNFs, the rheological properties are higher for the PS-MWCNT composites*.

4.2.2.4 Rheological Properties: Extruded & Annealed

The extruded PS-CNF composites were investigated for their dynamic rheological properties to compare with those of the solvent processed composites. Figure 4.25 shows the storage modulus G' and the loss modulus G'' of the extruded PS-CNF composites as functions of frequency. Comparing figures 4.24 and 4.25, it is evident that the rheological behavior of the extruded and solvent processed PS-CNF composites is similar. Both G' and G'' increase with CNF loading and at 3 wt.% loading of CNFs and above, G' reaches a plateau at low frequencies indicating that percolated CNFs may be forming a pseudo-solid like network with strong interactions between polymer and particles [83,84]. Similar, but less predominant effects are observed in G''. However, the values of G' and G'' of the extruded composites are consistently lower than solvent processed composites at all loadings. This can be attributed to the lower aspect ratio of CNFs in the extruded composites when compared to the solvent processed composites as described in 4.1.3.

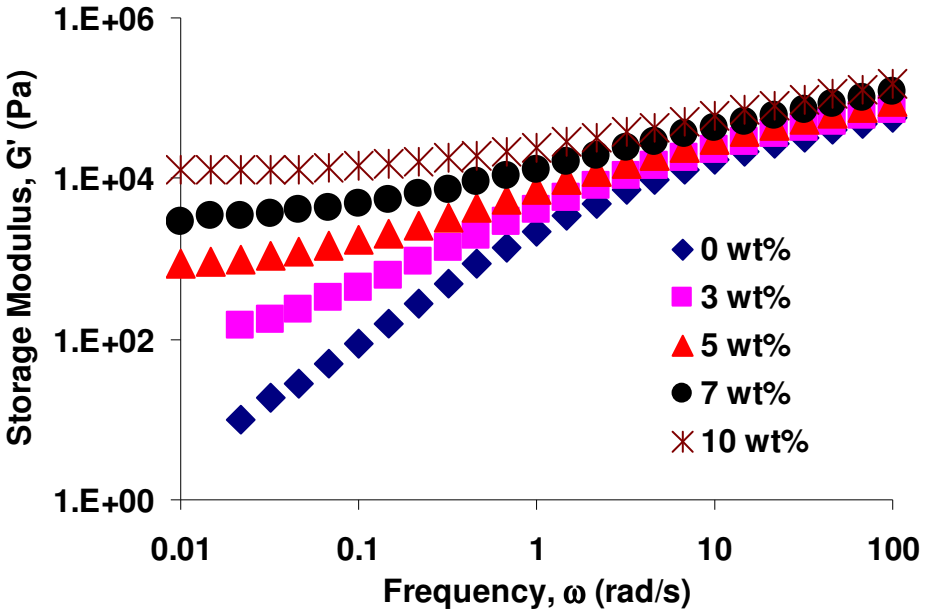

(a)

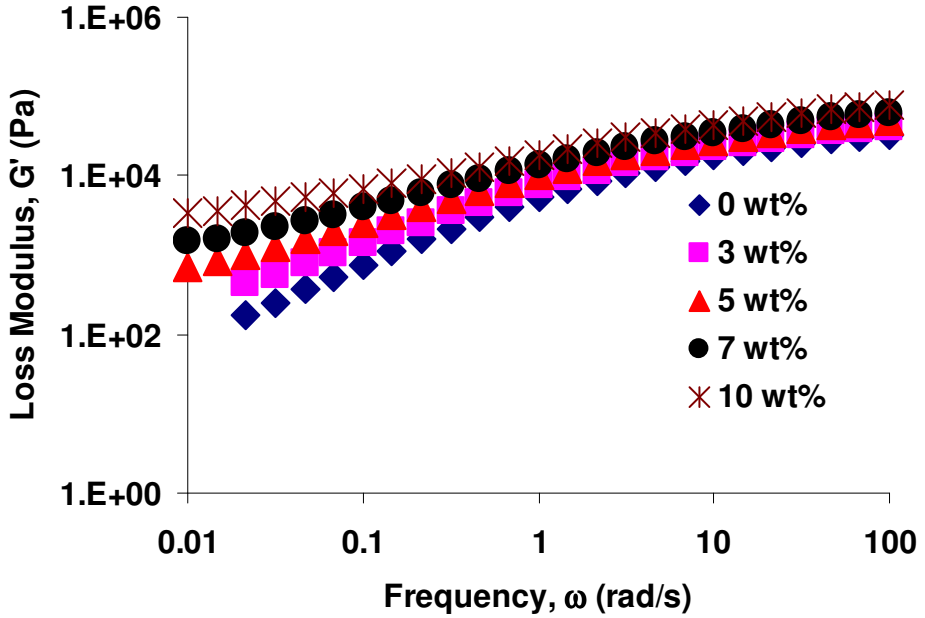

(b)

Figure 4.25 (a) Storage modulus (G') and **(b)** loss modulus (G'') of the extruded PS-CNF composites as a function of frequency at a temperature of 190°C. Data are shown for a range of CNF loadings. Note the lower values of G' and G'' when compared with the solvent processed PS-CNF composites shown in figure 4.24.

Furthermore, similar to electrical conductivity, annealing the extruded PS-CNF composites resulted in increased rheological properties. However, the increases in the rheological properties were not as significant as the electrical conductivity. Figure 4.26 shows the effect of annealing on the inverse loss tangent as a function of CNF loading. Inverse loss tangent, which represents the firmness of the material, shows a modest increase after annealing. In addition to the direct evidence provided by microscopy (see 4.1.4), this corroborates the re-establishment of connections between the CNFs that were lost during processing. It should be noted that the rheological data in figure 4.26 were obtained at 200°C by annealing for 30 mins. Indeed, it is then understandable that the differences in rheology at 200°C are modest compared to the differences in electrical conductivities of unannealed and annealed composites conducted at room temperature.

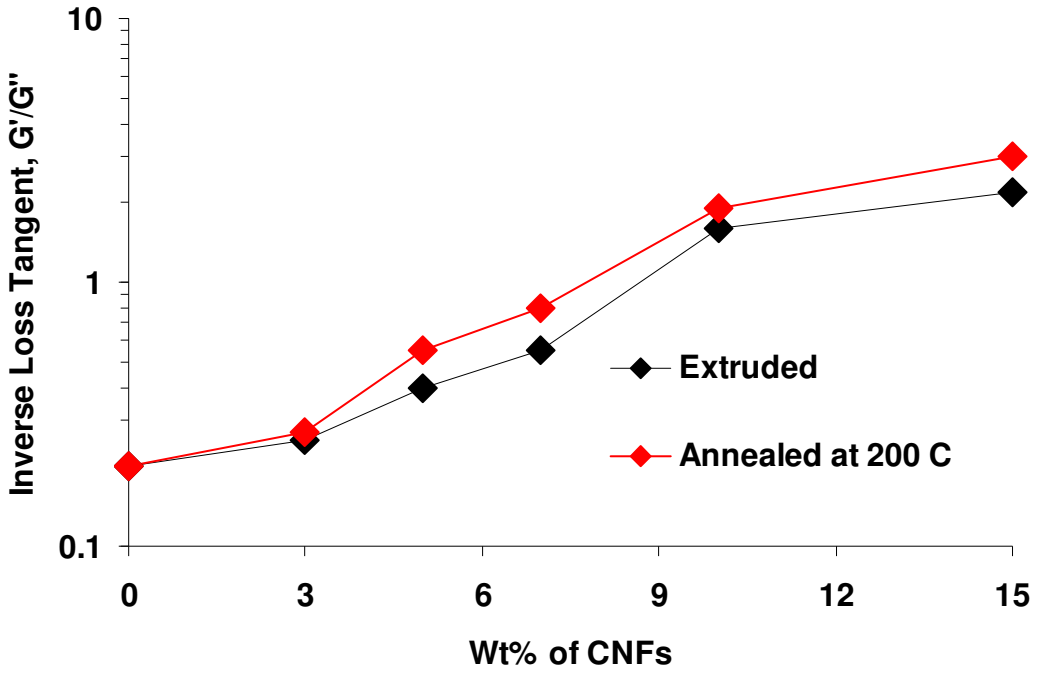

Figure 4.26 Effect of annealing on the rheological properties of extruded PS-CNF composites. The composites were annealed for 30 mins.

4.2.2.5 Thermo-oxidative behavior: Solvent Processed & Extruded

To understand the effects of processing on the thermo-oxidative behavior of the polymer phase and the filler phase in the PS-CNF composites, thermo gravimetric analysis was conducted at various CNF loadings in an unmixed, extruded and solvent processed state. For extruded PS-CNF composites, the effects of porosity, screw speed and screw design were also studied. The detailed experimental procedure was described in 3.3.1 and 3.4.3.

Figures 4.27a and 4.27b show the representative weight percent and weight loss rate (WLR) profiles respectively of the PS-CNF composites at various CNF loadings. The magnitude of the peak WLR of the styrene-rich phase as a function of the CNF loading can be seen in figure 4.27c. In contrast to the results reported in [55], figures 4.27a and 4.27b indicate that there is no significant effect of CNF loading on any of the three temperatures at peak weight loss rate (TPWLR) of the solvent processed or extruded PS-CNF composites. However, the magnitude of the peak WLR corresponding to the styrene-rich phase was found to quadratically decrease with CNF loading. This is consistent with the quadratic reduction in the WLR that is predicted by the simple combustion model [100] for an isotropic solid structure, such as a sphere or a cube, as its size is reduced (which is equivalent to a reduction in the volume fraction of the polymer). Thus, the reduction of the peak WLR of the composite is consistent with increasingly replacing the weight of PS with CNFs. The peak WLR decreases quadratically from 15.7 mg/min for neat PS to 0 mg/min for neat CNFs.

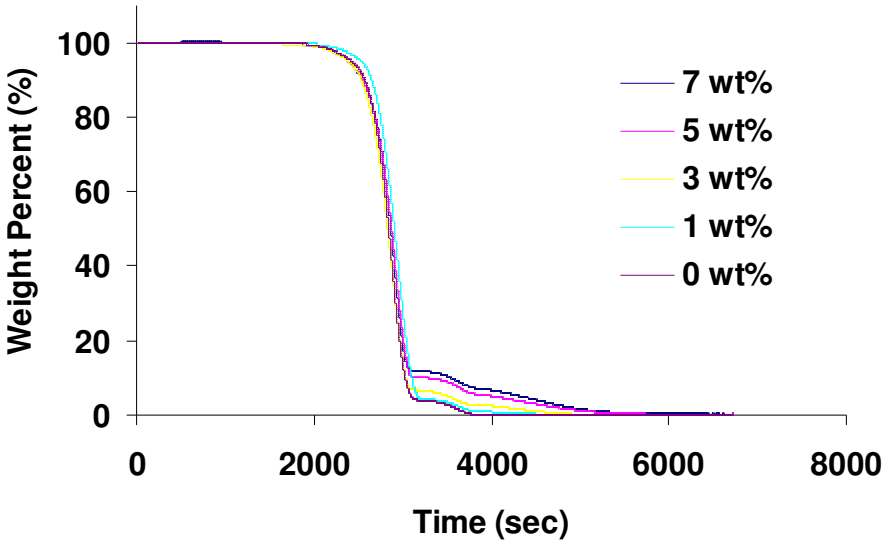
Weight Percent (%)
100
80
60
40
20
0
0
2000
4000
6000
8000
Time (sec)
7 wt%
5 wt%
3 wt%
1 wt%
0 wt%

(a)

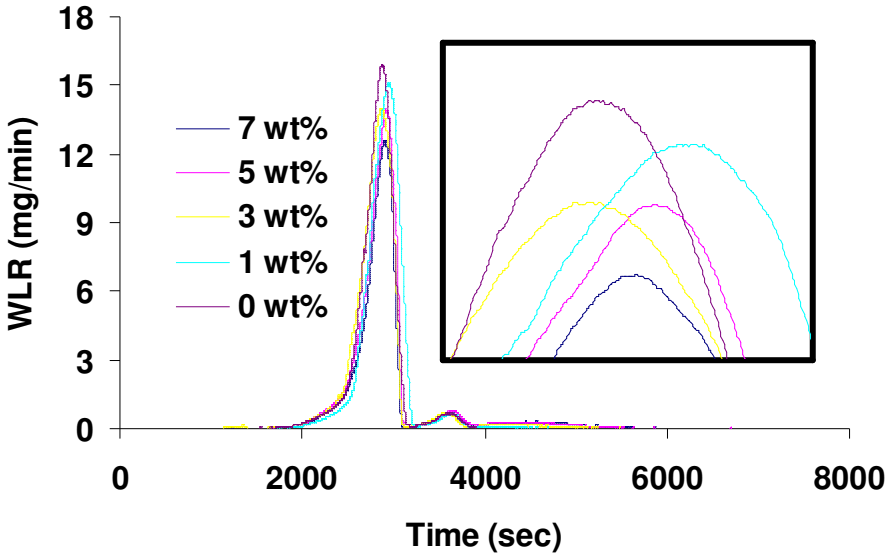
WLR (mg/min)
18
15
12
9
6
3
0
0
2000
4000
6000
8000
Time (sec)
7 wt%
5 wt%
3 wt%
1 wt%
0 wt%

(b)

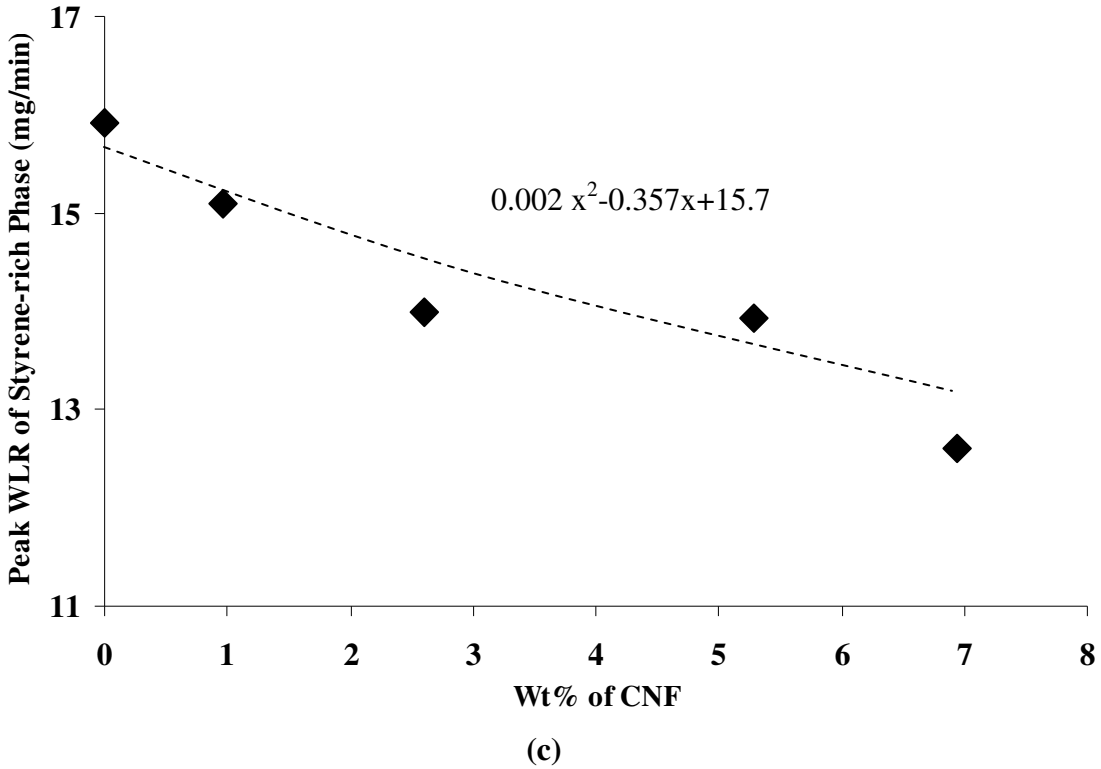

Figure 4.27 (a) Weight percent loss profiles of PS-CNF composites at various CNF loadings. **(b)** WLR profile of the PS-CNF composites at various CNF loadings. The inset shows the peak WLR of the styrene-rich phase. **(c)** The decreasing magnitude of peak WLR of the styrene-rich phase with increasing CNF loading.

In order to understand the effect of processing on the thermo-oxidative behavior of the polymer phase in the composites, the TPWLR corresponding to the styrene-rich phase was compared for the solvent processed, low porosity extruded and high porosity extruded composites. Since there was no significant effect of CNF loading on the TPWLR, the average of all the TPWLR corresponding to the styrene-rich phase at the loadings studied was assumed to be a representation of the processing effects. Figure 4.28 shows the average TPWLR of neat PS and the PS-CNF composites corresponding to the styrene-rich phase as a function of the processing technique. It is evident that the solvent processed composites exhibit the lowest TPWLR, while the low porosity extruded composites exhibit the highest TPWLR. The neat PS results tend to indicate that the

solvents contaminate the PS thereby enhancing its combustion. Thus, an important conclusion can be drawn regarding the effect of processing on the thermal properties of the polymer phase of PS-CNF composites: *extrusion is a slightly more desirable process than solvent processing for enhancing the thermal stability of the polymer phase by avoiding contamination from solvents*. In addition, *the decrease in TPWLR of PS-CNF composites in comparison to neat PS indicates that the presence of CNFs, which are thermally more conductive, tends to enhance the combustion by improving the rates of heat transfer.* Within the TSE process, the removal of porosity through the use of a vacuum pump tends to marginally enhance the thermal stability.

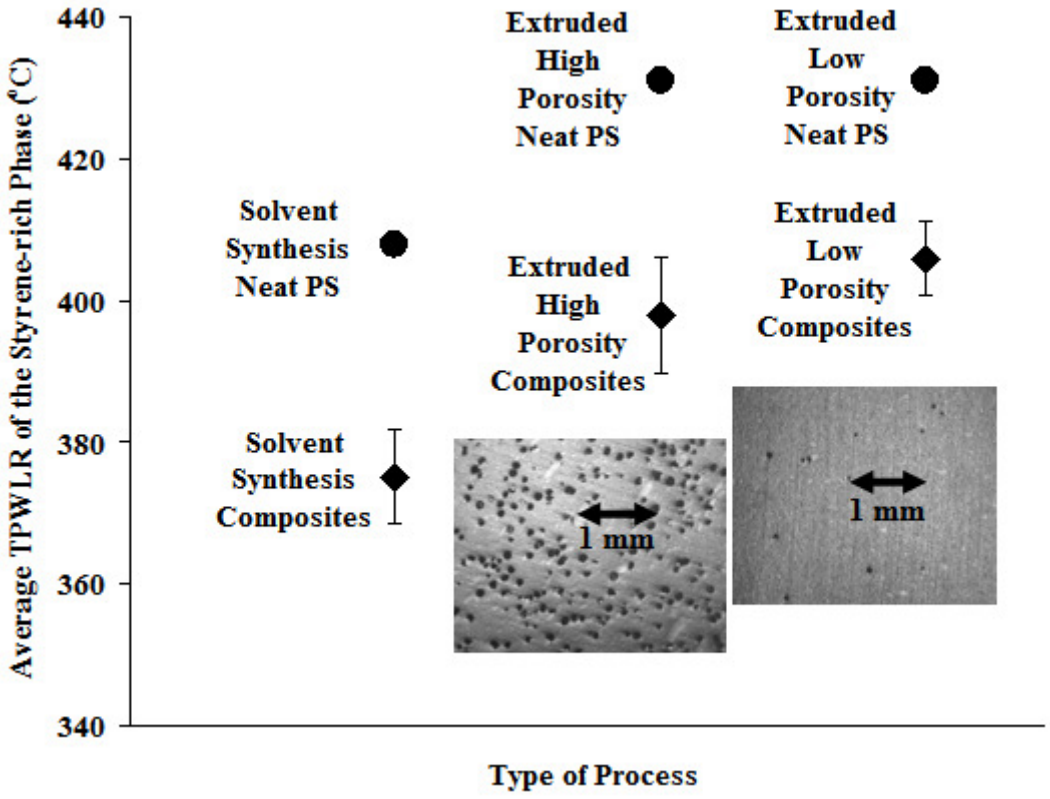

Figure 4.28 Average TPWLR of the styrene-rich phase of the PS-CNF composites processed via different techniques. Both the neat PS and the composites processed via solvent processing exhibit the least thermal stability and the extruded low porosity ones exhibit the highest thermal stability. The inset shows optical micrographs depicting the difference in porosity of the extruded composites.

Further insight into the effects of extrusion processing conditions on the thermo-oxidative behavior of the polymer phase of the composites was obtained by studying the TPWLR of the styrene-rich phase as a function of the extruder screw speed, which corresponds to the magnitude of shear rate (see figure 4.29).

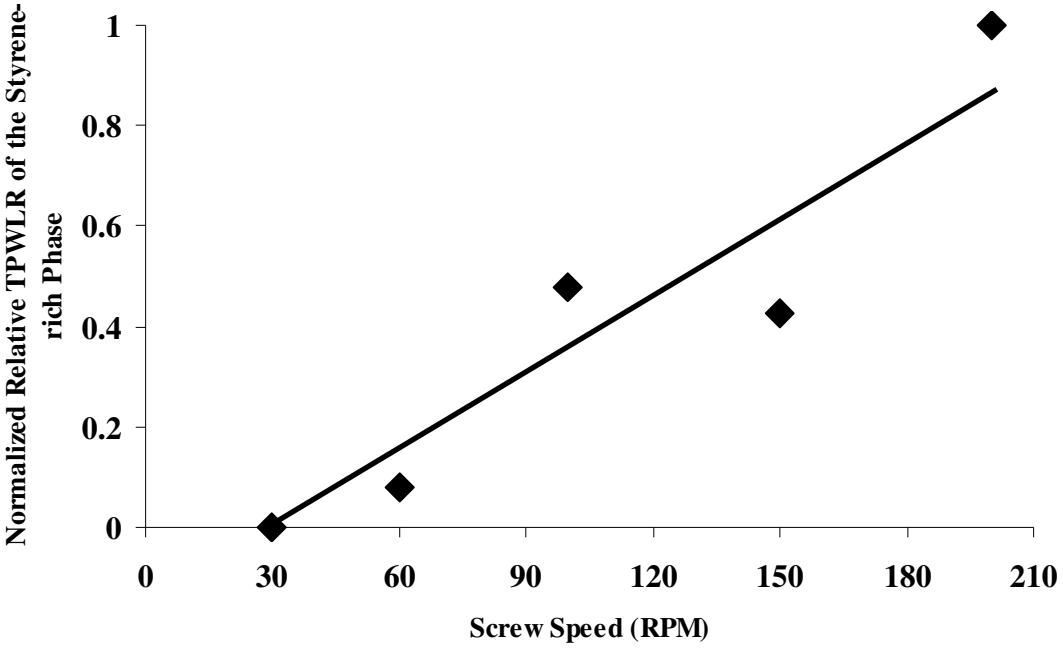

Figure 4.29 Normalized relative TPWLR of the styrene-rich phase as a function of the extrusion screw speed. Note the approximately linear increase in TPWLR with increasing screw speed.

The TPWLR of the styrene-rich phase is normalized to vary between 0 and 1 to identify the qualitative trend clearly. It indicates an approximately linear increase in TPWLR with screw speed. This can be attributed to the increase in agglomerate size at a screw speed of 30 rpm when compared to 200 rpm due to lower shear rates, as discussed in 4.1.5. Thus, an important conclusion can be drawn about the effects of processing on the microstructure of the PS-CNF composite: *increasing the surface area of the agglomerated and dispersed CNFs in the polymer possibly inhibits the initiation of thermal decomposition*. This provides additional evidence that the use of solvents is

affecting the thermal decomposition of PS in a deleterious manner (see figure 4.27) since the dispersion of the CNFs, which is better in solvent processed PS-CNF composites (see figure 4.4), should be enhancing the thermal stability.

In order to investigate the effects of the solvent and extrusion processing on the thermo-oxidative behavior of the CNFs, the normalized weight loss of CNFs in the composites (i.e., the normalized weight loss after the time corresponding to the point of inflection between the second and third peaks of the WLR curve) was studied as a function of time and compared with unmixed ingredients (i.e., unprocessed PS and CNF). Figure 4.30 shows that the CNFs in solvent processed composites decompose at a substantially faster rate than the TSE processed ones. It can also be seen that the CNFs in both processes exhibit a faster decomposition rate relative to the unmixed material. Increasing the degree of shear in the TSE process i.e., changing from a low shear to a high shear screw design (see 3.2.2.2), slightly increases the rate of thermal decomposition. Given that the solvent processed PS-CNF composites show a random dispersion of CNFs (see figure 4.4), the thermo-oxidative behavior of the TSE processed material tends to indicate a microstructure in which the CNFs are better dispersed than the unmixed ingredients, but not dispersed as well as the solvent processed composites. Agglomerations in the extruded composites are clearly evident in the micrographs seen in figure 4.7. Thus, an important conclusion about characterizing the effect of processing on the microstructure of PS-CNF composites can be made: the combination of figures 4.7 and 4.30 indicates that *the TGA measurements can provide insight into the degree of dispersion resulting from the processing of the composites in a manner that is complimentary to conventional microscopy techniques*.

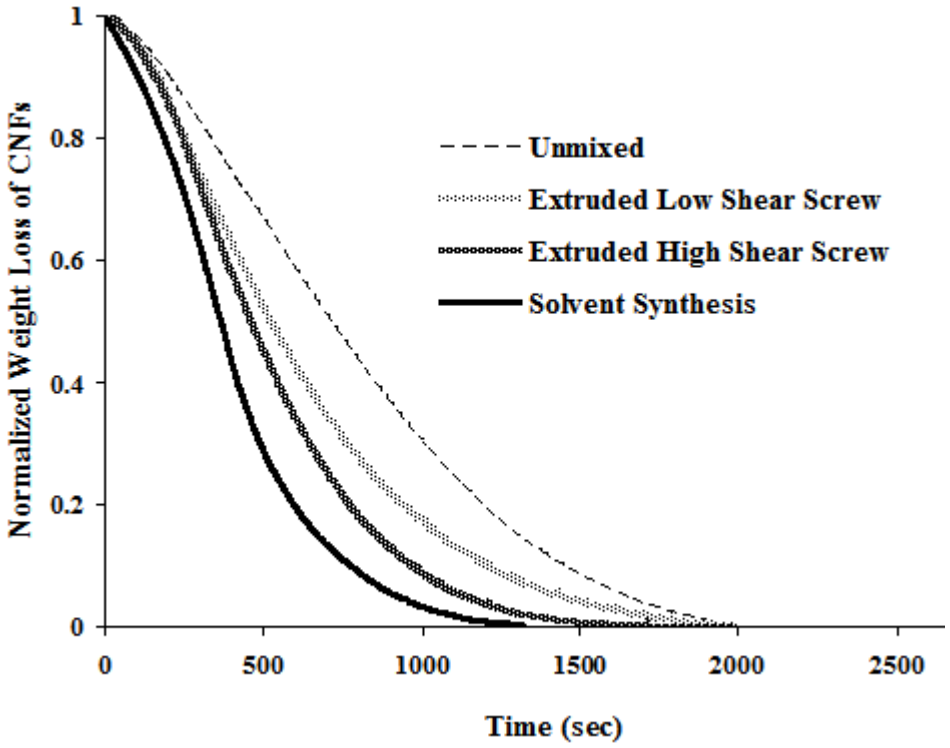

Figure 4.30 Normalized weight loss of CNFs as a function of time for the PS-CNF composites. Note that the rate of weight loss of CNFs increases with increasing levels of shear mixing.

4.2.2.6 Mechanical Properties: Extruded

To further investigate the structure-property and processing-property relationships for extruded PS-CNF composites, the tensile modulus, tensile strength, and % strain to failure of the PS-CNF composites extruded using the high shear screw design (see 3.2.2.2) were measured using the procedure described in 3.4.4. Figure 4.31 shows a representative stress-strain plot of the extruded PS-CNF composites. The stress-strain behavior seen in figure 4.31 is typical of most glassy polymers. Neat PS is a brittle polymer with a less than 1% strain to failure. The presence of polybutadiene in polystyrene results in toughening above the yield strain. The toughening is usually

attributed to the generation and growth of crazes [101]. This explains the higher % strain to failure (~8%) of the PS observed in figure 4.31.

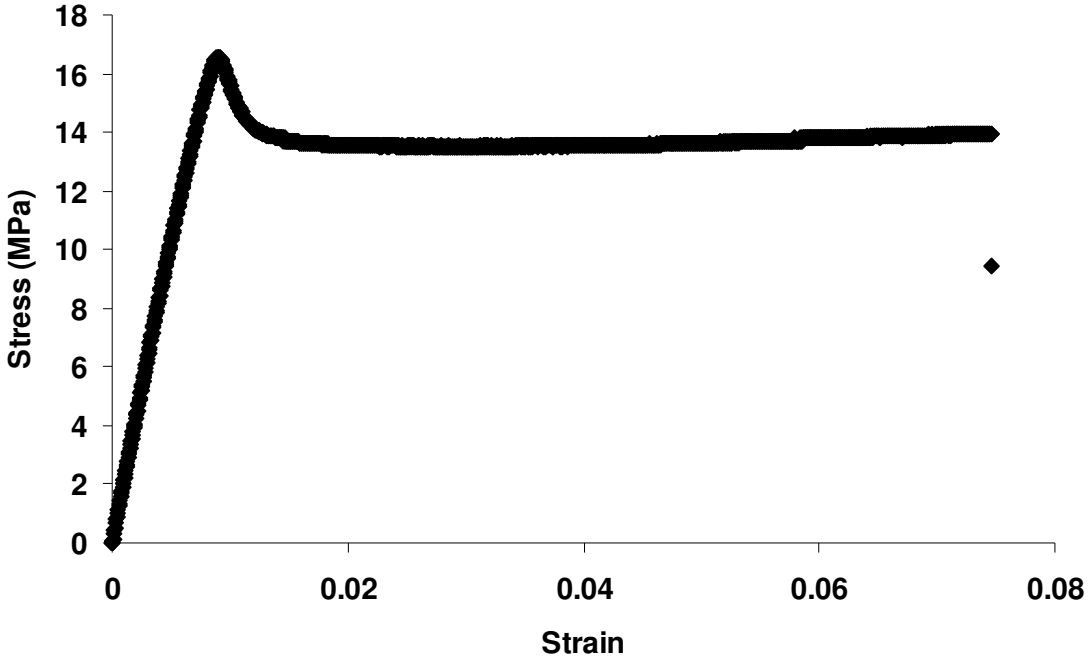

Figure 4.31 A representative stress-strain plot of the extruded PS-CNF composites.

Figure 4.32 shows the tensile modulus, tensile strength and the % strain the failure as functions of CNF loading. The tensile modulus shows a linear increase from 1.9 GPa for the neat PS to 3.1 GPa for the extruded PS-CNF composite with ~10 wt.% CNF loading. The tensile strength shows a linear increase from 16 MPa for the neat PS to 25 MPa for the extruded PS-CNF composite with ~10 wt.% CNF loading. The % strain to failure shows a linear decrease from 12% for the neat PS to 2% for the extruded PS-CNF composite with ~10 wt.% CNF loading. In summary, at 10 wt.% CNF loading, the tensile modulus increased by 62%, tensile strength increased by 54% and % strain to failure decreased by 85% compared to the neat PS. While the increase in tensile modulus and

tensile strength is due to the higher mechanical properties of CNFs, the decrease in % strain to failure is due to the brittle nature of the CNFs.

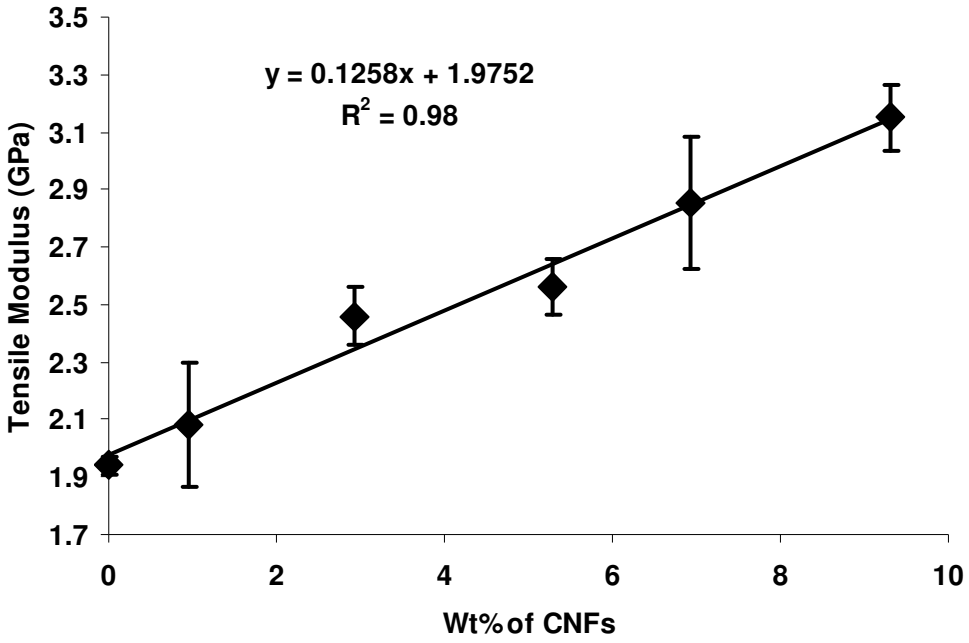

(a)

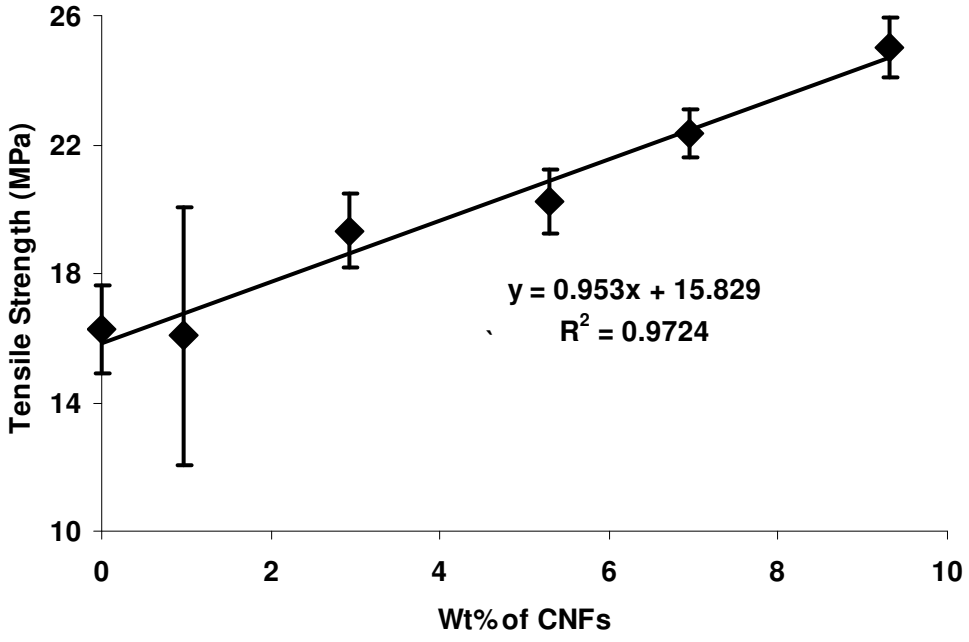

(b)

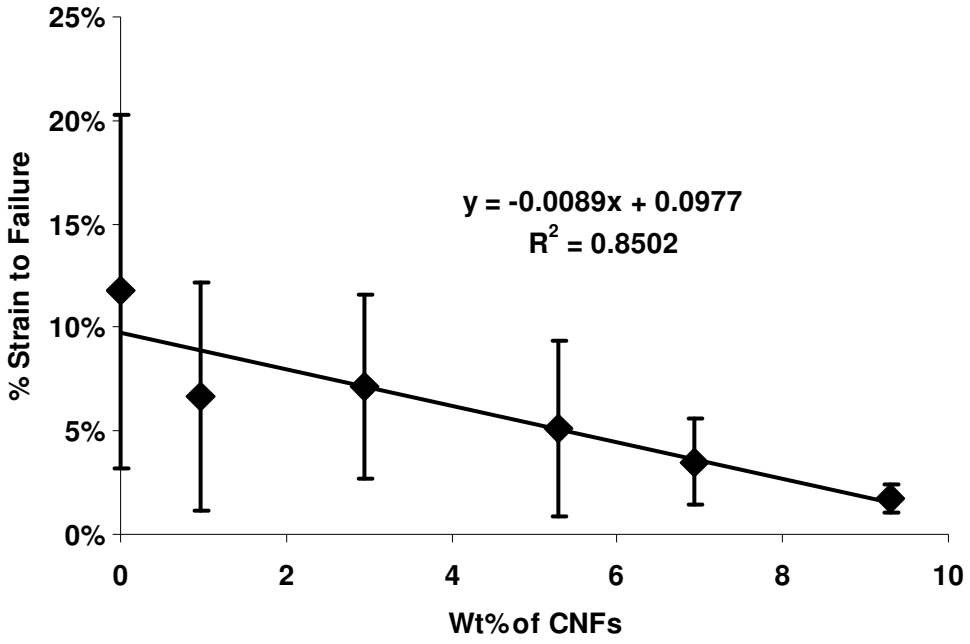

(c)

Figure 4.32 Influence of CNF loading on the **(a)** tensile modulus, **(b)** tensile strength, and **(c)** % strain to failure of the extruded PS-CNF composites.

Figure 4.32a provides an important insight into the reinforcing effects of CNFs on the tensile modulus of extruded PS-CNF composites: by extrapolating the linear trend of the tensile modulus to a 100 wt.% CNF loading, *the limiting tensile modulus for the CNFs was estimated to be ~15 GPa*. This value is similar to other recent investigations [71] into the mechanism of carbon nanomaterials reinforcement in polymer nanocomposites. However, it is significantly lower than the expectations of carbon nanomaterials [102,103]. This discrepancy may be due to the previously discussed agglomerates of CNFs (see 4.1.2 and 4.1.5) that act as masses of 'springs', thereby reducing the effective modulus of the CNFs. Furthermore, the existence of agglomerates could promote crack propagation while preventing the nanocomposites from realizing the full enhancement in mechanical properties.

In addition, the effect of various extrusion processing parameters on the tensile modulus and tensile strength was also studied. Figure 4.33 shows the influence of the type of CNFs – high density (HD) or low density (LD), filler feed port – end or middle, and a vacuum pump (VP) – with or without, on the tensile modulus and tensile strength of extruded PS-CNF composites with 10 wt.% CNF loading, extruded at 200 RPM. It is evident that the LD CNFs result in higher modulus and strength than the HD CNFs. This can be attributed to the higher aspect ratio of LD CNFs when compared to HD CNFs (see 3.1.2.2) that results in higher surface area and hence better load transfer. The choice of filler feed port, which corresponds to the residence time in the extruder, does not indicate any effect on mechanical properties. The increase in residence time in feeding the filler through the end port when compared to the middle port is less than 10 minutes. The results indicate that such a small increase in residence time is not sufficient to improve the mixing significantly. Correspondingly, no appreciable change in the mechanical properties was observed.

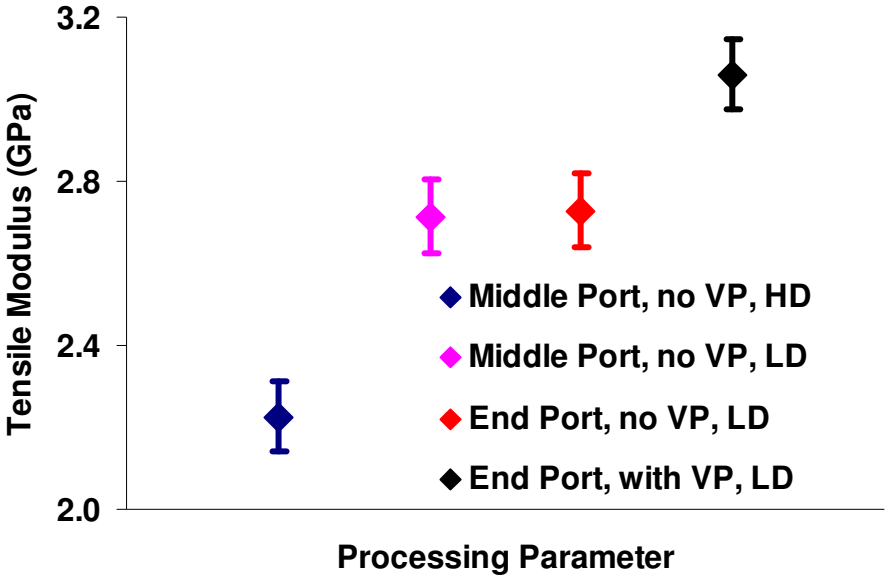

(a)

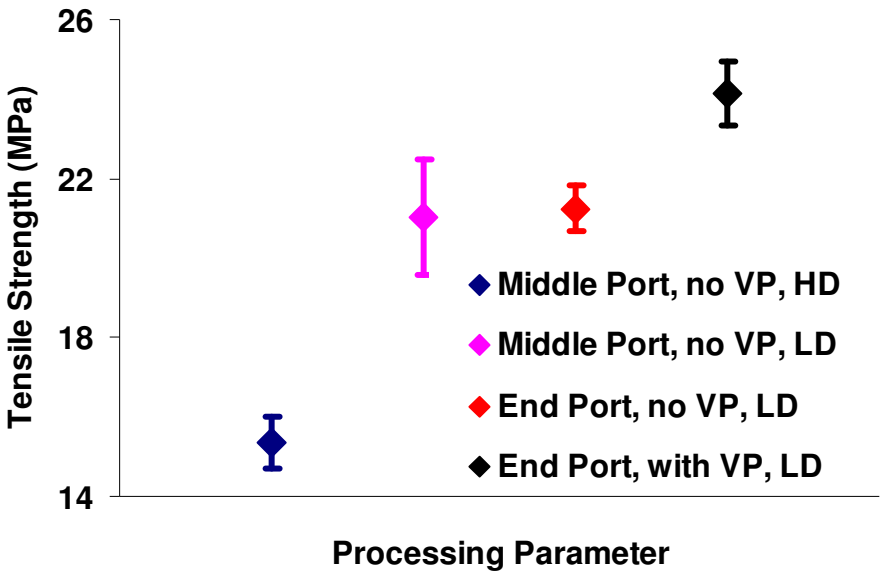

(b)

Figure 4.33 Influence of type of CNFs – high density (HD) or low density (LD), filler feed port – end or middle, and vacuum pump (VP) – with or without, on the **(a)** tensile modulus, and **(b)** tensile strength of PS-CNF composites with 10 wt.% CNF loading, extruded at 200 RPM.

On the other hand, using a vacuum pump in-line further improved the modulus and strength. The vacuum removed the air entrained in the CNFs, thereby reducing the porosity in the composites (see figure 4.8) and increasing the modulus and strength.

Figure 4.34 shows the influence of screw speed and flow rate on the tensile modulus and tensile strength of PS-CNF composites with 10 wt.% CNF loading. Two different flow rates – 1 and 2 lb/hr, and five different screw speeds – 30, 60, 90, 150, 200 RPM were employed. While there was no significant effect of flow rate on the mechanical properties, increasing screw speed, which corresponds to increased magnitude of shear rate, increased the modulus and strength. This is due to the redistribution of higher aspect ratio agglomerates into lower aspect ratio ones, as described in 4.1.5.

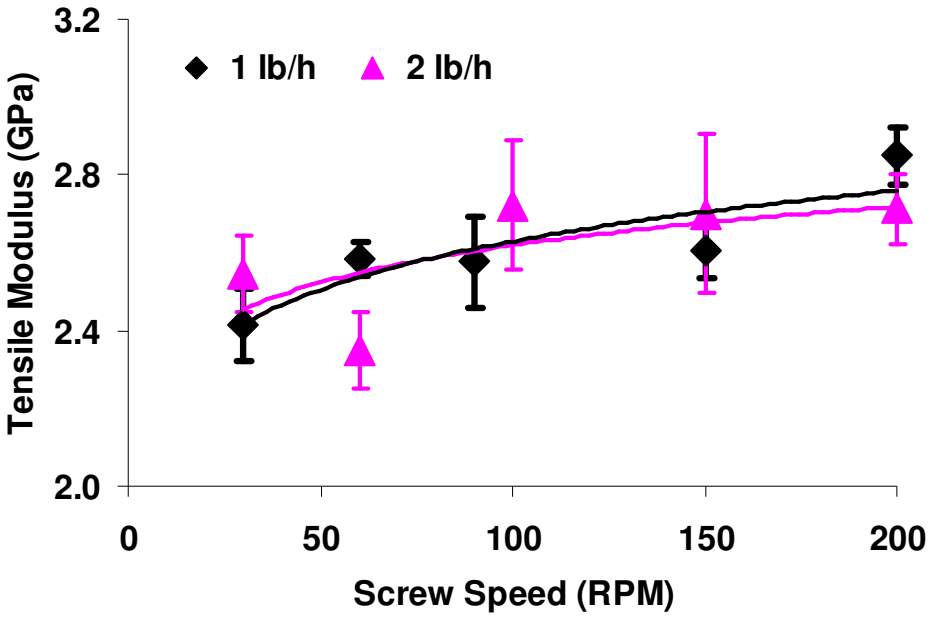

(a)

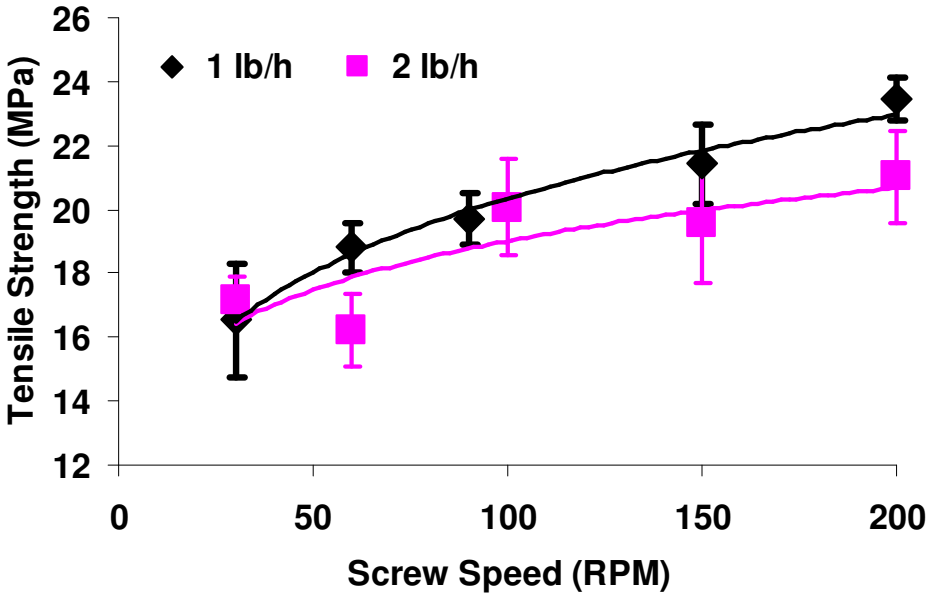

(b)

Figure 4.34 Influence of screw speed and flow rate on the **(a)** tensile modulus, and **(b)** tensile strength of PS-CNF composites with 10 wt.% CNF loading, extruded at 200 rpm. While flow rate does not affect the mechanical properties significantly, both modulus and strength tend to increase with screw speed and begins to asymptotically reach a plateau at higher screw speeds.

From Figure 4.34, a conclusion may be drawn concerning processing-property relationships for extruded PS-CNF composites: *both modulus and strength begin to*

asymptotically reach a plateau value at higher screw speeds indicating that increasing the magnitude of shear rate does not provide a complete solution to obtaining optimal mechanical properties.

4.3 Comparison of Solvent Processing and Extrusion: Summary

With the results described in 4.2.2, it is possible to begin constructing an idea of the differences between solvent processing and extrusion. For the aforementioned physics of the processing effects on the material, the results are qualitatively indicating the following:

Solvent Processing	**TSE**
Characteristics & Mechanism	
• Batch (small quantities)	• Continuous (large quantities)
• Ultrasonic energy couples with agglomerates to cause separation through agitation or bursting of microbubbles through cavitation.	• Breakup of agglomerates at higher shear rates. Possible separation of agglomerates through attrition at low degree of screw channel fills.
• Polymer and filler mixed in a low shear environment after sonication, for a long time, in a less viscous medium.	• Polymer and filler mixed in a high shear environment, in a more viscous medium.
Microstructure	
• Good dispersion on micro and nanoscale resulting in low percolation threshold. Resultant filler aspect ratio is higher. No induced alignment.	• Good distribution on microscale, poor dispersion on nanoscale resulting in high percolation threshold. Resultant filler aspect ratio is lower. Induced alignment.
Properties	
• Higher rheological and electrical properties, but lower thermo-oxidative properties.	• Lower rheological and electrical properties, but higher thermo-oxidative properties.

4.4 Processing – Structure Relationships: A New Combinatorial Approach

The processing-structure relationship in extruded PS-CNF composites has also been examined for establishing a new approach to develop polymer nanocomposites via combinatorial materials science. The new combinatorial approach is a direct outcome of the transient processing conditions of extrusion that permits for a high throughput, continuous method to process PS-CNF composites for rapid structure-property characterization. However, in this research it was essential to establish the relationship between the mixing in extrusion (i.e., processing) and the resulting compositional gradient (i.e., structure).

As described in 2.5.1, although there has been significant research to develop and characterize compositional gradients (CGs), they are either a posteriori techniques [104,105] or limited to low loadings of the filler in the composite [73]. At higher loadings, especially of dark colored fillers, the optical probes tend to reach their saturation, i.e., detection limit. Furthermore, most of the prior works conducted to rapidly determine the CGs require a pre-calibration of the technique with known composition, thereby decoupling the processing from the evolution of the structure. In order to address these issues, a non-destructive approach, based on the residence distribution (see 3.3.2) representing the mixing in the extrusion process was adopted. The nature of the approach allows rapid characterization of the CG compared to a time-consuming and destructive approach such as thermogravimetric analysis.

4.4.1 Prediction of the Compositional Gradient

In general, the response $y(t)$, from a linear, continuous, time-invariant system described by $\Phi(t)$ with input signal, $u(t)$, can be predicted using the *convolution integral* [106]:

$$y(t) = \int_0^t \Phi(t-\tau)u(\tau)d\tau \tag{4.12}$$

In the extrusion context, equation (4.12) can be transformed into the volume domain as,

$$C(v) = \int_0^\infty \hat{\bar{g}}(v-v')\,H(v')\,dv' \tag{4.13}$$

where, $\hat{\bar{g}}(v)$ is a characteristic of the process that is independent of processing conditions, $H(v)$ is the Heaviside function representing the step input of the filler and $C(v)$ is the response to the step input of the filler, i.e., the CG, assuming that the melt absorbance is linearly proportional to composition of the filler. This assumption is valid at low compositions of the filler where Rayleigh static light scattering principles predict that the scattered intensity of light scales linearly with number of particles [107,108], i.e., composition of the filler.

In order to establish the processing-structure relationship and predict the CG, the characteristic of the process that is independent of the processing conditions has to be identified. As described in 2.5.2, leveraging the efforts of Elkouss et al [76], the master curve ($\hat{\bar{g}}(v)$) obtained by modeling the normalized residence volume distributions (RVDs) can be used as a characteristic of the process in equation (4.13) to obtain the CG. The normalized RVDs, obtained experimentally using the in situ optical probe (see 3.3.2), can be modeled in various ways [109-113] to obtain the master curve ($\hat{\bar{g}}(v)$).

Without loss of generality, the applicability of the approach can be demonstrated by modeling the normalized RVDs using simple empirical equations based on transfer functions that represent a series of perfect batch mixers [114,115]. A second order transfer function that corresponds to the mixing occurring in the screw and the die zones of the extruder was used. In the Laplace domain, it can be represented as,

$$G(s) = \frac{a^2 e^{-v_d s}}{(s+a)^2} \qquad (4.14)$$

where, v_d is the delay volume and a is the shape factor. The inverse transform gives the model in the volume domain as,

$$g(v) = a^2 (v - v_d) e^{-a(v-v_d)} \qquad (4.15)$$

Figure 4.35 shows a representative normalized RVD that was obtained experimentally and the curve obtained by modeling it with the normalized form of equation (4.15), as shown in equation (2.3). The peak of the experimental curve is slightly lower than that of the modeled curve because the absorbance of the optical probe reached its saturation i.e., detection limit. The same argument explains why the peak was flatter than what would be expected. This is especially true with dark fillers such as CNFs and CNTs. This phenomenon was not observed in an earlier work using the same experimental setup with bright fillers [104,105].

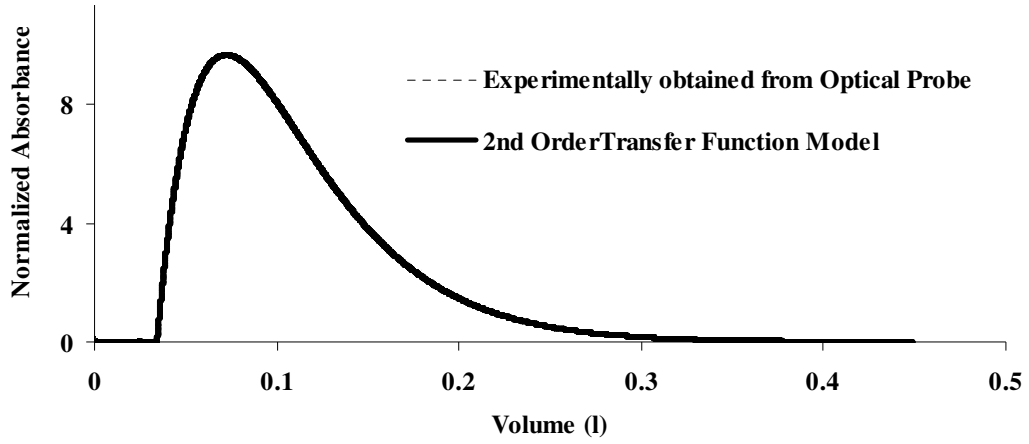

Figure 4.35 Modeling the normalized RVD using a second order transfer function. The peak of the experimental curve is slightly lower than that of the modeled curve because the optical probe measuring the absorbance reached its detection limit.

In addition, to leverage the earlier efforts by Elkouss et al [76], the absence of predominant elastic effects has to be verified. It was done by experimentally obtaining the normalized RVDs for the PS-CNF composites at varying polymer flow rates and extruder screw speeds for a fixed screw design. These normalized RVDs were modeled as described above and it was observed that all the curves superimposed within reasonable error as shown in figure 4.36.

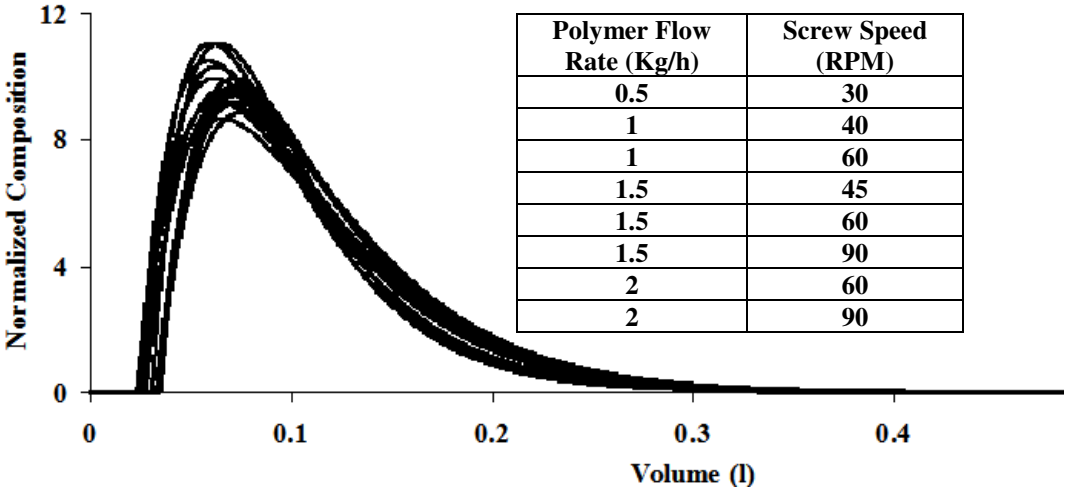

Polymer Flow Rate (Kg/h)	Screw Speed (RPM)
0.5	30
1	40
1	60
1.5	45
1.5	60
1.5	90
2	60
2	90

Figure 4.36 The modeled normalized RVDs resulting from varying polymer flow rates and extruder screw speeds superimposed within reasonable error .

For the resulting master curve ($\hat{\bar{g}}(v)$) of PS-CNF composites, $v_d = 0.052\, l$ and $a = 30\, l^{-1}$. Using equation (4.13), the convolution of $\hat{\bar{g}}(v)$ with a Heaviside step function of magnitude *k,* predicts the CG as,

$$C(v) = k \int_0^v \hat{\bar{g}}(v)\, dv \tag{4.16}$$

Figure 4.37 compares the CG of PS-CNF composites ranging from an initial volume fraction of 0 to a final volume fraction of 0.06 i.e., $k = 6$, experimentally characterized using a TGA, with that theoretically predicted by equation (4.16). The weight fraction characterized by the TGA was converted to volume fraction using equation (4.2).

An important conclusion can be drawn from figure 4.37 about the characterization of processing-structure relationships for extruded PS-CNF composites: *the experimental measurements correlate well with those predicted by convolution thereby validating the non-destructive approach.* This approach has significant implications in combinatorial techniques utilizing CGs. It allows rapid characterization of the CGs when compared to the time consuming and destructive tests like thermogravimetric analysis. With this approach, the amount of filler that is needed to achieve a CG containing all volume fractions between 0 and 0.06 was only 15 g, which was achieved by operating the PS feeder steadily at a rate of 2 lb/hr and the CNF feeder at 0.2 lb/hr for 10 minutes. Extending the operation of the CNF feeder beyond this time resulted in steady-state production of the PS-CNF composites with a volume fraction of 0.06 at a rate of 0.016 l/min.

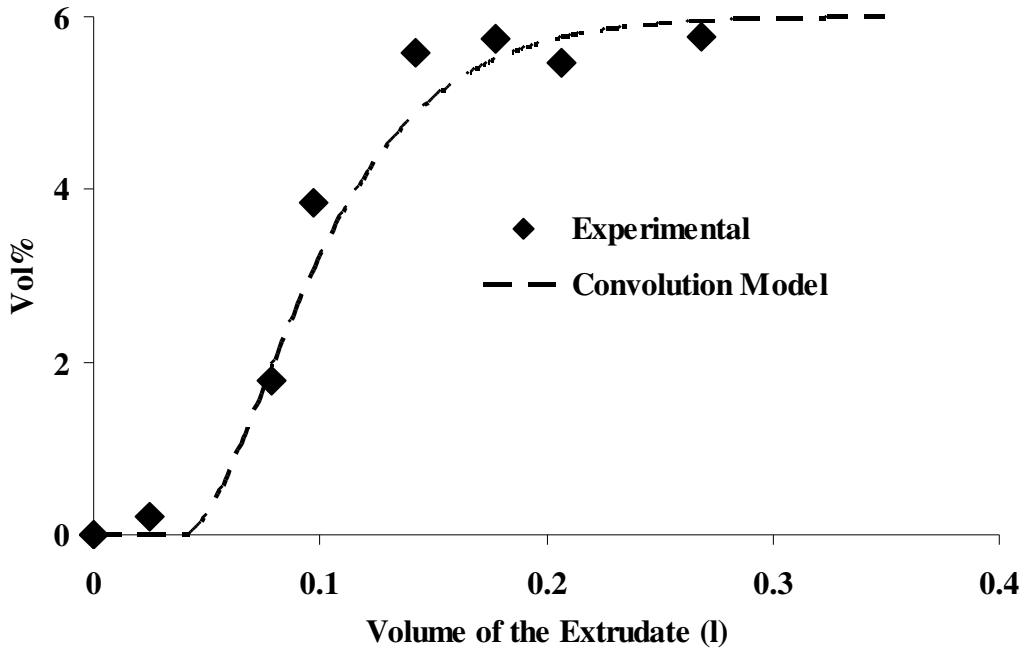

Figure 4.37 The compositional gradient predicted via convolution correlates well with the experimental values obtained from thermogravimetric analysis for the PS-CNF composite. This confirms the validity of the non-destructive approach.

4.4.2 CG Characterization Approach: Influence of Filler Size

Due to the expensive nature of nanoscale ingredients, it is desirable to apply the CG characterization approach to inexpensive microscale ingredients, such as bright colored KCl, and assess their suitability as 'dummy' fillers. Figure 4.38 compares the CG of PS-KCl composites ranging from an initial volume fraction of 0 to a final volume fraction of 0.18 i.e., $k = 18$, experimentally characterized using a TGA, with that predicted by equation (4.16). Here, it must be noted that the master curve ($\hat{\bar{g}}(v)$) used in equation (4.16) was that obtained from modeling the normalized RVDs for the PS-CNF composites. In spite of that the experimental results correlated well with those predicted by convolution. Thus it can be concluded that the size scale of the fillers tested does not affect the evolution of CGs, thereby indicating that the transient effects of the mixing

process are independent of the size of the filler. This would imply that the normalized RVD resulting from the microscale and nanoscale filler is the same. Therefore the following conclusion can be drawn about the influence of the size scale of ingredients on the processing-structure relationships: *inexpensive microscale ingredients can be used to conduct impulse or step experiments to verify the absence of predominant elastic effects and to establish appropriate processing conditions for obtaining desired CGs instead of using more expensive nanoscale ingredients*.

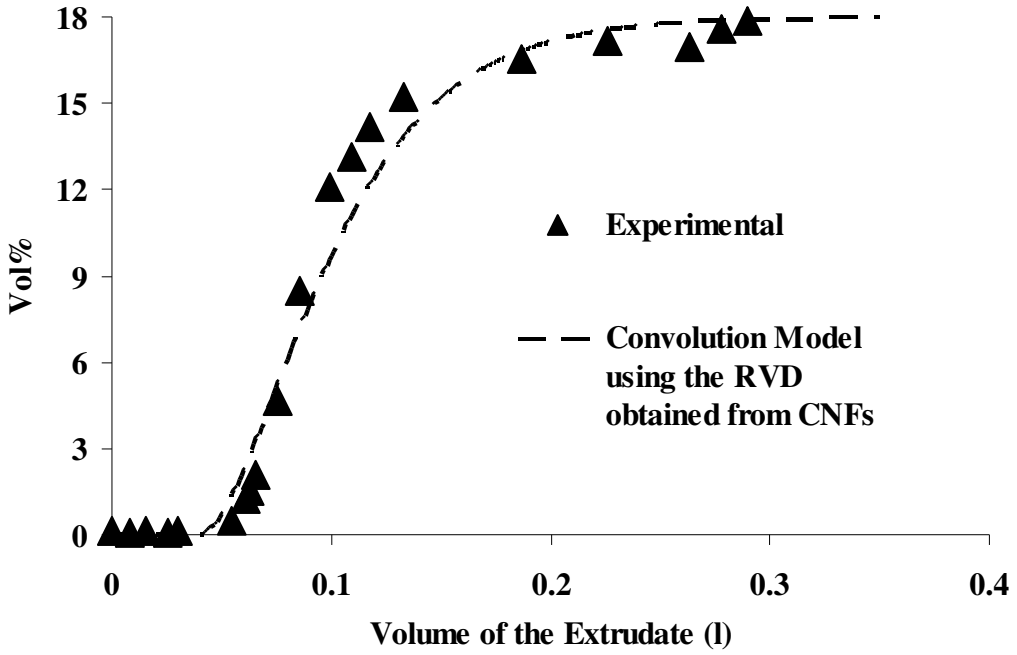

Figure 4.38 The compositional gradient predicted via convolution correlates well with the experimental values obtained from thermogravimetric analysis for the PS-KCl composite. This indicates that the approach is independent of the size scale of the fillers.

5. Conclusions and Future Work

Although a significant amount of research has been conducted to establish the structure-property relationships of polymer-CNT/CNF composites, there have been very few efforts to address the effect of processing on the structure-property relationships. In order to address this issue, this work focused on comparing the processing-microstructure and structure-property relationships of PS-MWCNT and PS-CNF composites produced via solvent processing and twin screw extrusion. The processing-property relationships were also investigated for the extruded composites. In addition to batch processing, a combinatorial approach to establishing the processing-structure-property relationships of PS-CNF composites was demonstrated.

The research issues addressed in this work answered several fundamental questions related to developing polymer nanocomposites with enhanced material properties. They resulted in advancing the understanding of the influence of the type of process and processing parameters on the electrical, rheological, thermo-oxidative and mechanical properties of the PS-MWCNT and PS-CNF composites. This helps in engineering the properties and performance of these composites by appropriate choice of the type of process and the processing parameters. The microstructural characterization led to a better understanding of how the properties of the PS-MWCNT and PS-CNF composites evolved as a function of distribution of the agglomerates, and dispersion, alignment and aspect ratio of the filler. The non-destructive approach based on the convolution of process models to predict the compositional gradients allowed for more rapid characterization of processing-structure relationships in polymer nanocomposites developed via a combinatorial approach.

5.1 Intellectual Contributions

Through this research effort, the following specific intellectual contributions were made that directly affect the development and characterization of polymer nanocomposites:

- **New methodology to quantify the limiting rheological properties of percolated nanostructures [116]:** In all the works reported to date, the increase in electrical conductivity and rheological parameters of polymer-CNF/MWCNT composites were each reported or modeled independently as a function of the particle percolation. There have been no reports of a physical and quantitative relationship between the increase in electrical conductivity and the rheological parameters, both of which fundamentally depend on the extent of particle percolation. In order to address this issue, an interpenetrating phase polymer nanocomposite formed by percolation of MWCNTs in PS-MWCNT composites was quantitatively characterized. This was accomplished by treating the PS-MWCNT composite as a combination of two phases: a continuous PS phase reinforced by non-interacting MWCNTs, and a continuous phase consisting of the pseudo-solid like network of percolated MWCNTs. The distribution of MWCNTS among the continuous phases was determined from the degree of percolation of MWCNTs correlated to power-law fits of the electrical conductivity with and without a percolation threshold. Subsequently, the dynamic rheological properties (the storage modulus and loss modulus) of the PS-MWCNT composites were interpreted as a function of the degree of percolation, in addition to the concentration of MWCNTs and frequency using a modified Nielsen's model. This methodology, for the first time, allows the determination of limiting rheological

properties of the pseudo-solid like network of percolated MWCNTs. Simultaneously, it was possible to isolate the effect of non-interacting MWCNTs reinforcing the PS from the percolated MWCNTs. Hence, this methodology has important implications in quantifying the properties of percolated nanostructures not only in polymer nanocomposites, but also in self-assembly, tissue fixation etc.

- **Novel approach to assess the degree of dispersion using thermogravimetric analysis [117]:** Traditionally thermogravimetric analysis was used to study the composition of composite systems, identify the purity of fillers, and to establish the thermal and thermo-oxidative behavior of polymer nanocomposites. In this work, the normalized thermo-oxidative decomposition of the CNFs resulting from different processes (solvent processing and twin screw extrusion) and processing conditions (high and low shear screw design) was studied in detail. It was observed that the normalized thermo-oxidative decomposition of the CNFs correlated well with the qualitative degree of dispersion of the CNFs obtained from scanning electron microscopy. Hence, a novel thermogravimetric analysis-based approach was demonstrated that can characterize the degree of dispersion of the filler in composites that complements conventional microscopy techniques. This approach has three significant advantages over conventional microscopy techniques: (1) it does not require a contrast difference between the filler and the matrix, (2) it is not limited to probing small areas at a time and gives a bulk measurement of the degree of dispersion, and (3) it is more quantitative.

- **Novel approach to rapidly and non-destructively characterize compositional gradients resulting from transient extrusion [118]:** In the past few years there has been an increased interest in rapidly characterizing the composition and properties of composites with CGs resulting from transient extrusion. However, the current state-of-art characterization techniques for determining the composition in compositional gradients are either a posteriori techniques or limited to low loadings of the filler in the composites. Furthermore, most of the prior works conducted to rapidly determine the CGs require a pre-calibration of the technique with known composition, thereby decoupling the processing from the evolution of the structure. In this work a novel convolution approach based on normalized residence volume distributions was developed and demonstrated to overcome the above drawbacks. The nature of the approach allows rapid characterization of the CG compared to a time-consuming and destructive approach such as thermogravimetric analysis. Since the approach does not decouple processing from the evolution of the structure, it can be used to precisely estimate the quantity of expensive nanoscale fillers required to produce the compositional gradient, before conducting the experiments. Furthermore, it was also shown that the approach is independent of the size scale of the filler. Hence, inexpensive microscale fillers can be used instead of more expensive nanoscale fillers to conduct experiments to establish the appropriate processing conditions for obtaining desired compositional gradients.
- **Advanced understanding of mechanical property enhancement in polymer nanocomposites and associated limitations:** In this work, the effect of CNF composition and extrusion processing parameters on the tensile strength and tensile

modulus of the polymer nanocomposites has been thoroughly investigated. Although increasing the composition of CNFs increases the mechanical properties of the composites, similar enhancements at higher concentrations (more than ~10 wt.%) have also been demonstrated by using less expensive carbon microfibers. Thus, the effectiveness of using CNFs is limited to lower concentrations (less than ~10 wt.%). Furthermore, at lower concentrations, it was observed that increasing the extrusion shear rate leads to an asymptotic plateau in mechanical properties. At higher shear rates, microscopy showed that the CNFs deagglomerate, but also suffer from a reduction in aspect ratio, thereby losing their effectiveness to enhance the mechanical properties. Since deagglomeration is a function of both the magnitude of shear rate and the residence time, it is desirable to use a lower shear rate and an extended residence time in order to retain the aspect ratio of CNFs, thereby increasing their effectiveness to reinforce the polymer matrix. As evidenced by microscopy in this work, further improvement of the mechanical properties of polymer nanocomposites is possible by improving the interfacial adhesion. In summary, the insights discussed above advance the understanding of how to better enhance the mechanical properties of polymer nanocomposites.

- **Improved selection of the process to obtain the desired properties [117,119,120]:** In this work, the influence of different processes on the electrical, rheological and thermo-oxidative properties of polymer nanocomposites was studied. The following conclusions were drawn to improve the selection of the type of process that can be used to obtain the desired properties: (1) Flow induced shear stresses in the die during extrusion align the nanoscale fillers and reduce the electrical conductivity. Upon

annealing the extruded composites, the aligned nanoscale fillers are relaxed and regain their interconnectivity, and hence the electrical conductivity of composite is improved. Thus, in order to obtain better electrical conductivity of polymer nanocomposites, a combination of extrusion and annealing is desirable. (2) Solvent processing is more desirable to obtain better rheological properties than the extruded ones because of the lower reduction in aspect ratio of the nanoscale fillers in solvent processing when compared to extrusion. (3) Extrusion is more desirable to obtain better thermal stability of the composites when compared to solvent processing because the absence contamination of from solvents. (4) As long as the nanoscale fillers can be dispersed randomly, the choice of solvent does not have a significant affect on the electrical and rheological properties of the polymer nanocomposites.

5.2 Future Work

During the course of this research investigation, some interesting research issues have been uncovered that affect the development of polymer nanocomposites needing further investigation. The following is a list of these issues:

1. *Characterize the mechanical properties of the extruded polymer nanocomposites in both axial and transverse directions.* This will provide a better understanding of the nanoscale filler alignment on the mechanical properties of the polymer nanocomposites.
2. *Characterize the molecular weight and crystallinity of the polymer as a function of the type of process and processing parameters*. This will provide insight to decouple

the affect of filler loading from the changes in the properties of the polymer phase itself.

3. *Process composites with varying residence time and magnitude of shear rate*. Since it has been concluded in this work that deagglomeration is a strong function of both the residence time and the magnitude of shear rate, it would be appropriate to find the critical combination of the two parameters that would lead to optimal material properties. While the residence time can be varied by modifying the screw design, the magnitude of shear rate can be varied by modifying the screw speed.
4. *Process and characterize the properties of hierarchically structured composites for multifunctionality*. In the present work, the composites were made using only one filler to enhance the properties. By studying multi-component and multi-scale systems, significant enhancement in more than one property, for example, both electrical and mechanical properties, can be achieved to address multifunctionality.
5. *Tailor the expanse of the compositional gradient by varying the screw design*. Although the entire treatment of the combinatorial approach developed in this work assumes a fixed screw design, it is not difficult to extend it to varying screw designs. Assuming the absence of predominant elastic effects, every new screw design tested requires only a single impulse experiment to experimentally obtain the normalized residence volume distribution that can be modeled to obtain the master curve. Subsequently, the compositional gradient for the new screw design can be predicted by using equation.
6. *Process and characterize polymer-CNF composites with other polymer systems*. Polymers, such as Nylon, are qualified for different applications than PS. They may

also offer better interfacial adhesion between the polymer matrix and the CNFs resulting in better mechanical properties.

7. *Process and characterize composites of polymers with CNFs functionalized both at the ends and the sidewalls*. While the end functionalization can be utilized to cross-link the CNFs with another, thereby creating a continuous fiber-like structure, the sidewall functionalization can be used to improve the adhesion to the polymer matrix. This could potentially result in ultrastrong nanocomposites that can be deployed in space flight applications.
8. *Characterization of diseased tissues in histopathological specimens*: The new technique for characterizing limiting properties in polymer nanocomposites can be extended to histopathology by investigating a new approach to characterizing the degree of percolation for networks of non-conductive diseased tissues, such as confocal microscopy techniques, that would replace the electrical conductivity measurements. The concentration of diseased cells would also need to be calibrated against the level of mechanical degradation in the percolated network of diseased cells and the isolated diseased cells that are quantified using the new technique.

References

1. Bhushan, B. (Ed.), *Handbook of Nanotechnology*, Springer-Verlag, Berlin, Germany (2004).
2. Daenen, M., de Fouw, R. D., Hammers, B., Janssen, P. G. A., Schouteden, K., Veld, M. A. J., *The Wondrous World of Carbon Nanotubes: A Review of Current Nanotube Technologies*, Eindhoven University of Technology, Eindhoven, Netherlands (2003).
3. Ajayan, P. M., *Chemical Reviews* 99, p. 1787 (1999).
4. Sandler, J., Shaffer, M.S.P., Prasse, T., Bauhofer, W., Schulte, K., Windle, A.H., *Polymer* 40, p. 5967 (1999).
5. Lozano, K., *JOM Journal* 52, p. 34 (2000).
6. Andrews, R., Jacques, D., Minot, M., Rantell, T., *Macromolecular Materials and Engineering* 287, p. 395 (2002).
7. Kearns, J. C., Shambaugh, R. L., *Journal of Applied Polymer Science* 86, p. 2079 (2002).
8. Mulhaupt, R., Schall, N., *Kunststoffe* 91, p. 178 (2001).
9. Ferguson, D. W., Bryant, E. W. S., Fowler, H. C., *Proceedings of SPE ANTEC*, p. 1219 (1998).
10. Du, F., Fischer, J. E., Winey, K. I., *Journal of Polymer Science B: Polymer Physics* 41, p .3333 (2003).
11. De la Chapelle, M. L., Stephan, C., Nguyen, T. P., Lefrant, S., Journet, C., Bernier, P., Munoz, E., Benito, A., Maser, W. K., Martinez, M. T., De la Fuente, G. F., Guillard, T., Flamant, G., Alvarez, L., Laplaze, D., *Synthetic Metals* 103, p. 2510 (1999).
12. Benoit, J. M., Corraze, B., Lefrant, S., Blau, W. J., Bernier, P., Chauvet, O., *Syntheric Metals* 121, p. 1215 (2001).
13. M. J. Biercuk, M. C. Llaguno, M. Radosavljevic, J. K. Hyun, A. T. Johnson, and J. E. Fischer, *Applied Physics Letters* 80, p. 2767 (2002).
14. Safadi, B., Andrews, R., Grulke, E. A., *Journal of Applied Polymer Science* 84, p. 2660 (2002).
15. Watts, P. C. P., Hsu, W. K. , Chen, G. Z., Fray, D. J., Kroto, H. W., Walton, D. R. M., *Journal of Materials Chemistry* 11, p. 2482 (2001).
16. Shaffer, M. S. P., Windle, A. H., *Advanced Materials* 11, p. 937 (1999).
17. Qian, D., Dickey, E.C., Andrews, R., Rantell, T., *Applied Physics Letters* 76, p. 2868 (2000).
18. Yang, Y. L., Gupta, M. C., Dudley, K. L., Lawrence, R. W., *Nanotechnology* 15, p. 1545 (2004).
19. Zhang, B., Fu, R. W., Zhang, M. Q., Dong, X. M., Wang, L. C., Pittman, C. U., *Materials Research Bulletin* 41, p. 553 (2006).
20. Sennett, M., Welsh, E., Wright, J. B., Li, W. Z., Wen, J. G., Ren, Z. F., *Applied Physics A - Materials Science and Processing* 76, p. 111 (2003).
21. Potschke, P., Abdel-Goad, M., Alig, I., Dudkin, S., Lellinger, D., *Polymer* 45, p. 8863 (2004).
22. Mahfuz, H., Adnan, A., Rangari, V. K., Hasan, M. M., Jeelani, S., Wright, W. J., DeTeresa, S. J., *Applied Physics Letters* 88, p. 083119-1 (2006).

23. Kashiwagi, T., Grulke, E., Hilding, J., Harris, R., Awad, W., Douglas, J., *Macromolecular Rapid Communications* 23, p. 761 (2002).
24. Kumar, S., Doshi, H., Srinivasarao, M., Park, J. O., Schiraldi, D. A., *Polymer* 43, p. 1701 (2002).
25. Tang, B. Z., Xu, H. Y., *Macromolecules* 32, p. 2569 (1999).
26. Fan, J. H., Wan, M. X., Zhu, D. B., Chang, B. H., Pan, Z. W., Xie, S. S., *Journal of Applied Polymer Science* 74, p. 2605 (1999).
27. Xie, X. L., Zhou, X. P., Tang, J., Hu, H. C., Wu, H. B., Zhang, J. W., *China Synthetic Rubber Industry* 25, p. 46 (2002).
28. Jin, Z. X., Pramoda, K. P., Goh, S. H., Xu, G. Q., *Materials Research Bulletin* 37, p.271 (2002).
29. Gong, X. Y., Liu, J., Baskaran, S., Voise, R. D., Young, J. S., *Chemistry of Materials* 12, p. 1049 (2000).
30. Haggenmueller, R., Gommans, H. H., Rinzler, A. G., Fischer, J. E., Winey, K. I., *Chemical Physics Letters* 330, p. 219 (2000).
31. Sandler, J., Windle, A. H., Werner, P., Altstadt, V., Es, M. V., Shaffer, M. S. P., *Journal of Materials Science* 38, p. 2135 (2003).
32. Potschke, P., Fornes, T. D., Paul, D. R., *Polymer* 43 p. 3247 (2002).
33. Potschke, P., Dudkin, S. M., Alig, I., *Polymer* 44, p. 5023 (2003).
34. Meincke, O., Kaempfer, D., Weickmann, H., Friedrich, C., Vathauer, M., Warth, H., *Polymer* 45, p. 739 (2004).
35. Jin, Z., Pramoda, K. P., Xu, G., Goh, S. H., *Chemical Physics Letters* 337, p. 43 (2001).
36. Thostenson, E. T., Chou. T. W, *Journal of Physics D: Applied Physics* 35, p. 77 (2002).
37. Sandler, J. K. W., Pegel, S., Cadek, M., Gojny, F., van Es, M., Lohmar, J., Blau, W. J., Schulte, K., Windle, A. H., Shaffer, M. S. P., *Polymer* 45, p. 2001 (2004).
38. Tibbetts, G. G., McHugh, J. J., *Journal of Materials Research* 14, p. 2871 (1999).
39. Kuriger, R. J., Alam, M. K., Anderson, D. P., Jacobsen, R. L., *Composites A: Applied Science and Manufacturing* 33(1) (2002), 53–62.
40. Sandler, J., Werner, P., Shaffer, M. S. P., Demchuk, V., Altstadt, V., Windle, A. H., *Composites A: Applied Science and Manufacturing* 33, p. 1033 (2002).
41. Potschke, P., Brunig, H., Janke, A., Fischer, D., Jehnichen, D., *Polymer* 46, p. 10355 (2005).
42. Jin, L., Bower, C., Zhou, O., *Applied Physics Letters* 73, p. 1197 (1998).
43. Bower, C., Rosen, R., Han, R., Zhou O., *Applied Physics Letters* 74, p. 3317 (1999).
44. Kimura, T., Ago, H., Tobita, M., Ohshima, S., Kyotani, M., Yumura, M., *Advanced Materials* 14, p. 1380 (2003).
45. Bai, J. B., Allaoui, A, *Composites A: Applied Science and Manufacturing* 34A, p. 689 (2003).
46. Bryning, M. B., Islam, M. F., Kikkawa, J. M., Yodh, A. G., *Advanced Materials* 17, p. 1186 (2005).
47. Du, F., Fischer, J. E., Winey, K. I., *Physical Review B: Condensed Matter* 72, p. 121404/1 (2005).

48. Ramasubramaniam, R., Chen, J., Liu, H., *Applied Physics Letters* 83, p. 2928 (2003).
49. Lozano, K., Bonilla Rios, J., Barrera, E. V., *Journal of Applied Polymer Science* 80, p. 1162 (2001).
50. Gordeyev, S. A., Macedo, F. J., Ferreira, J. A., van Hattum, F. W. J., Bernardo, C. A., *Physica B: Condensed Matter* 279, p. 33 (2000).
51. Du, F., Scogna, R. C., Zhou, W., Brand, S., Fischer, J. E., Winey, K. I., *Macromolecules* 37, p. 9048 (2004).
52. Wu, G., Lin, J., Zheng, Q., Zhang, M. Q., *Polymer* 47, p. 2442 (2006).
53. Rodgers, R., Mahfuz, H., Rangari, V. K., Chisholm, N., Jeelani, S., *Macromolecular Materials and Engineering* 290, p. 423 (2005).
54. Mahfuz, H., Rangari, V. K., Islam, M. S., Jeelani, S., *Composites A: Applied Science and Manufacturing* 35, p. 453 (2004).
55. Xu, Y. J., Higgins, B., Brittain, W. J., *Polymer* 46, p.799 (2005).
56. Chatterjee, A., Deopura, B. L., *Journal of Applied Polymer Science* 100, p. 3574, (2006).
57. Lozano, K., Barrera, E. V., *Journal of Applied Polymer Science* 79, p. 125 (2001).
58. Hasan, M. M., Zhou, Y. X., Jeelani, S., *Materials Letters* 61, p. 1134 (2007).
59. Zhou, Y. X., Pervin, F., Rangari, V. K., Jeelani, S., *Materials Science and Engineering A: Structural Materials Properties Microstructure and Processing* 426, p. 221 (2006).
60. Xie, H. F., Liu, B. H., Yang, H., Wang, Z. L., Shen, J. Y., Cheng, R. S., *Journal of Applied Polymer Science* 100, p. 295 (2006).
61. Dalton, A. B., Collins, S., Munoz, E., Razal, J. M., Ebron, V. H., Ferraris, J. P., Coleman, J. N., Kim, B. G., Baughman, R. H., *Nature* 423, p. 703 (2003).
62. Barber, A. H., Cohen, S. R., Wagner, H. D., *Applied Physics Letters* 82, p. 4140 (2003).
63. Salvetat, J. P., Briggs, A. D., Bonard, J. M., Bacsa, R. R., Kulik, A. J., Stockli, T., Burnham, N. A., Forro, L., *Physical Review Letters* 82, p. 944 (1999).
64. Eitan, A., Fisher, F. T., Andrews, R., Brinson, L. C., Schadler, L. S., *Composites Science and Technology* 66, p. 1162 (2006).
65. Gallant, F. M., Bruck, H. A., Prickett, S. E., *Propellants Explosives Pyrotechnics* 31, p. 456 (2006).
66. Huang, Y. Y., Ahir, S. V., Terentjev, E. M., *Physical Review B* 73, p. 125422 (2006).
67. Xiang, X. D., Sun, X., Briceno, G., Lou, Y., Wang, K. A., Chang, H., Wallace-Freedman, W. G., Chen, S. W., Schultz, P. G., *Science* 268, p.1738 (1995).
68. Amis, E. J., Xiang, X. D., Zhao, J. C., *MRS Bulletin* 27, p. 295 (2002).
69. Potyrailo, R. A., Takeuchi, I., *Measurement Science and Technology* 16, p. 1 (2005).
70. Gilman, J. W., Bourbigot, S., Shields, J. R., Nyden, M., Kashiwagi, T., Davis, R.D., Vanderhart, D.L., Demory, W., Wilkie, C. A.., Morgan, A. B., Harris, J., Lyon, R. E., *Journal of Materials Science* 38, p. 4451 (2003).
71. Nyden, M., Gilman, J. W., Davis, R., Shields, J. R., *SAMPE Journal*, p. 738, (2002).

72. Eidelman, N., Simon, C. G., *Journal of Research of the National Institute of Standards and Technology* 109, p. 219 (2004).
73. Potyrailo, R. A., Wroczynski, R. J., Pickett, J. E., Rubinsztajn, M., *Macromolecular Rapid Communications* 24, p. 124 (2003).
74. Mudalamane, R., Bigio, D.I., *AIChE Journal* 49, p. 3150 (2003).
75. Levenspiel, O., *Chemical Reaction Engineering*, Wiley Eastern Ltd., New Delhi (1962).
76. Elkouss, P., Bigio, D. I., Wetzel, M. D., Raghavan, S. R., *AIChE Journal* 52, p. 1451 (2006).
77. Andrews, R., Jacques, D., Rao, A. M., Derbyshire, F., Qian, D., Fan, X., Dickey, E. C., Chen, J., *Chemical Physics Letters* 303, p. 467 (1999).
78. Andrews, R., Jacques, D., Qian, D., Dickey, E. C., *Carbon* 39, p. 1681 (2001).
79. Bom, D., Andrews, R., Jacques, D., Anthony, J., Chen, B., Meier, M. S., Selegue, J. P., *Nano Letters* 2, p. 615 (2002).
80. Barraza, H. J., Pompeo, F., O'Rear, E. A., Resasco, D. E., *Nano Letters* 2, p. 797 (2002).
81. Mudulamane, R. (Ed.), *Calculation of Percentage Channel Fill for Co-TSEs*, University of Maryland, College Park, MD (2001).
82. Castaldi, M. J., Kwon, E., *International Journal of Green Energy* 4, p. 45 (2007).
83. Kharchenko, S. B., Douglas, J. F., Obrzut, J., Grulke, E. A., Migler, K. B., *Nature Materials* 3, p. 564 (2004).
84. Hines, P. J., Duckett, A., Read, D. J., *Macromolecules* 40, p. 2782 (2007).
85. Enikolopyan, N. S., Fridman, M. L., Stalnova, I. O., Popov, V. L., *Advances in Polymer Science* 96, p. 1 (1990).
86. McNally, T., Potschke, P., Halley, P., Murphy, M., Martin, D., Bell, S. E. J., Brennan, G. P., Bein, D., Lemoine, P., Quinn, J. P., *Polymer* 46, 8222 (2005).
87. Xheng, J., He, A., Li, J., Xu, J., Han, C. C., *Polymer* 47, 7095 (2006).
88. Bruck, H. A., Rabin, B. H., *Journal of Materials Science* 34, p. 2241 (1999).
89. Bruck, H. A., Rabin, B. H., *Journal of the American Ceramic Society* 82, p. 2927 (1999).
90. Krieger, I. M., Dougherty, T. J., *Transactions of the Society of Rheology* 3, p. 137 (1959).
91. Rodlert, M., Plummer, C. J. G., Leterrier, Y., Manson, J. A. E., *Journal of Rheology* 48, p. 1049 (2004).
92. Lin, C. R., Chen, W. J., *Colloid and Polymer Science* 277, p. 1019 (1999).
93. Einstein, A., *Annalen der Physik (Leipzig)* 19, p. 371 (1906).
94. Nielsen, L. E., *Journal of Physics D: Applied Physics* 7, p. 1549 (1974).
95. Lin, Y., Meziani, M.J., and Sun, Y. P., *Journal Materials Chemistry* 17, p. 1143 (2007).
96. Schluter, A. D. (Ed.), *Functional Molecular Nanostructures: Topics in Current Chemistry*, Springer (2005).
97. Bicerano, J., Douglas, J. F., Brune, D. A., *Journal of Macromolecular Science: Reviews in Macromolecular Chemistry and Physics C39*, p. 561 (1999).
98. Ren, J. X., Casanueva, B. F., Mitchell, C. A., Krishnamoorti, R., *Macromolecules 36*, p. 4188 (2003).

99. Solomon, M. J., Almusallam, A. S., Seefeldt, K. F., Somwangthanaroj, A., Varadan, P., *Macromolecules* 34, p. 1864 (2001).
100. Kuo, K. K., *Principles of Combustion*, 2nd Edition, John Wiley & Sons Inc., New York, NY, (2005).
101. Okamoto, Y., Miyagi, H., Kakugo, M., Takahashi, K., *Macromolecules* 24, p. 5639 (1991).
102. Wong, E. W., Shehan, P. E., Lieber, C. M., *Science* 277, p. 1971 (1997).
103. Salvetat, J. P., Kulik, A. J., Bonard, J. M., Briggs, G. A. D., Stokli, T., Metenier, K., Bonnamy, S., Beguin, F., Burnham, N. A., Forro, L., *Advanced Materials* 11, p. 161 (1999).
104. Gallant, F. M., Bruck, H. A., Kota, A.K., *Journal of Composite Materials* 38, p. 1873 (2004).
105. Gallant, F. M., Bruck, H. A., Prickett, S. E., Cesarec, M., *Composites A: Applied Science and Manufacturing* 37, p. 957 (2006).
106. Fogler, H. S., *Elements of Chemical Reaction Engineering*, Upper Saddle River, NJ, Prentice Hall (1999).
107. Meeten, G. H. (Ed.), *Optical Properties of Polymers*, Elsevier Applied Science Publishers, New York, NY (1986).
108. Jones, R. A. L., *Soft Condensed Matter*, Oxford University Press, Oxford, UK (2002).
109. Naor, P., Shinnar, R., *Industrial and Engineering Chemistry Fundamentals* 2, p. 278 (1963).
110. Pinto, G., Tadmor, Z., *Polymer Engineering and Science* 10, p. 279 (1970).
111. Wolf, D., White, D. H., *AIChE Journal* 22, p. 122 (1976).
112. Janssen, L. P. B. M., Hollander, R. W., Spoor, M. W., Smith, J. M., *AIChE Journal* 25, p. 345 (1979).
113. Thompson, M., Puaux, J. P., Hrymak, A. N., Hamielec, A. E., *International Polymer Processing* 10, p. 111 (1995).
114. Gao, J., Walsh, G.C., Bigio, D., Briber, R.M., and Wetzel, M.D., *AIChE Journal* 45, p. 2541 (1999).
115. Chen, L., Hu, G. H., Lindt, J. T., *Polymer Engineering and Science* 35, p. 598 (1995).
116. Kota, A. K., Cipriano, B. H., Powell, D., Raghavan, S. R., Bruck, H. A., *Nanotechnology* 18, p. 505705 (2007).
117. Kota, A. K., Kerzner, R., Powell, D., Bigio, D. I., Bruck, H. A., Accepted *Polymer Engineering and Science* (2007).
118. Kota, A. K., Strohmer, T., Murphy, L., Powell, D., Bigio, D. I., Bruck, H. A., Accepted *AIChE Journal* (2007).
119. Cipriano, B. H., Kota, A. K., Laskowski, C. J., Bigio, D. I., Bruck, H. A., Kashiwagi, T., Raghavan, S. R., Submitted to *Advanced Materials* (2007).
120. Kota, A. K., Cipriano, B. H., Duesterberg, M. K., Gershon, A. L., Powell, D., Raghavan, S. R., Bruck, H. A., *Macromolecules*, 40, p. 7400 (2007).